# A Novel Experimental Platform for the Study of Near-Field Radiative Transport and Measurements from Thin Dielectric Coatings

by
Yashar Ganjeh

A dissertation submitted in partial fulfillment
of the requirements for the degree of
Doctor of Philosophy
(Mechanical Engineering)
in the University of Michigan
2015

Doctoral Committee:

Associate Professor Pramod Sangi Reddy, Co-Chair
Professor Edgar Meyhofer, Co-Chair
Associate Professor Anthony Grbic
Assistant Professor Xiaogan Liang

# Table of Contents

# List of Figures

# List of Tables

# Abstract

Near-field radiative heat transfer (NFRHT) is an active area of research with implications for heat transfer and thermal management technologies in the future. Previous experiments observed that when the gap-size between a hot surface, the emitter, and a cold one, the receiver, reduces to micrometer dimensions significant enhancements in radiative heat flow between the two surfaces, above the value predicted by Stefan-Boltzman law, are observed. Subsequent theoretical studies supported these results and predicted orders-of-magnitude enhancement in radiative heat flow if the gap-size is further decreased to nanoscale. A range of other interesting phenomena are also predicted for this near-field regime. One of the most intriguing of these theoretical predictions is that pertaining to NFRHT enhancements calculated for nanoscale-thin dielectric coatings. In particular, when the gap-size between the emitter and receiver becomes comparable to film thickness, the enhancements in radiative heat flow are predicted to be as large as those for bulk materials, which can result in heat transfer coefficients that are ~20 times that of far-field values for a gap size of ~20 nm. No experiment has proved the validity of theoretical predictions pertaining to NFRHT enhancement from nanoscale-thin dielectric films.

Here, a new experimental platform to perform NFRHT experiments is presented. The platform consists of two major components; a microfabricated resistive picowatt-resolution calorimeter and a six degree-of-freedom nanopositioner that can parallelize two planes with ~6 μrad of resolution. While this platform is designed to eventually perform NFRHT measurements between parallel

plates, here it is used to measure enhancements of radiative heat flow between a spherical emitter and thin dielectric receiver with varying thickness. Consequently, for the first time, a dramatic increase in near-field radiative heat transfer from thin dielectric films is observed, which is comparable to that obtained between bulk materials, even for very thin dielectric films (50–100 nm) when the spatial separation between the hot and cold surfaces is comparable to the film thickness. These results are attributed to the spectral characteristics and mode shapes of surface phonon polaritons, which dominate near-field radiative heat transport in polar dielectric thin films.

# CHAPTER 1

# Near-Field Radiative Heat Transfer (NFRHT): An Introduction

## 1.1 Introduction

Near-field radiative heat transfer (NFRHT) is an active area of research with technological implications for future thermo-photovoltaic (TPV) [1], thermal management [2], and energy conversion devices [3, 4]. There is a wealth of theoretical work which predicts significant enhancement in radiative heat transfer in the near-field regime that cannot be explained by the Stefan-Boltzmann law for far-field radiation [5]. The near-field regime is realized when the distances separating a hot emitter and a cold receiver are reduced to below the thermal wavelengths given by Wien's displacement law. In this chapter, a theoretical framework to explain this behavior and a brief summary of experimental observations of NFRHT are presented.

## 1.2 Near-Field Radiative Heat Transfer (NFRHT)

Radiative heat transfer in the far-field regime (Fig 1.1) where the gap $d$ between a hot surface, called an emitter, and a cold one, called a receiver, is larger than their thermal wavelength given by Wien's displacement law, is well understood and the maximum heat transfer between the two bodies can be calculated via Stefan-Boltzman law [6]; according to this law, the maximum heat flux ($q$) between a hot surface called the emitter, and cold one called the receiver can be calculated as $q = \sigma\,(T_{emit}^4 - T_{rec}^4)$, where $T_{emit}$ *and* $T_{rec}$ are the temperatures of the emitter and the receiver respectively and σ is the Stefan-Boltzman constant.

However, when the gap distance between the two surfaces becomes comparable to or less than their thermal wavelength (Fig 1.1d), significant enhancement in radiative heat transfer is possible due to the contribution of "evanescent waves", which exist at the interface between two media. These waves decay exponentially away from the interface and consequently do not contribute to heat transfer when the two surfaces are far away from each other. However, when the gap-sizes become small, these waves greatly enhance the energy density. Thus, NFRHT, unlike Far-Field Radiative Heat Transfer (FFRHT), is highly gap-size dependent. There are different sources for these evanescent waves; they can occur at an interface due to total internal reflection. In other cases surface waves such as surface phonon polaritons for polar dielectrics, can result in evanescent waves [7, 8]. Here I give a brief overview of theoretical framework that is used to calculate enhancements in heat transfer due to near-field radiation. A more detailed theoretical explanation is given in chapter 3 to explain the origins of these enhancements in the special case of polar dielectric thin films.

Radiative heat flux for a body at thermal equilibrium is a result of random fluctuations of charges (e.g. electrons in metals) which result in thermally-driven electrical currents. Polder and van Hove [5] presented some of the first calculations for NFRHT using Rytov's fluctuational electrodynamics [9] to relate these thermally-driven stochastic electrical currents in objects to the resulting electromagnetic fields. Using the fluctuation-dissipation theorem, these currents are given by [10]:

$$\langle j_m(\overrightarrow{r'},\omega) j_n^*(\overrightarrow{r''},\omega)\rangle = \frac{4}{\pi}\omega\varepsilon_0 Im[\varepsilon(\omega)]\delta_{mn}\delta\left(\overrightarrow{r'}-\overrightarrow{r''}\right)\Theta(\omega,T)\delta(\omega-\omega'), (1)$$

Where $j_{m,n=1,2,3}$ denote the *x*, *y* ,*z* components of the current density, $\delta_{mn}$ and $\delta(\omega - \omega')$ are the Kroneceker and Dirac delta and $\Theta(\omega, T)$ is the mean energy of a Planck oscillator. * denotes the complex conjugate. Introducing these random currents as source terms in Maxwell's equations one can solve for the proper Dyadic Green's Functions for the geometry of interest and obtain the electric and magnetic fields:

$$\vec{E}(\vec{r},\omega) = i\omega\mu_0 \int_V \overleftrightarrow{G}\left(\vec{r},\overrightarrow{r'},\omega\right).\vec{j}\left(\overrightarrow{r'},\omega\right)d\overrightarrow{r'}, (2)$$

$$\vec{H}(\vec{r},\omega) = \int_V \nabla\times\overleftrightarrow{G}\left(\vec{r},\overrightarrow{r'},\omega\right).\vec{j}\left(\overrightarrow{r'},\omega\right)d\overrightarrow{r'}\ , (3)$$

Here, $\mu_0$ is the magnetic permeability of vacuum and $\overleftrightarrow{G}\left(\vec{r},\overrightarrow{r'},\omega\right)$ is the Green's function that relates the current source $\vec{j}$ at $\overrightarrow{r'}$ to the resulting electric field at $\vec{r}$.

Subsequently these fields can be used to calculate the spectral energy flux by the means of spectral Poyting vector:

$$\langle\vec{S}(\vec{r},\omega)\rangle = \int_0^\infty \frac{1}{2}\langle Re[\vec{E}(\vec{r},\omega)\times\overrightarrow{H^*}(\vec{r},\omega')]\rangle d\omega' \quad (4)$$

Following the procedure discussed above, it can be shown that heat flux (heat transfer per unit time and per unit area) can be calculated as follows:

$$Q(T_1, T_3, d) = \int_0^\infty \frac{d\omega}{4\pi^2} [\Theta(\omega, T_1) - \Theta(\omega, T_3)] \int_0^\infty dkk [\tau_s(\omega, k) + \tau_p(\omega, k)] \quad (5)$$

where $\Theta(\omega, T_i) \equiv \hbar\omega / [\exp(\hbar\omega / k_B T_i) - 1]$ , where 1 and 3 denote the emitting and the receiving surfaces, respectively, and 2 corresponds to the vacuum gap. $\omega$ is the radiation frequency, $k$ is the magnitude of the wave vector component parallel to the layer planes and $\tau_s$ and $\tau_p$ are the transmission probabilities for the transverse electric (TE) and transverse magnetic (TM) modes, respectively. These probabilities can be calculated in terms of Fresnel reflection coefficient as [11]:

$$\tau_{\alpha=s,p}^{13}(\omega, k) = \begin{cases} \frac{(1-|r_\alpha^{12}|^2)(1-|r_\alpha^{23}|^2)}{|D_\alpha|^2}, & if\ k < \frac{\omega}{c}, propogating\ waves \\ \frac{4Im(r_\alpha^{12})Im(r_\alpha^{23})e^{-2Im(\zeta_3)d}}{|D_\alpha|^2}, & if\ k > \frac{\omega}{c}, evanescent\ waves \end{cases}, \quad (6)$$

The Fresnel reflection coefficients are given by:

$$r_s^{ij} = \frac{\zeta_i - \zeta_j}{\zeta_i + \zeta_j}, \quad (7)$$

$$r_p^{ij} = \frac{\varepsilon_j \zeta_i - \varepsilon_i \zeta_j}{\varepsilon_j \zeta_i + \varepsilon_i \zeta_j}, \quad (8)$$

Where $\zeta_i = \sqrt{\varepsilon_i(\omega)\, \omega^2/c^2 - k^2}$ is the transverse component (perpendicular to planes) of the wavevector and $\varepsilon_i(\omega)$ is the frequency-dependent complex dielectric function and $D_\alpha = 1 - r_\alpha^{12} r_\alpha^{23} e^{i\zeta_3 d}$ is the Fabre-Perot-like denominator. I get back to these relations in chapter 3, where the reason behind the observed enhancements due to NFRHT are considered in more depth.

This framework is used for nearly half a century to calculate NFRHT between different types of materials, e.g. metals, dielectrics [12], and doped semiconductors [13, 14]. Some of these

calculations were repeated for the plate-plate geometry by my colleague, Bai Song, and the results for different material combinations are shown in Fig 1e. As can be seen in this figure, for two dielectric surfaces ($SiO_2$-$SiO_2$, or SiC-SiC) the heat transfer coefficient at a gap-size of 10 μm can be 3 orders-of-magnitude larger than the far-field values. Consequently, NFRHT holds great promise for future energy conversion devices.

While there are multiple theoretical studies that explored NFRHT, experimental work is very sparse. The first experimental observation of NFRHT dates back to 1969 when Domoto and coworkers observed heat transfer increases between copper disks at liquid Helium temperatures [15]. Later, Hargreaves conducted measurements between chromium plates but at room temperature and observed enhancements in heat flow [16]. More recently, measurements of NFRHT were made between closely-spaced silica plates [17], sapphire plates [18], and between metallic surfaces at cryogenic temperatures [19, 20]. All these measurements observed enhancements beyond those expected from law of black-body radiation. A recent study has also achieved measurement of NFRHT between $SiO_2$ beams with gap-sizes as small as ~250 nm [21].

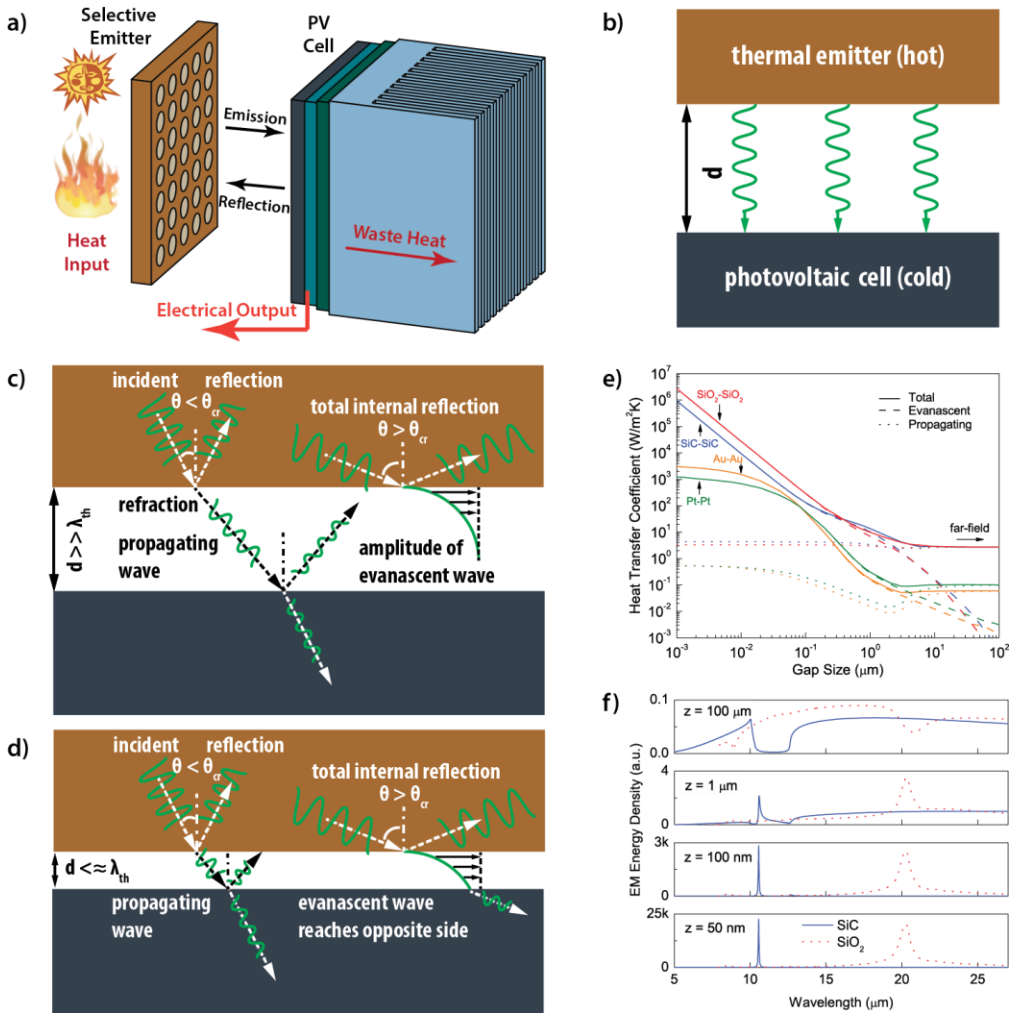


***Figure 1.1**. **Near-Field Radiative Heat Transfer and its Possible Application.** **a** depicts a TPV device that is comprised of a hot thermal emitter and a photovoltaic cell with an appropriate band gap. **b** shows a schematic of the device. Figures **c** and **d,** depict how propagating and evanescent modes contribute to thermal transport; when the emitter and receiver are separated with gap-sizes that are higher than thermal wavelength, the evanescent waves decay before reaching the receiver and hence do not contribute to energy transfer. In **d**, where the separation is smaller than thermal wavelength, these waves can reach the receiver and hence contribute to energy transfer. **e,** shows computational predictions for heat transfer coefficients (HTC) between parallel plates for different materials [10]. The calculations are based on fluctuational electrodynamics and more details are given in Chapter 3. **f,** computed electromagnetic energy density at various heights above a semi-infinite SiC and $SiO_2$ surface [10].*

However, considering cross section of the beams (500 nm × 1.1 μm) used in comparison to the propagation length of surface electromagnetic waves responsible for NFRHT in $SiO_2$ which is ~10 μm [22], this experiment is not a true representation of plane-plane geometry as the plane is

confined in one dimension. In another recent work, nanostructured pillars on $SiO_2$ microplates were leveraged to achieve gap-sizes below 1 μm between the plates; however, the measurements were limited to three gap-sizes and suffered from large uncertainties both in gap-size and the heat transfer coefficient [23].

None of the aforementioned experimental measurements of NFRHT between parallel plates have achieved submicrometer-sized gaps between parallel plates. This is because of the numerous experimental and technical considerations that are required to make such a measurement; more specifically, these limitations can be summarized as follows:

1) Large heat fluxes can only be obtained if the emitter and the receiver are sufficiently large; however, it's almost impossible to make large plates with gap-sizes below a micrometer. This is mainly because they will not be flat. One remedy is to use planes with micrometer dimensions. However, heat fluxes associated with microfabricated plates will be small and in order of picowatts and will require high-sensitivity calorimetry techniques.
2) Even with microfabricated plates, the two surfaces will need to be extremely smooth and clean. The roughness of the surface and existence of contaminating particles on them will limit the minimum achievable gap-size.
3) Finally, even if the two surfaces are perfectly flat, smooth and clean, and we are able to measure heat flows as small as picowatts, an instrument is needed to position them parallel to each other and control their spatial separation with nanometer resolution.

Going back to Fig 1.1e, it can be seen that only when the gap distance is reduced to below a micrometer, can one observe significant enhancement in the HTC. As a result of the above experimental difficulties, the most interesting portion of the near-field regime with the most

significant increase in heat flow remains experimentally unexplored. To achieve sub-micrometer gap-sizes and circumvent the experimental difficulties associated with the alignment of two planes, some experiments were done using other configurations. The main idea behind these set-ups was the removal of the need for plane-plane parallelization.

As one alternative, the sphere-plane geometry has been used as a means to circumvent the experimental difficulties that occur when aligning two plates. Two of such setups, which measured NFRHT between a sphere and a plate were developed by Shen *et al.* [24, 25], and Rousseau *et al.* [26]. Since heat fluxes in sphere-plane configuration are much smaller than plane-plane configurations, these two setups rely on high-resolution bimaterial cantilever temperature sensors [27, 28] to resolve small temperature changes of ~10-100 μK, which are measured by attaching a silica sphere to the end of a vertical bimaterial cantilever and detecting the deflections of the beam using an optical laser. Based on the results of these experiments, when the spatial separation between the sphere and the plate approaches nanometers (~30 nm), the heat transfer coefficient exceeds that set by the blackbody radiation limit by three orders of magnitude.

## 1.3 NFRHT enhancement from thin films

All of the experimental efforts described in section 1.2 studied NFRHT between bulk substrates. However, one of the most interesting theoretical predictions pertaining to NFRHT is the enhancement expected from polar dielectric thin films. For example, Francoeur's calculations predicted ~3 orders of magnitude enhancement in radiative heat flux from 10 nm-thick SiC coatings, which was 2.2 times larger than that of bulk SiC [29]. In another study, Basu calculated similar enhancements for $SiO_2$ coatings and attributed these enhancements to gap-size dependence of penetration depth for NFRHT [30]. At both cases, the enhancements occur when the gap-size

between the two surfaces become comparable to film thickness. The framework used for these calculations is similar to the one explained in section 1.2. When dealing with thin coatings or multilayer system, the relations given by (6) can be replaced by the following [31, 32]:

$$\tau_{\alpha=s,p}^{13}(\omega,k)=\begin{cases}\frac{(1-|R_\alpha^1|^2)(1-|R_\alpha^3|^2)}{|D_\alpha|^2}, & if\ k<\frac{\omega}{c}, propogating\ waves\\ \frac{4Im(R_\alpha^1)Im(R_\alpha^3)e^{-2Im(\zeta_3)d}}{|D_\alpha|^2}, & if\ k>\frac{\omega}{c}, evanescent\ waves\end{cases}, (9)$$

Where the Fresnel reflection coefficients, $r_\alpha^{ij}$, have been replaced by total reflection coefficients of the system $R_\alpha^i$. This equation is considered in more detail in chapter 3. None of these theoretical predictions pertaining to NFRHT enhancement from thin films have been tested experimentally.

## 1.4 Dissertation Goals

While there is a lot of theoretical work that have explored NFRHT enhancement for the past half-century, experimental work, especially a direct measurement between parallel planes with sub-micrometer gaps have been limited; in other words, the current experimental platforms are not adequate for a systematic measurement of NFRHT between parallel plates. In the first part of my thesis, chapter 2, I am going to present a novel experimental platform for study of near-field radiative heat transfer. This platform consists of two main components:

1. A microfabricated picowatt-resolution calorimeter to measure small changes in radiative heat flow with changing gap-size
2. A 6 degree-of-freedom nanopositioner, which enables precise positioning of two microdevices with respect to each other and can control the gap-size between them with nanometer resolution

I show the details of these platforms and close the chapter by presenting our initial measurements between $SiO_2$ plates.

In the 2nd part of my thesis, chapter 3, I am going to use the same platform to address a central question regarding NFRHT enhancement from thin dielectric coatings. As mentioned above, a lot of theoretical work predicts enhancements from thin dielectric films that can be comparable to those from bulk materials. In chapter 3, using our platform, I demonstrate the validity of these prediction experimentally. I support these results by presenting an in-depth theoretical explanation of these results.

Finally in chapter 4, a summary of the work and possible future directions are given.

# CHAPTER 2

# An Experimental Platform for NFRHT Measurements

## 2.1 Introduction

In this section, an experimental platform for performing NFRHT measurements is presented in detail. The platform consists of two parts: a) a picowatt-resolution calorimeter that is needed to measure the small changes in heat-flow associated with NFRHT with changing gap-size, and b) a custom-built 6 degree-of-freedom nanopositioner that enables manipulation of the desired microfabricated devices with respect to each other. Taken together, these two instruments will enable measurement of radiative heat transfer coefficient (HTC) with varying gap-sizes. In particular, in chapter 3, this platform is used to address the central question of my thesis in measuring enhancements in radiative heat flow from thin dielectric coatings.

## 2.2 Room-Temperature Picowatt-Resolution Calorimetry

In order to enable measurements of small heat flow changes associated with NFRHT with changing gap-size, one needs very high resolution calorimeters. During the first year of my PhD, I worked on the development of a picowatt resolution calorimeter [33] that were later modified for NFRHT experiments. Here, I briefly discuss the concept behind the design of the calorimeter and how it differs from the devices that were eventually used in the NFRHT experiments.

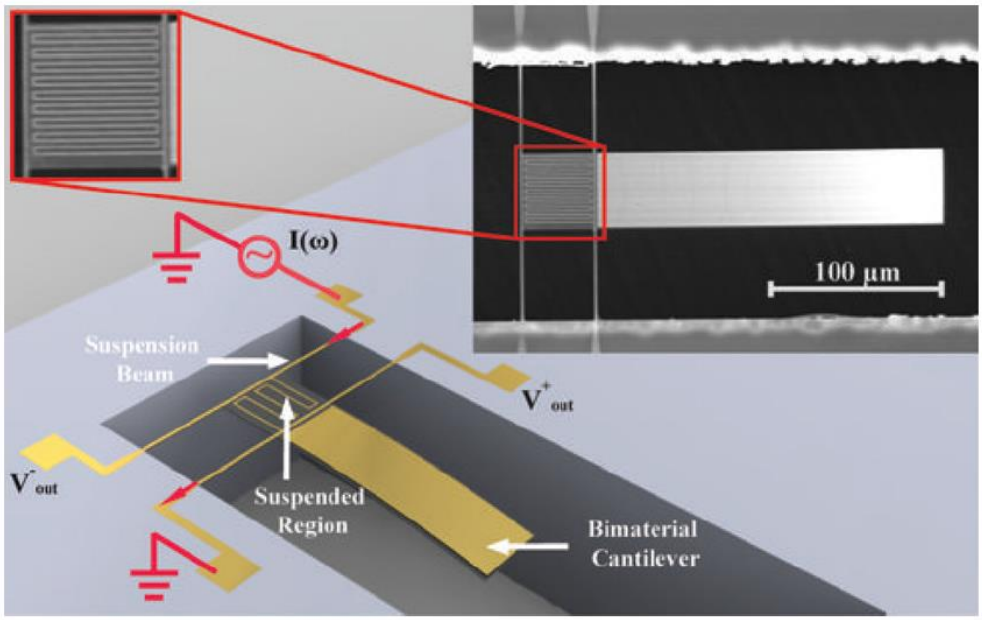


***Figure 2.1. Schematic of a picowatt calorimeter is shown along with a scanning electron micrograph of a microfabricated device (inset).*** *The central area of the device is suspended by thin (~2 µm) and long (~50 µm) beams. A serpentine line that serves as a 4-probe heater/thermometer and a 200 µm long bimaterial cantilever that acts as an ultra-sensitive thermometer are integrated into the suspended region; figure adapted from [33].*

The basic strategy employed in this work for achieving picowatt-resolution calorimetry is to microfabricate a thermally isolated island from which very precise temperature measurements can be made. This is shown in Fig. 2.1; here, the calorimeter consists of a thin low-stress silicon nitride

($SiN_x$) membrane that is suspended by thin and long $SiN_x$ beams which have a combined thermal conductance ($G$) of ~600 nW/K and serve to thermally isolate the suspended membrane. Further, a bimaterial cantilever that can detect periodic temperature variations with a resolution ($\Delta T_{res}$) of ~4 μK and a noise floor of ~6.4 μK is integrated into the suspended membrane. When this suspended device is operated in a high vacuum environment ($<10^{-6}$ Torr), thermal conduction via the gas molecules and heat transport by radiation are negligible, ensuring that the total thermal conductance between the suspended region and the environment is ~600 nW/K. In other words, the only thermal resistance between the suspended region and the substrate is due to conduction through the four suspending beams. The low thermal conductance of the beams and the excellent temperature resolution of the bimaterial cantilever enable single-digit picowatt resolution (since $q = G \times \Delta T_{res}$). A schematic of the picowatt calorimeter along with a scanning electron micrograph of a fabricated device is shown in Figure 2.1.

While this set-up successfully achieves picowatt-resolution at room temperature, it relies on the bimaterial cantilever temperature sensor to achieve a high temperature resolution. The mechanical coupling from deflections of the bimaterial cantilever make this design unsuitable for NFRHT measurements. More precisely, the deflections of bimaterial cantilever resulting from temperature changes will couple to the suspended membrane and consequently prevent accurate measurement of gap-size between the calorimeter and an emitting surface. Consequently, for NFRHT measurements that require accurate measurement of gap-sizes, a calorimeter which does not rely on temperature measurements using a moving cantilever is needed. Based on a careful analysis of noise performance of resistive heater/thermometers, Sadat [34, 35] was able to design calorimeters that only used resistive thermometers to achieve picowatt resolution. These calorimeters did not

need bimaterial cantilevers. These modified devices did not suffer from mechanical coupling between the cantilever and the suspended surface and were used in our NFRHT measurements. They are presented in chapter 3.

## 2.3 A Platform to Parallelize Planar Surfaces and Control their Spatial Separation with Nanometer Resolution

As I mentioned in chapter 1, there is not sufficient experimental work for NFRHT between parallel plates with submicrometer gaps. Here, I present a nanopositioning platform that can manipulate two planar surfaces and control their spatial separation with nanometer resolution[36]. While the final purpose of this platform is measurement of NFRHT between parallel plates, here I use it to study NFRHT enhancement from thin dielectric coatings in a sphere-plane geometry. This instrument was designed and built by me, in collaboration with my colleague Bai Song and makes use of an integrated reflected light microscope, and is capable of parallelizing two planar surfaces such that the angular deviation of the surfaces is <6 μrad, while simultaneously allowing control of the gap from 15 μm down to contact with ~0.15 nm resolution. The capabilities of this platform were verified by using two custom-fabricated micro-devices with planar surfaces, 60 × 60 $\mu m^2$ each, whose flatness and surface roughness were experimentally quantified. The microdevices were fabricated by other lab members. We first parallelized the two micro-devices by using the developed platform in conjunction with a simple optical approach that relies on the shallow depth of field (~2 μm) of a long working distance microscope objective. Subsequently, we experimentally tested the parallelism achieved via the optical alignment procedure by taking

advantage of the electrodes integrated into the micro-devices (Fig. 2.6). Our measurements unambiguously show that the simple depth-of-field based optical approach enables parallelization such that the angular deviation between the two surfaces is within ~500 μrad. This ensures that the separation between any two corresponding points on the parallel surfaces deviate by ~30 nm or less from the expected value. Further, we show that improved parallelization can be achieved using the integrated micro-electrodes which enable surface roughness limited parallelization with deviations of ~5 nm from parallelism.

## 2.4 Design of the Nanopositioner

As mentioned in chapter 1, computational studies of NFRHT between parallel surfaces with nanoscale separation (~100 – 1000 nm) have predicted several interesting effects such as a dramatic increase—by orders of magnitude—in the thermal conductance between planar surfaces [7, 8, 37] (in comparison to surfaces separated by macroscale gaps), and rectification of radiative heat currents [38]. Recent work has succeeded in experimentally probing NFRHT between parallel surfaces separated by micrometer sized gaps [18, 19, 39] as well as between a sphere and a plane separated by nanoscale gaps [24, 26]. The sphere-plane geometry, while experimentally convenient, is not easily amenable to direct theoretical/computational analysis [40]. Further, most novel materials of interest [32, 41, 42] in NFRHT cannot be readily fabricated in the form of spheres—highlighting the need for an experimental platform to probe NFRHT between parallel surfaces separated by nanoscale gaps. However, such measurement capabilities are nonexistent due to the experimental challenges in parallelizing planar surfaces as well as in creating and controlling nanoscale separations in-between them.

In order to parallelize two finite-area planar surfaces of equal size it is necessary to have excellent control on the relative tilt angles ($\theta_x$, $\theta_y$) between the two planes (see Fig. 2.2 for the definition of the coordinate system). Further, to ensure that the corresponding points of the top and bottom planes (Fig. 2.2) can be aligned precisely with respect to each other it is necessary to control both their relative alignment along the *x*, *y* directions and the angular orientation about the *z* axis ($\theta_z$) (Fig. 2.2). Finally, in order to control the spatial separation between them it is necessary to have fine control on relative positioning of the two planes along the *z* axis.

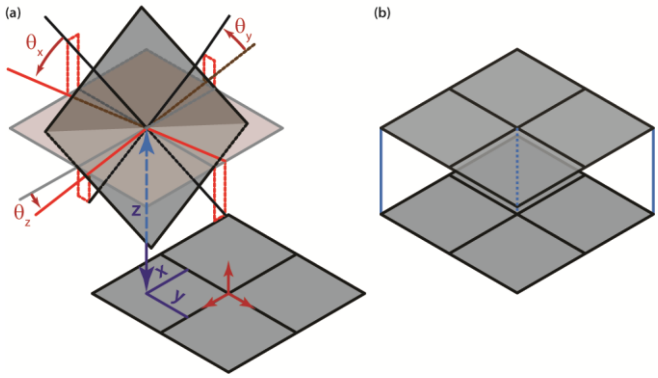


***Figure 2.2. Schematic of two finite-area planar surfaces to be made parallel to each other.*** *Control of the relative alignment along the x, y, z directions, and the relative angular alignment* $\theta_x$, $\theta_y$, $\theta_z$, *is required to accomplish the desired parallelization. The Cartesian coordinate system is attached to the laboratory reference frame; figure adapted from [36].*

In this section, we describe the design of a custom-built nanopositioning instrument that enables control of all the relevant relative degrees-of-freedom ($x$, $y$, $z$, $\theta_x$, $\theta_y$, $\theta_z$) to accomplish the desired parallelization. The basic design of the nanopositioner (Fig. 2.3) comprises of two major

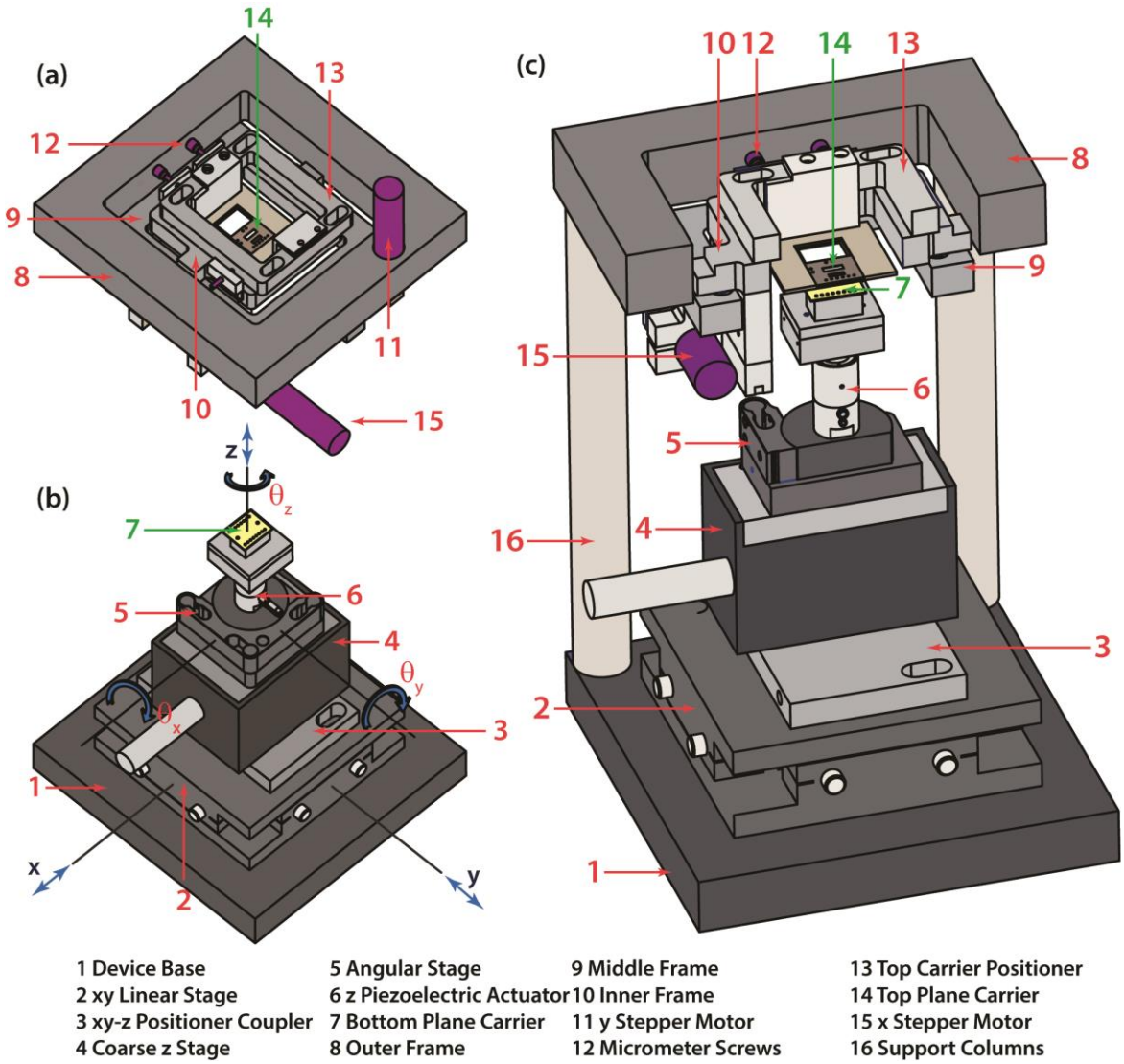


***Figure 2.3. Schematic design of the nanopositioner with the major parts labeled. a,*** *the top subassembly is used to control the relative angular alignments* $\theta_x$, $\theta_y$ *as well as to enable control of the relative alignment of the two planes along the x, y directions,* ***b,*** *the bottom subassembly controls the relative alignment of the bottom plane along the x, y directions as well as the angular rotations about x, y, and z directions. The spatial separation is controlled using a z-linear stage and a piezoelectric actuator to control the position in z direction.* ***c,*** *Sectional view of the top and bottom subassemblies assembled together by four columns (two of the columns are not shown for visual clarity) ; figure adapted from [36].*

subassemblies: the top and bottom subassemblies. The top subassembly (Fig. 2.3a) houses the top plane and enables fine control of $\theta_x$, $\theta_y$ as well as coarse positioning along the *x* and *y* directions.

The bottom subassembly (Fig. 2.3b) houses the bottom plane and enables coarse alignment along the *x*, *y* directions and the $\theta_x$, $\theta_y$ angles. Further, it also enables rotation along the $\theta_z$ direction along with both coarse and fine approaches in the *z* direction. Figure 2.3c shows a cross-sectional view of the assembled nanopositioner where the top and bottom subassemblies are connected by four columns (two of the columns are not shown for visual clarity).

### 2.4.1. Description of the Top Subassembly

In order to control the relative angular positions $\theta_x$ and $\theta_y$, a custom-built goniometer was integrated into the top subassembly. The goniometer consists of three rigid frames: the outer frame, the middle frame and the inner frame (parts 8 - 10 of Fig. 2.3, respectively). All parts are made of Aluminum 6061, unless otherwise noted. The outer frame serves to attach the top subassembly to the bottom subassembly via four rigid columns (part 16 of Fig. 2.3c) and houses two fixed sockets of the spherical joints for $\theta_y$-rotation (see below). The middle frame enables control of the relative rotation $\theta_y$ as it is designed to rotate about the *y* axis (see Figs. 2.4a and b) via two spherical joints that use precision ground stainless steel spheres. Figures 2.4a and b show the outer and middle frames and one such joint. The rotation of the middle frame is accomplished by using a stepper motor (part 15,Fig. 2.5a, PI M-224.27), which exerts a torque about the *y* axis. The motor has a stainless steel sphere on its head and pushes on a stainless steel attachment that is rigidly connected to the frame; these parts were made from steel to reduce surface abrasions. Further, an opposing torque is provided by a preloaded spring that pulls the middle frame against the outer frame. Thus, the motor along with the spring controls the angular position. The inner frame of the top subassembly is connected to the middle frame, via an identical design, to enable rotations about the *x* axis. Ideally, the inner and middle frames should be mounted such that the *x* and *y* axes of

rotations intersect each other. However, due to inevitable tolerances in machining we estimate that the two axes are separated from each other by ~10 μm.

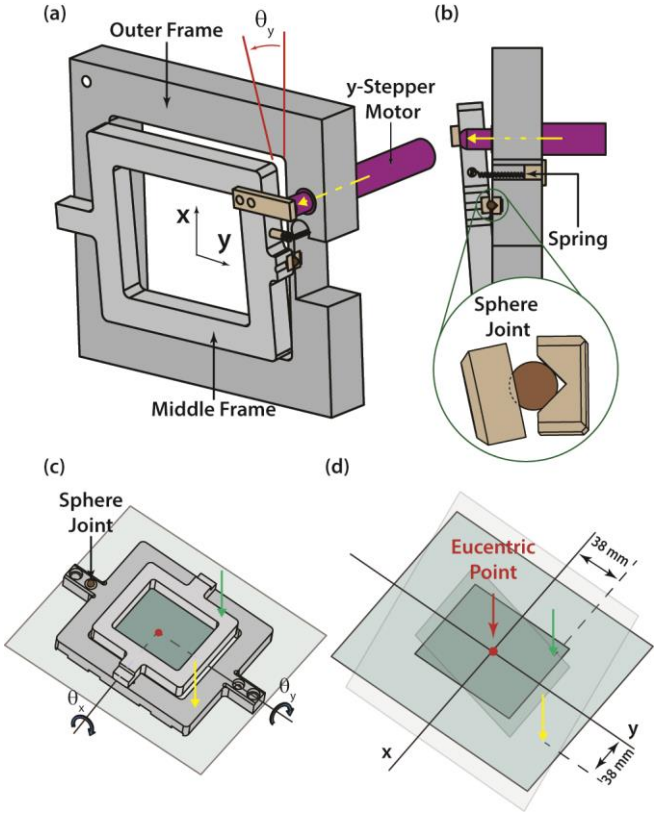


***Figure 2.4. Angular control of the top plane with the custom-built goniometer. a,*** *isometric view showing how rotation about y axis is controlled;* ***b,*** *side view showing the preloaded spring and one of the sphere joints;* ***c,*** *schematic view of the middle and inner frames and the extended top plane (shaded blue), with arrows showing equivalently where the motors push for the x (green) and y (yellow) axes;* ***d,*** *schematic drawing demonstrating how the location of eucentric point remains unchanged during rotation of the two frames and hence the importance of placing the top plane as close to it as possible. The arm lengths where each stepper applies its equivalent force are also shown; figure adapted from [36].*

Our analysis and experimental observations show that this small deviation from ideality does not pose significant limitations for our nanopositioning scheme; hence, we neglect it and assume that the axes intersect. The point of intersection of the axes is called the eucentric point, which represents the center of rotation (Figs. 2.4c and d).

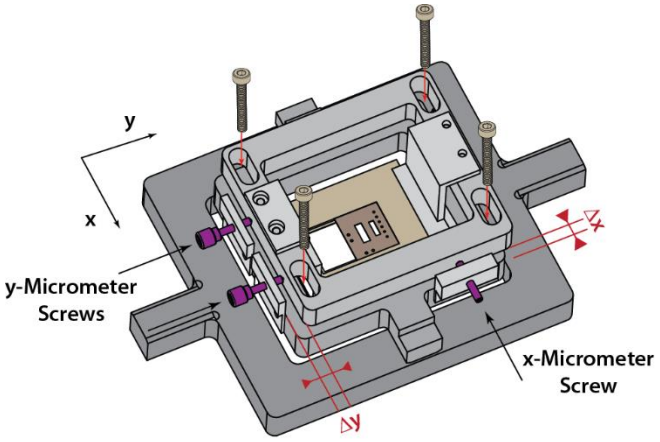


***Figure 2.5. Control of the position of the top carrier in x and y directions****. Three micrometer screws are used for this purpose: one for x direction and the other two for y direction adjustments. Upon reaching the final desired position of the top carrier, the location of the positioner is fixed by holding it rigidly against the inner frame using four screws as shown; figure adapted from [36].*

In order to accomplish parallelization to within our experimental requirements, it is necessary to ensure that the centroid of the top plane is located in close proximity (~10 μm) to the eucentric point. If this condition is not met, rotations about the *x* and *y* axes lead to appreciable translational motion of the centroid, which is detrimental to the parallelization process. In order to position the centroid at the eucentric point, we have integrated into the inner frame an additional translational positioner (part 13 of Fig. 2.3a) that has the top plane rigidly attached to it. The *x* and *y* locations of this positioner (with respect to the inner frame) are adjusted by three micrometer screws (M3×0.25) as shown in Fig. 2.5. After positioning the centroid of the top plane to the eucentric

point the translational frame is tightly fixed to the inner frame with four M3 screws to prevent mechanical drift. The separation between the centroid and the eucentric point along the *z* axis is carefully adjusted with shim stock to reduce deviation to ~10 μm.

### 2.4.2. Description of the Bottom Subassembly

In order to control the relative position of the two planes along the *x*, *y*, and *z* directions as well as to control the angular rotation about the *z* axis ($\theta_z$) we integrated a commercial *xy* linear stage (part 2 of Fig. 2.3, Newport M401), a *z* stage (part 4 of Fig. 2.3, Klinger Scientific MVD-50), a piezoelectric linear actuator along *z* direction (part 6 of Fig. 2.3, Physik Instrumente 845.10(V)), and a custom-designed *z* axis rotation element (part 3 of Fig. 2.3). Additionally, a coarse tip-tilt mechanism for controlling the angular rotation of the bottom plane was also added (part 5 of Fig. 2.3, Newport U200-P) to further facilitate overall control of $\theta_x$ and $\theta_y$.

The commercial *xy*-stage has an adjustment resolution of ~1 μm and a range of 12 mm in both *x* and *y* directions and supports all the components of the bottom subassembly. The *xy* linear stage is coupled to a coarse *z*-stage through the rotation element. Minor adjustment in the relative rotation of the two planes about the *z* axis is possible by rotating this element with a micrometer screw (Thorlabs DAS110, not shown in Fig. 2.3). The *z* stage has an adjustment resolution and range of 5 μm and 12 mm, respectively. This stage can be used to coarsely control the spatial separation between the top and bottom planes. For high resolution adjustments of the gap size, which is an important requirement for future NFRHT experiments, a piezoelectric actuator with a range of ~15 μm and a resolution of ~0.15 nm (limit set by our electronics) is used.

In addition to controlling translation in the *x*, *y*, and *z* directions, it is also convenient to control the angular rotation of the bottom plane using a kinematic mount (part 5 of Fig. 2.3), which is sandwiched between the *z* stage and the piezoelectric actuator. Although this alignment is in-principle not necessary for parallelization, it facilitates the particular optical approach that we implemented in this work to enable parallelization of surfaces (described in detail in section 2.5). Finally, a carrier (part 7 of Fig. 2.3) that houses the bottom plane is mounted on the actuator.

### 2.4.3. Estimation of the Achievable Parallelism

We estimate the relative angular positioning that is achievable using the nanopositioner described above. The stepper motors have a step size of 200 nm. The effective arm length of the inner frame for rotation about the *x* axis is ~38 mm (Fig. 2.4d) suggesting that the angular resolution $\theta_{x,\,res}$ is ~6 µrad (200 nm/38 mm). A similar resolution is expected for rotations about the *y* axis as the arm length is the same.

| Area of Parallel Surfaces | 60 × 60 µm$^2$ | 200 × 200 µm$^2$ | 1000 × 1000 µm$^2$ |
|---|---|---|---|
| Estimate of achievable spatial deviation from parallelism (*p*) | 0.36 nm | 1.2 nm | 6 nm |

***Table 2.1.*** *Estimates of the achievable spatial deviation from parallelism for ideal planar surfaces of different areas, using the custom-built nanopositioner; table adapted from [36].*

To determine the degree of parallelism achievable by the platform described above, we first define as a metric for the parallelism of any two finite-area planar surfaces the spatial deviation from

parallelism *p*, which is given by $p = |\Delta z_{\max} - \Delta z_{\min}|$. Here, $\Delta z_{\max}$ ($\Delta z_{\min}$) represents the maximum (minimum) separation along the *z* direction between any two points of the planes. Given the estimated angular resolution, *p* is estimated to have values ranging from 0.4 nm to 5 nm for ideal surfaces of various areas as shown in Table 1. In practice, a lower limit of ~5 nm is more reasonable since the inherent roughness of the real surfaces does not allow the realization of the ideal value.

## 2.5 Requirements for Achieving Excellent Parallelization and Description of Micro-devices Used in Experiments

In order to leverage the nanopositioner and reduce the separation between two parallel planar surfaces down to the nanometer scale, both surfaces must be extremely flat, smooth, and free of particulate contamination. In other words, if either surface has an appreciable curvature, a roughness of tens of nanometers, or if there are particles of considerable size (e.g. >10 nm) on the surface, nanoscale separation with a *p* value smaller than the characteristic dimensions of these imperfections cannot be achieved. Creation of macroscopic surfaces that satisfy these conditions is extremely challenging due to difficulties associated with both creating such surfaces and keeping them free of particulate contamination. Further, characterization of macroscopic surfaces to ensure that they indeed meet the desired conditions is also very difficult.

In order to overcome these problems, we chose to fabricate two micro-devices each of which enclose planar regions which are ~60 × 60 $\mu m^2$ in size (see Fig. 2.6). The first device (see schematic in Fig. 2.6a), represents the top plane and is called the top device. It has four integrated metallic electrodes, which play an important role in our experiments (explained in detail below). The second device (Fig. 2.6b), represents the bottom plane and is a mesa-shaped structure with a planar

area of ~60 × 60 μm$^2$, on its top. Further, this entire mesa-shaped structure is coated with a metal to enable the experiments (explained in detail below). These micro-devices are desirable because it is possible to directly quantify their surface characteristics using atomic force microscopy (AFM), dark field optical microscopy (DFOM), and scanning electron microscopy (SEM). We now describe our approach to practically realizing the desired devices using standard microfabrication techniques as well as our approach to characterize their surfaces.

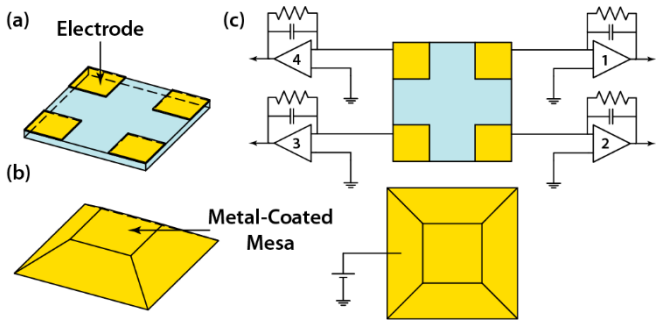


***Figure 2.6. Schematic of the micro-devices. a,*** *top device representing the top planar surface;* ***b,*** *bottom mesa device representing the bottom planar surface (shown upside-down);* ***c,*** *schematic drawing showing the current amplifiers connected to the top electrodes and a voltage bias applied to the bottom electrode; figure adapted from [36].*

### 2.5.1. Fabrication of the Top Plane Micro-device

The fabrication of the top device is relatively simple. We fabricate the top device on a 4-inch Plan Optik Borofloat 33® glass wafer. The choice of the glass substrate is not necessary but can to some extent simplify the process of optically aligning the bottom plane with the top plane due to its transparency (described in detail later in Section 2.6). Fabrication of the top chip requires only a one-step lithographic patterning process using Microchem LOR lift-off resist and subsequent evaporative deposition of a 100 nm thick gold film. The lift-off photoresist is necessary to ensure

that the edges of all the electrodes have no spikes or burrs. After fabrication, the wafer is diced to create chips of desired dimensions and subsequently cleaned to ensure the creation of good devices. Figures 2.7a and b show respectively the SEM and dark field optical images of one such fabricated micro-device.

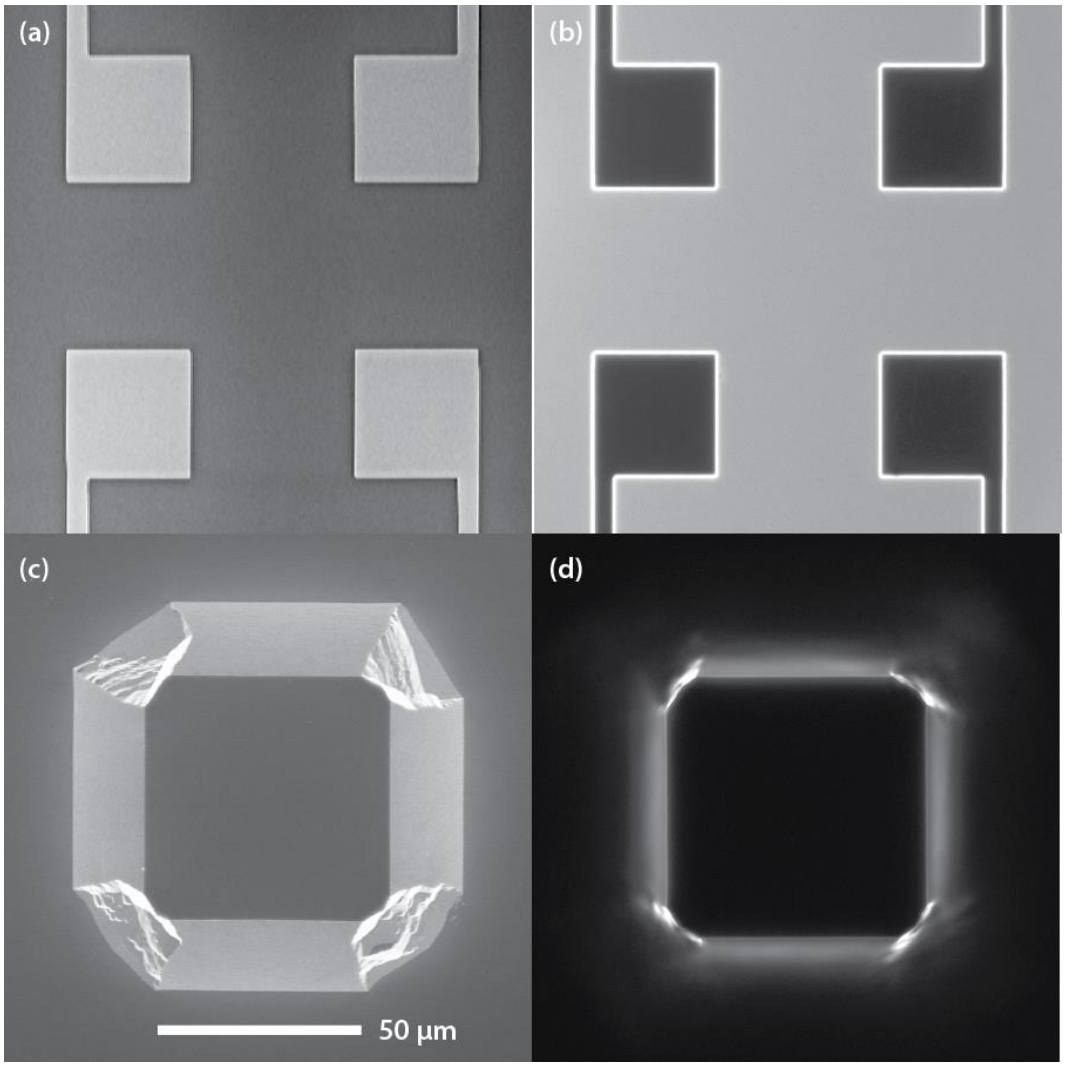


***Figure 2.7. Dark field optical microscope (DFOM) and scanning electron microscope (SEM) images of the micro-devices. a,*** *SEM and* ***b,*** *DFOM images of the top micro-device (with four gold contact pads);* ***c*** *and* ***d*** *are SEM and DFOM images of the bottom mesa device, respectively; figure adapted from [36].*

### 2.5.2. Fabrication of the Bottom Plane Micro-device

The mesa-shaped bottom device is made from a silicon wafer. As shown in Figure 2.8, fabrication of the mesa chip begins with the thermal growth of a ~1 μm thick silicon dioxide ($SiO_2$) film on top of a 4-inch (100)-oriented silicon wafer, followed by lithographic patterning of a ~60 × 60 $\mu m^2$ square $SiO_2$ region with ribs at the corners (Fig. 2.8) to allow for convex corner compensation [43]. Subsequently, a KOH wet, anisotropic etching step is performed to create the desired mesa structure with a square region on the top. The etching process is continuously monitored and stopped when the height of the silicon mesa is ~20 μm and an essentially square top mesa surface is formed. Without the ribs at the corners in the mask, the top surface would be more circular.

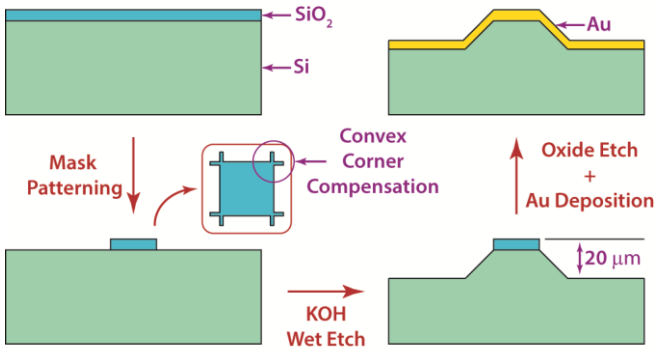


***Figure 2.8. Schematic of the fabrication procedure used to create the mesa micro-device**. The ribs at the corners of the square mask ensure that the final top surface of the mesa structure resembles a square; figure adapted from [36].*

After fabrication of the mesa structure, the wafer is diced into small chips under the protection of a thick layer of photoresist and cleaned with hot Baker PRS-2000 and piranha. Once the oxide mask on top of the mesa is etched away with buffered hydrofluoric acid, an ideal planar silicon surface appears. By carefully controlling the etching conditions, the etched area on the chip is

essentially parallel to the mesa surface. Finally, a 5 nm thick Cr adhesion layer and a 100 nm thick Au film are sequentially deposited all over the chip, which serves as an electrode in later experiments (details in Section 2.7). Figure 2.7c and d show an SEM and a DFOM image of the fabricated device, respectively. We note that in order to increase the yield of chips with desirable surface characteristics, it is necessary to take great care to ensure that the entire process is as clean as possible.

### 2.5.3. Characterization of the Micro-Devices and Precautions during Handling

After the chips were fabricated, the surface quality was examined using an AFM (Veeco, NanoMan VS). These studies, performed on multiple devices, suggest that the curvatures of both the top and bottom surfaces are essentially zero (see Fig. 2.9a, b). Further, it was ascertained from AFM measurements that the root-mean-square roughness of both the gold-electrode patterned glass surface (top device) and the gold-coated mesa surface (bottom device) is at most ~3 nm and is <1 nm for a majority of devices (Fig. 2.9b). The AFM scans could also easily identify chips with particulate contamination. However, it was not necessary to perform AFM scans on devices to detect particulate contamination as DFOM was found to be equally effective in detecting particles as small as a few nanometers in height. This was confirmed by characterizing the same chips using both AFM (Fig. 2.9c) and DFOM (Fig. 2.9d). By carefully characterizing the top and bottom micro-devices using AFM and DFOM, we ensure that all the devices used in the current study have a negligible curvature, and a surface roughness <3 nm. Further, we ensure that no particulate contaminants of appreciable size (larger than the surface roughness) are present on the surface.

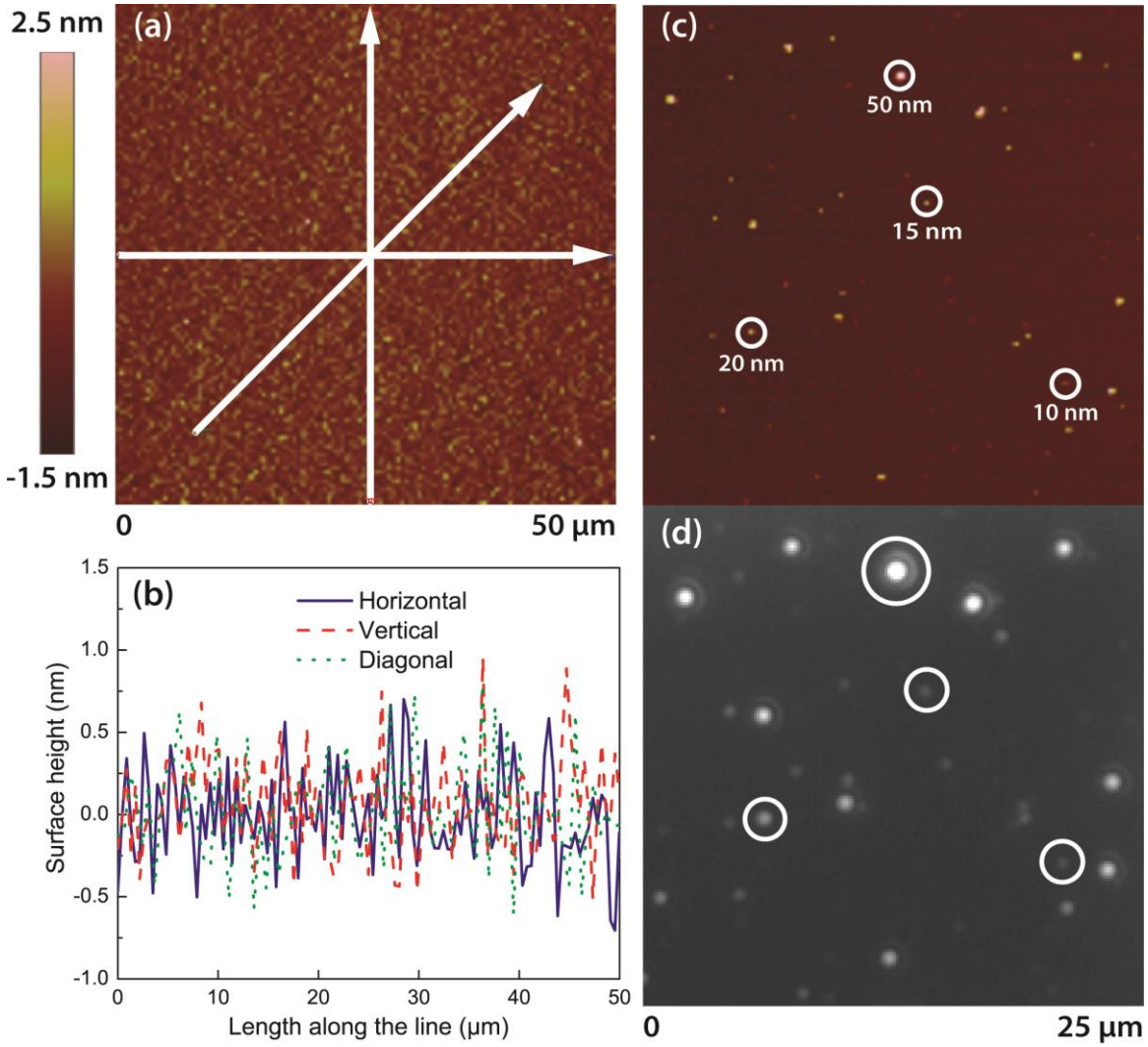


***Figure 2.9. Characterization of planarity, surface roughness and particle contamination. a,*** *AFM images of the top of a smooth and clean mesa surface and* ***b,*** *line profiles of the mesa surface. These data show that the mesa surface has no appreciable deviations from planarity and a very small surface roughness (< 1 nm rms). Similar results were obtained for the top surface (not shown).* ***c,*** *An AFM image of a mesa surface with particulate contamination and the corresponding (d) A DFOM image* ***d,*** *A comparison of the AFM and DFOM images shows that particles as small as 10 nm in size can be readily detected using DFOM with our microscope system (20 ms exposure with the CCD camera) and the describe device surfaces; figure adapted from [36].*

Once clean chips are prepared, it is of paramount importance to ensure that they remain clean for the experiments. To accomplish this, we used portable vacuum containers (Control Company

3163) for carrying the chips from cleanroom to the lab. Further, the nanopositioner was placed inside a custom-built laminar flow chamber (HEPA-filtered air) so that all the entire alignment procedure and experiments are conducted in a particle-free environment. Our tests show that once put inside the chamber, clean chips remain free of particulate contaminations for periods as long as a week.

## 2.6 Optical Approach to Facilitate Parallelization

In order to effectively parallelize the surfaces it is necessary to incorporate a tool that is capable of quantitatively detecting deviations from the desired parallelism. A variety of approaches can be used to this end, including capacitive sensing[18] and interferometry [44]. Here, we have implemented a simple optical approach (illustrated in Fig. 2.10), that uses a Zeiss microscope (Axiotech Vario) equipped with a long working distance (9 mm) and large magnification objective (Zeiss LD EC Epiplan-Neofluar 50×/0.55 HD). The long working distance objective is chosen as it provides the required spatial clearance for easy optical access to the planar surfaces of interest. At the same time, the numerical aperture (0.55) of the objective is sufficiently large to yield a shallow depth of field (~2 μm), which is essential for the optical alignment process as described below. The depth of field was confirmed experimentally by recording how the image of a point or a line changes during a through-focus imaging process (data not included).

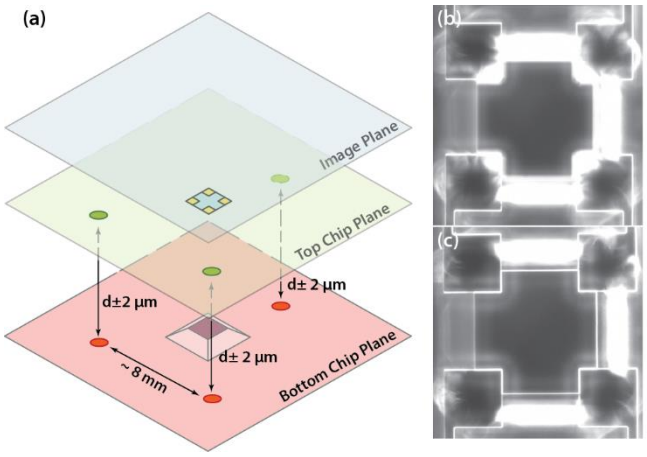


***Figure 2.10. Description of the scheme used to parallelize the top and bottom surfaces.*** *The optical alignment scheme ensures that corresponding points on the top chip plane and the bottom chip plane are at almost identical distances from each other ($d \pm 2$ µm). The microfabricated devices are not drawn to scale; figure adapted from [36].*

### 2.6.1. Alignment Approach

In the optical alignment approach (Fig. 2.10), the microscope objective is fixed rigidly while the bottom mesa chip is oriented using the kinematic mount (part 5 of Fig. 2.3) of the bottom subassembly to place the micrometer-sized mesa surface parallel to the image plane. This is done by sequentially translating three points on the chip surface, spatially separated by ~8 mm from each other, to the center of the field of view using the *xy* linear stage; and subsequently bringing each of them into focus using the tip-tilt mechanism so that the images of all three points are contained in the same image plane. This ensures that the vertical (*z*) separation of all the three points from the image plane differs at most by the depth of field of the objective, which is ~2 µm. As a result, the corresponding angular deviation between the mesa chip surface and the image plane would be less than 250 µrad (2µm / 8mm). This completes the alignment of the bottom surface.

Subsequently, a similar approach is used to tip and tilt the top glass chip using the custom-built goniometer of the top subassembly. This enables us to place the three points on the chip surface, spatially separated from each other by ~8 mm, into a single focal plane, with a small error set by the depth of field of the microscope objective. Again, the deviation in the vertical ($z$) position of the three points is within ~2 μm. Together, these simple alignment procedures ensure that, without any further corrections, the maximum angular deviation would be <500 μrad. Once the both surfaces are aligned, translational controls in the $xy$ plane are exploited to place the bottom surface right beneath the top surface. Thus, for a 60 × 60 μm$^2$ planar surface that meets the requirements described in section 3.4, the spatial deviation from parallelism ($p$) is expected to be at most ~30 nm (500 μrad × 60 μm). Note that in this particular set of experiments, the translational alignment process benefits from the transparency of the top chip as it allows easy optical access to the bottom device. However, the capability of our platform is by no means limited to the parallelization of transparent surfaces. For opaque devices such as those made from silicon wafer, a through-wafer etching can be applied to the surrounding area of the top device so that the bottom device can be seen through the hole. We note that the alignment approach described above does not enable us to achieve the parallelism that is, in-principle, achievable using the nanopositioner (see Table 2.1). However, if successful, the relatively simple optical approach described above enables superior parallelization without any other complicated devices such as capacitive sensors/interferometers or modification of device surfaces of interest. In the next section, we first independently quantify the parallelism achieved by the optical approach described here. Subsequently, we show that, by taking advantage of the electrodes integrated into the devices, it is possible to obtain improved parallelism with $p$ values of ~5 nm.

## 2.7 Improvement and Quantification of Parallelization Achieved Using the Optical Approach

In order to quantify the parallelism achieved by the optical approach we implemented a procedure that took advantage of the electrodes integrated into the top and bottom devices. In this procedure, a small voltage bias (~50 mV) was applied to the gold layer coating the bottom device (mesa structure), while each of the four electrodes of the top device was grounded and connected to four individual current amplifiers (see Fig. 2.6c). The current amplifiers serve to detect a contact between the top electrodes and the electrode on the mesa structure.

To quantify the parallelism between the surfaces, we begin by first laterally (*x*, *y* directions) aligning the top and bottom surfaces. After this alignment is accomplished, the four pads of the top devices are located directly above the four corners of the mesa structure as shown in Fig. 2.11.

Subsequently, the bottom surface (mesa) is first displaced towards the top surface using the coarse *z* positioner integrated into the bottom subassembly to reduce the separation between the two surfaces to within 15 μm: the travel range of the PI piezo actuator. After this is accomplished, the piezoelectric actuator is used to gradually reduce the gap between the top and bottom surfaces by moving the bottom surface towards the top surface at a very low speed (~2 nm/s). This is continued until the bottom surface momentarily touches one of the four gold pads integrated into the top surface (see Fig. 2.11). Upon contact, an electrical current flows through the bottom electrode and the top electrode involved in the contact. As soon as a contact is detected the piezoelectric actuator is immediately withdrawn using a simple control loop implemented on a computer with an A/D converter.

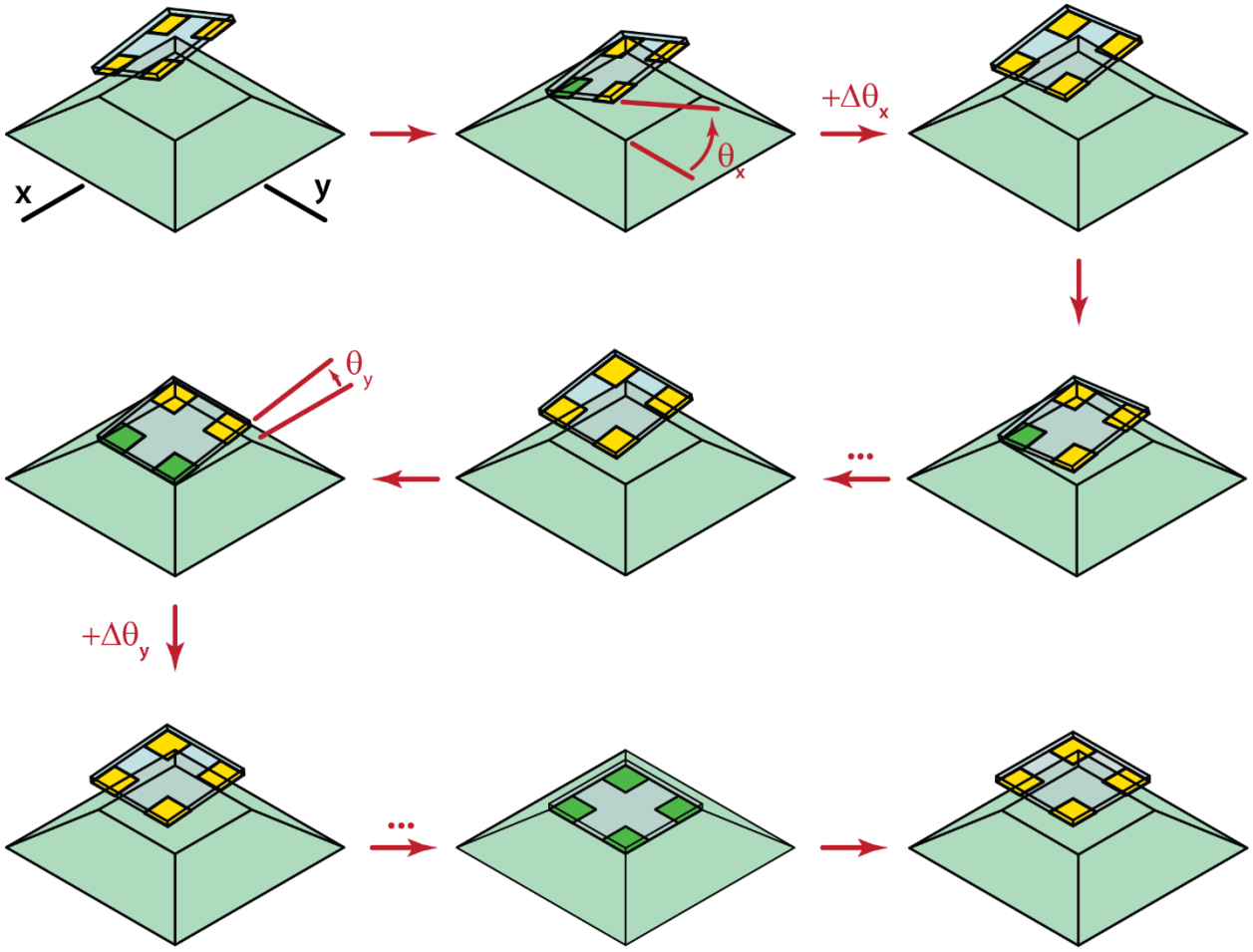


***Figure 2.11. Schematic drawing of the experimental process to quantify the parallelism achieved with depth-of-field based optical alignment.*** *In this procedure, the electrodes integrated into the top device and bottom devices are used to identify when a contact (indicated by green color) is made; figure adapted from [36].*

After withdrawing for a sufficiently large distance, the orientation of the top surface about the *x* axis is adjusted by a very small angle $\Delta\theta_x$ (typically ~25 μrad) using the motorized goniometer. The direction of rotation is chosen so that the pad which made the contact would be raised higher while the pad on the other side of *x* axis will be lowered. After reorienting the top surface, the bottom surface is brought up again to make a contact. If the same top electrode makes contact

again the above process is repeated. This process is continued until at least one of the pads located on the other side of *x* axis makes contact with the mesa (instead of the top electrode that made the initial contact). The total angular rotation $\theta_x$ required to accomplish this change in contact electrodes is recorded. This represents an upper bound to the angular deviation, from parallelism, around *x* axis.

After the above procedure is completed, the same procedure is then used to tune the angular position about *y* axis. The total angle tilted about *y* axis, $\theta_y$, which is the upper bound of the angular deviation around *y* axis, is also recorded. After the fine-tuning around both axes is completed, in almost all the experiments performed, four virtually simultaneous contacts (~2 seconds) are formed between the bottom electrode and each of the top electrodes as the bottom micro-device is driven into the top device at a slow speed (~2 nm/s). Figure 2.12 shows a typical example of contact during the piezo-driven approach of the two surfaces. As can be seen, the relative displacement of the piezo actuator from the first to the last contact is ~5 nm, which represents the maximum deviation from parallelism between the top and bottom electrodes after fine parallelization. This number is consistent with the observed surface roughness of the devices and the angular alignment accuracy of our nanopositioning system. The values of $\theta_x$ and $\theta_y$ recorded in a total of eight experiments with eight different pairs of devices with desired surface roughness are listed in Table 2.2.

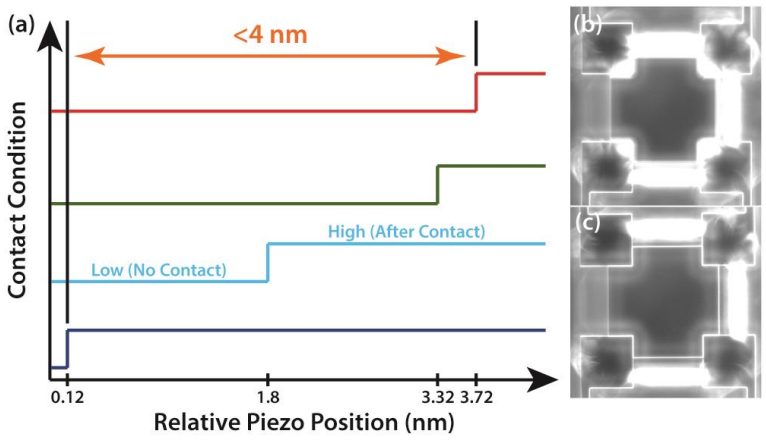


***Figure 2.12. Parallelization using integrated electrodes.*** *(a) A representative trace displaying the sequence of contact formation between the electrodes of the top and bottom device for an approach speed of 2 nm/s. Here, a low signal level indicates an open contact, whereas a high level is a sign of contact. After the first contact is made, the remaining three electrodes contact the bottom device within a displacement of <4 nm. The displacement range over which the contacts are made is independent of the approach speed (0.2 – 10 nm/s, N=8) and is consistently smaller than 5 nm. However, the sequence in which the pads make contact may differ between experiments. (b) A dark-field optical microscope (DFOM) image of the top and bottom devices that are spatially separated by a few microns (after optical alignment). (c) A DFOM image when all four top device's electrodes make electrical contact with the electrode of the bottom device; figure adapted from [36].*

| No. | 1 | 2 | 3 | 4 | 5 | 6 | 7 | 8 |
|---|---|---|---|---|---|---|---|---|
| $\theta_x$ (µrad) | 180 | 360 | -120 | 540 | 60 | 360 | 150 | 210 |
| $\theta_y$ (µrad) | 0 | 0 | 0 | 0 | -250 | -90 | 240 | -210 |
| Estimated spatial deviation from parallelism, *p*, after optical alignment (nm) | 11 | 22 | 7 | 32 | 20 | 27 | 23 | 25 |

***Table 2.2.*** *The angular rotations about the x and y axes to obtain four simultaneous contacts between the top electrodes and the bottom electrode. The measured spatial deviation from parallelism, in eight independent measurements, right after optical alignment is also provided; figure adapted from [36].*

The measured angles $\theta_x$ and $\theta_y$ are sufficient to calculate the spatial deviation from parallelism *p*, achievable by the optical alignment approach as described in section 2.6. To understand this, we begin by noting that the effect of rotations about the *x* and y axes can be represented by rotation operators $R_x$ and $R_y$ that have the following form in the Cartesian coordinate system:

$$R_x = \begin{bmatrix} 1 & 0 & 0 \\ 0 & \cos\theta_x & -\sin\theta_x \\ 0 & \sin\theta_x & \cos\theta_x \end{bmatrix}, \quad R_y = \begin{bmatrix} \cos\theta_y & 0 & \sin\theta_y \\ 0 & 1 & 0 \\ -\sin\theta_y & 0 & \cos\theta_y \end{bmatrix} \tag{1}$$

Given an arbitrary 3D vector $\mathbf{r}_i$ representing a point on the top planar surface before fine tuning, the corresponding vector after the final tip and tilt adjustment, $\tilde{\mathbf{r}}_i$, is simply

$$\tilde{\mathbf{r}}_i = R_y R_x \mathbf{r}_i \tag{2}$$

Consequently, the formula for calculating $\mathbf{r}_i$ from $\tilde{\mathbf{r}}_i$ would be

$$\mathbf{r}_i = R_x^{-1} R_y^{-1} \tilde{\mathbf{r}}_i \tag{3}$$

From this expression, it is easy to see that the position vectors of the corners of the top plane ( $\mathbf{r}_1, \mathbf{r}_2, \mathbf{r}_3, \mathbf{r}_4$, see Fig. 12) after the optical alignment, can be related to the positions of the corners ( $\tilde{\mathbf{r}}_1 = (a, a, 0),\ \tilde{\mathbf{r}}_2 = (-a, a, 0),\ \tilde{\mathbf{r}}_3 = (-a, -a, 0),\ \tilde{\mathbf{r}}_4 = (a, -a, 0)$ ) after establishing four simultaneous contacts, where *a* is half the length of the square (see Fig. 2.13). Further it can be seen that the spatial deviation from parallelism (*p*) can be obtained as:

$$p = \max\left[\left|(\mathbf{r}_1 - \mathbf{r}_3)\cdot\hat{k}\right|, \left|(\mathbf{r}_2 - \mathbf{r}_4)\cdot\hat{k}\right|\right] \tag{4}$$

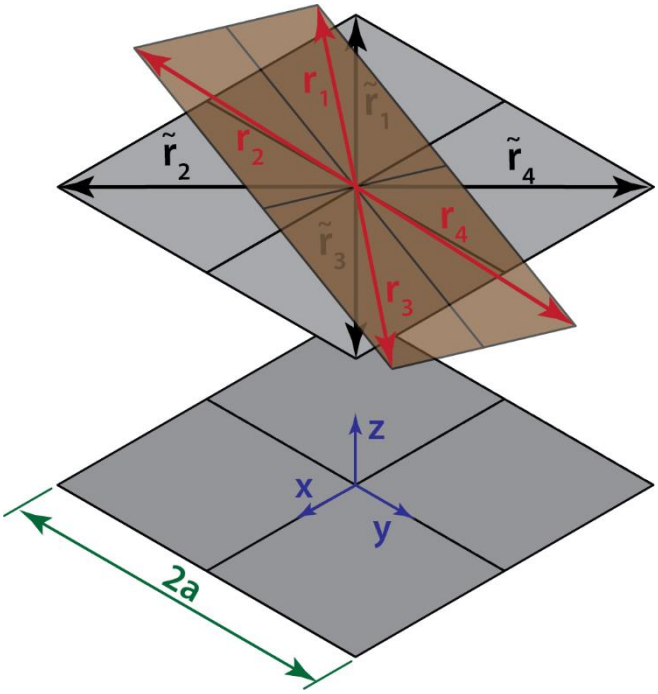


***Figure 2.13. Schematic describing the analysis of parallelization;*** *figure adapted from [36]*.

The values of *p* corresponding to each of the experiments performed above are listed in Table 2.2 and show that the deviations achieved in seven out of the eight experiments are within the estimated value of 30 nm, while one is slightly larger (32 nm). This unequivocally shows that the nanopositioner, which we built and described in section 2.3, combined with the depth-of-field based optical approach, has the capability to parallelize two planar surfaces of the area ~60 × 60 $\mu m^2$ with a spatial deviation from parallelism *p* as low as ~30 nm. In addition, this parallelism can be further improved by using the contact-based adjustment approach described above to reach values of $p \approx 5$ nm.

## 2.8 Conclusion

To summarize, we have described a nanopositioner that has the ability to parallelize two finite-area planar surfaces with respect to each other with angular resolutions of ~6 μrad about the *x* and *y* axes. This excellent angular resolution is achieved by using a goniometer that is controlled via the use of high resolution stepper motors. Further, the nanopositioner is also capable of controlling the spatial separation between the planes along the *z* direction with nanometer resolution. This is accomplished by the use of a coarse *z* positioner in conjunction with a high resolution piezoelectric actuator. Further, we have unambiguously demonstrated that using solely a simple optical approach, that relies on the shallow depth of field (~2 μm) of a microscope objective, it is possible to obtain very good parallelization ($p \approx 30$ nm) of micrometer sized surfaces (~$60 \times 60$ μm$^2$). We also demonstrated that this parallelization could be further improved ($p \approx 5$ nm) by a contact-based approach taking advantage of the electrodes integrated into the micro-devices. We show in the next chapter that that important new insights into NFRHT are obtained by combining this nanopositioning system with ultra-high resolution heat flow calorimetric techniques [35] presented earlier.

**Contributions:** All of the results presented here have been made possible due to contributions from my colleagues. More specifically, the picowatt-resolution calorimeter was designed and fabricated by S. Sadat and experiments were conducted using W. Lee's setup. Furthermore, the experiments were done by Y-J. Chua and me. I designed and built the nanopistioner in collaboration with B. Song and the microdevices used were designed by us and fabricated by K.K. Pagadala, S. Sadat, and K. Kim. All the experiments were run by B. Song and me.

# CHAPTER 3

# Nanoscale Dielectric Coatings Enhance Near-Field Thermal Radiation

**Acknowledgement:** This chapter is based on text extracts from our paper, which first appeared in Nature Nanotechnology [45].

## 3.1 Introduction

In chapter 1, it was demonstrated that thermal radiation plays an important role in many applications including but not limited to energy conversion, thermal management, lithography, data storage, and thermal microscopy. A review of recent studies on bulk materials showed that when the spatial separation between hot and cold surfaces is reduced to nanometers, well below the peak wavelength of the blackbody spectrum, radiative heat fluxes increase by orders of magnitude due to NFRHT. However, all these enhancements were observed in bulk materials and whether such enhancements can be engineered with nanoscale dielectric films thinner than the penetration depth of radiation remains experimentally unknown. Here, using the experimental

platform presented in chapter 3 that includes a picoowatt resolution heat-flow calorimeter [34] and the 6 degree-of-freedom nanopositioner, the first direct near-field radiation measurements from devices with nanoscale dielectric coatings are conducted. The results show dramatic increases in radiative heat transfer—comparable to those obtained between bulk materials—even for very thin dielectric films (50 - 100 nm) at spatial separation between the surfaces comparable to the film thickness. These results are explained by analyzing the spectral characteristics and the mode shapes of surface phonon polaritons, which dominate near-field radiative heat transport in polar dielectric thin films. These results have important implications to thermo-photovoltaic [1] and other technologies that seek to leverage near-field radiative heat transfer [2, 46-50].

## 1.2 Experimental Measurement of Enhancement in Thermal Radiation due to NFRHT from Thin Dielectric Coatings

While the theoretical predictions presented in chapter 1 have existed for a long time [3, 5, 7, 12, 37, 51], only recently measurements from bulk materials using either scanning probes with integrated thermal sensors [52] or bimaterial cantilever-based calorimeters [24, 26] have provided experimental support of striking enhancements in radiative heat transfer at the nanoscale. In spite of this important progress several fundamental predictions of NFRHT have remained unexplored. As mentioned in chapter 1, one of the most interesting predictions pertains to the thickness dependence of NFRHT and suggests that even nanometer-thick dielectric films dramatically enhance NFRHT in nanoscale gaps between dielectrics [7, 11, 29, 53]. While a recent paper has attempted to study the effect of a dielectric monolayer on NFRHT between one bare Au-surface and a second Au-surface coated with a monolayer of NaCl, the experimental results obtained in that work defy any theoretical or computational explanation [54]. Further, in that work elucidation

of NFRHT was also impeded by the inability to quantitatively measure heat currents. Thus, to date no experimental studies have characterized the interesting predictions of gap and film thickness dependent NFRHT enhancements despite their technological implications.

To experimentally study the dependence of NFRHT on film thickness we developed an ultra-sensitive, micro-fabricated calorimetric platform very similar to those presented in chapter 2 that enables quantitative studies of gap size-dependent heat currents from a spherical hot surface (called emitter) to a planar, colder surface (called receiver) for a broad range of film thicknesses (Fig. 3.1). We precisely control the gap size between the spherical emitter and the planar receiver from as small as 20 nm to as large as 10 μm using the custom-built nanopositioning platform (chapter 2), while simultaneously measuring heat currents between them to obtain the thermal conductance as a function of gap size. Further, the formation of contact between emitter and receiver is optically monitored (Fig. 3.1a). Details of the experimental process are given below.

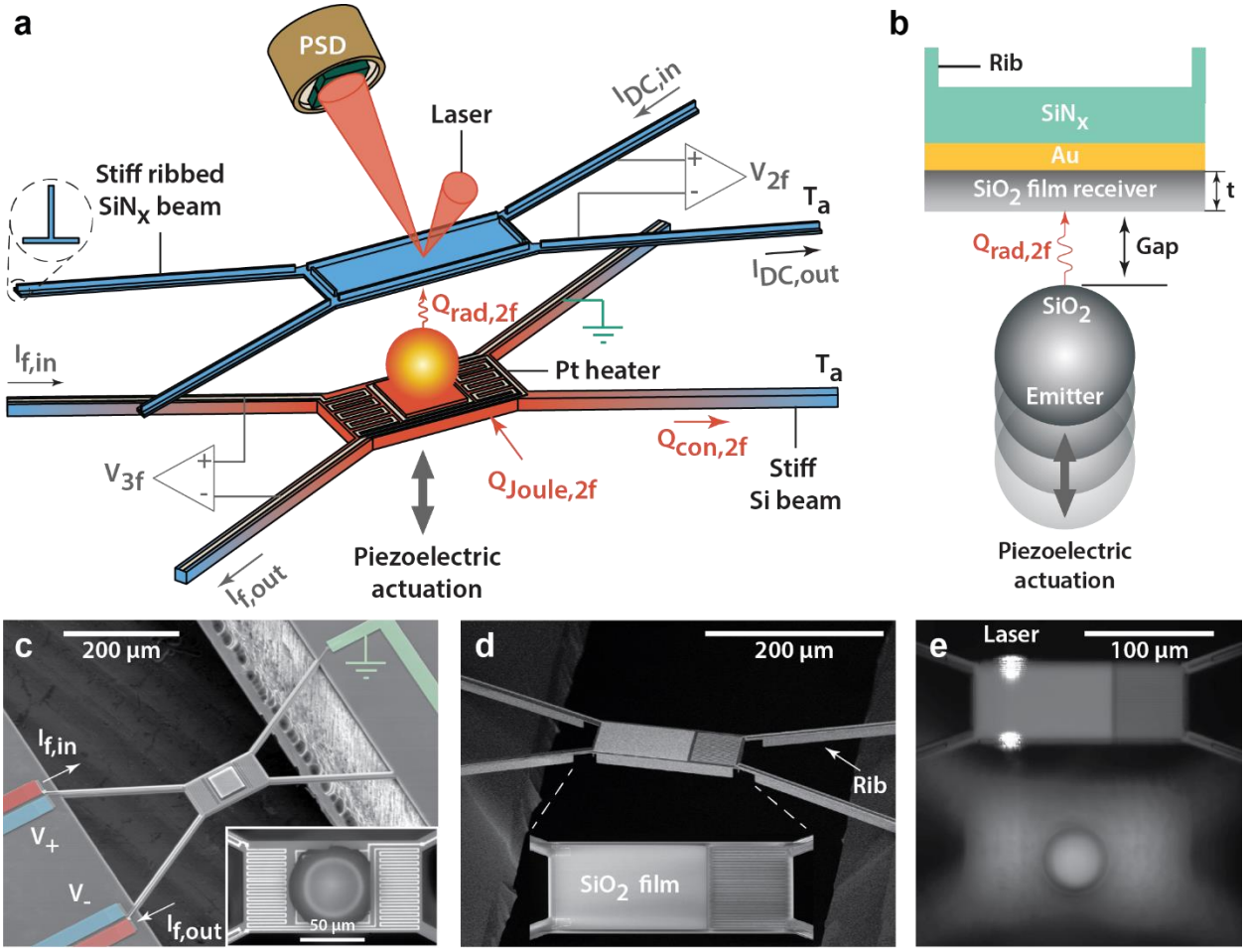


***Figure 3.1. Experimental setup. a,*** *Schematic of the experimental setup. The emitter consists of a suspended silicon platform, with an attached silica sphere, and an integrated electrical heater-thermometer. The receiver is a stiff silicon nitride platform coated with gold and a silica film of suitably chosen thickness. A laser (reflected off the receiver, see also* ***e****) and a position sensitive detector (PSD) enable optical detection of emitter-receiver contact formation with nanometer resolution.* ***b,*** *Schematic cross section of the planar receiver region and the spherical silica emitter. The gold layer is ~100 nm thick, the thickness (t) of the $SiO_2$ film varies from 50 nm to 3 µm for different receiver devices.* ***c,*** *Scanning electron microscope (SEM) image of the suspended platform and optical image (inset) of the spherical emitter.* ***d,*** *SEM images of the receiver show ribbed beams and suspended regions.* ***e,*** *An optical image of the emitter and receiver during alignment. In this image the devices were laterally displaced to enable simultaneous visualization; figure adapted from [45].*

### 3.2.1. Fabrication and Preparation of Microdevices

**Fabrication of Receiver Device:** The key steps involved in fabricating the receiver devices are shown in Fig. 3.2a. Starting with a 500 µm-thick p-type silicon (Si) wafer, 800 nm-wide (patterned using optical lithography) and 10 µm-deep trenches are etched using deep reactive ion etching (DRIE) (Step 1). A 150 nm-thick, wet thermal silicon dioxide ($SiO_2$) layer is then grown to further decrease the width of the trenches (Step 2). Subsequently, low-pressure chemical vapour deposition (LP-CVD) of a 1 µm-thick layer of low-stress silicon nitride ($SiN_x$) is performed, which forms the device membrane together with the ribs as the trenches are filled up with $SiN_x$ (Step 3). Once the structural elements of the devices are prepared, the electrical components, including the 30 nm-thick platinum (Pt) resistance heater-thermometer (Step 4) and the 100 nm-thick gold (Au) pads and electrical connections (Step 5), are deposited via successive lift-off processes using electron-beam (e-beam) evaporation on a 3 nm-thick chromium (Cr) layer deposited first to improve the adhesion. The next steps are to suspend the devices to achieve good thermal isolation. To this end, reactive ion etching (RIE) of the $SiN_x$ film is performed first on the front side of the wafer to carve out the device profile (Step 6), and then on the back side to allow access to the Si substrate (Step 7) for further processing. The wafer is subsequently etched with a 30% aqueous potassium hydroxide (KOH) solution at 85 ºC until the device is suspended (Step 8). The buried wet $SiO_2$ layer covering the suspended device is now exposed and etched away with buffered hydrofluoric acid (BHF), leaving behind a ribbed structure made of $SiN_x$ (Step 9). Finally, $SiO_2$ films of various thicknesses (50 nm, 100 nm, 1 µm, 2 µm and 3 µm) are formed on individual devices using low-temperature plasma-enhanced chemical vapor deposition (PE-CVD) (Step 10).

**Fabrication of Emitter Device:** Major fabrication steps for the emitter devices are illustrated in Fig. 3.2b. The process utilizes a Silicon-on-Insulator (SOI) wafer with a 500 µm-thick Si substrate layer, a 1 µm-thick buried oxide (BOX) layer and a 10 µm-thick Si device layer (Step 1). A 500 nm-thick low-stress LP-CVD $SiN_x$ film is first deposited on the wafer to electrically insulate subsequent patterns from the device layer (Step 2), followed by deposition of a 2 µm-thick layer of low-temperature LP-CVD $SiO_2$ (Step 3). The $SiO_2$ layer is then etched using RIE to form a square pad (Step 4) onto which a silica ($SiO_2$) microsphere will be glued (Fig. 3.3). Subsequently, the Pt resistance heater-thermometer and the electrical connection patterns are transferred onto the $SiN_x$ layer using successive lift-off processes (Step 5). The device profile is then formed by RIE etching of the $SiN_x$ layer and the Si device layer using the same mask pattern from the front side of the wafer, stopping at the BOX layer (Step 6). Subsequently, the $SiN_x$ layer and the $SiO_2$ layer on the back of the wafer are selectively etched with RIE to open a window for further processing (Step 7). To suspend the device, the bulk Si substrate is etched using through-wafer DRIE from the back, which stops at the BOX layer (Step 8). Finally, the BOX layer is etched using BHF (Step 9).

### 3.2.2. Microsphere Cleaning and Attachment

In order to create a functional emitter device with a spherical surface, silica microspheres with a nominal diameter of 53 µm (Corpuscular Inc.) are cleaned and attached to the fabricated emitter devices. A representative confocal laser scanning microscopy (CLSM) image of spheres as obtained from the manufacturer is shown in the inset of Fig. 3.3a. The cleaning procedure starts by dispersing microspheres in clean, deionized (DI) water, followed by repeated high-speed vortexing and high-power ultrasonication. This process removes a majority of the contamination,

and clean microspheres that are suitable for measurements are readily obtained (Fig. 3.3a). Additional surface characterization was performed using atomic force microscopy (AFM), see Fig. 3.6a-c, to confirm that the cleaned spheres have a smooth surface (RMS roughness < 3 nm). Once a clean sphere is identified, it is attached to the emitter device with the aid of an optical microscope using a 3-axis micropositioner equipped with either micrometre-sized wires or needle probes and two different mounting adhesives as described below.

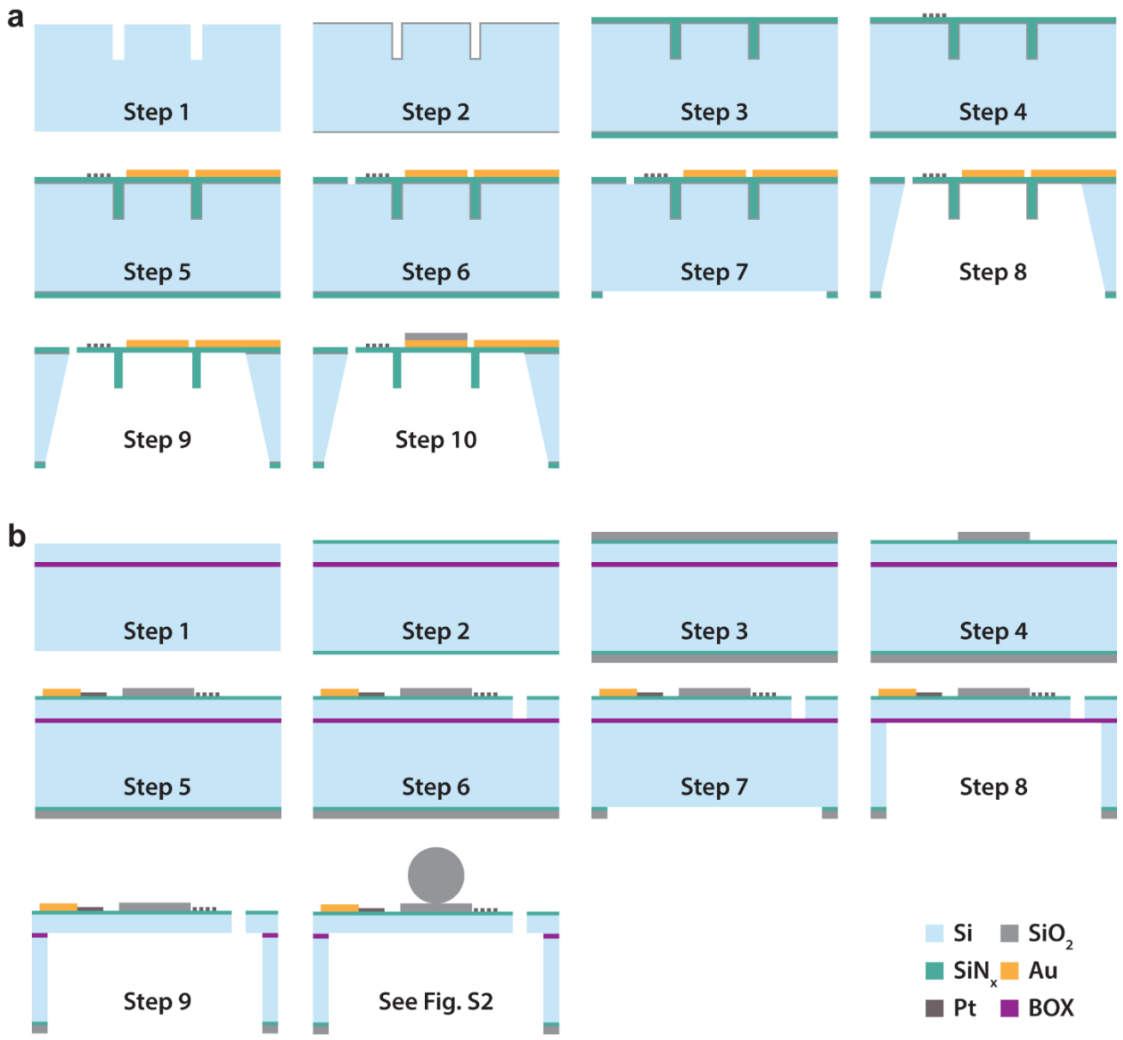


***Figure 3.2. Fabrication process for the receiver and the emitter microdevices. a****, The receiver device with ribbed structure.* ***b****, The emitter device fabricated on a SOI wafer; figure adapted from [45].*

We first use a Au wire (diameter ~20 μm, Fig. 3.3b) to transfer a small volume (~ 1 nl) of Crystalbond (CB) 509 (acetone-soluble adhesive, flow point 121 °C) to the square pad of an emitter device (Fig. 3.3c). To place a microsphere on an emitter, we coat a sharp, thoroughly cleaned tungsten (W) needle with a very small amount of CB555 (a water-soluble adhesive with a flow point of 66 °C), bring it into lateral contact with the selected sphere and transiently heat the W probe to melt the adhesive and attach the sphere (Fig. 3.3d, inset). Next, the emitter device is heated again (to melt the deposited CB509) and the tethered sphere is brought into contact with the emitter. Subsequently, the emitter device is cooled and the wire is heated (>66 °C), allowing the attachment of the sphere onto the emitter and the separation of the needle from the sphere (Fig. 3.3d). Finally, the entire device is cleaned in DI water to remove excess, water-soluble CB555 from the surface of the microsphere (Fig. 3.3e-f). Note that the sphere remains attached to the emitter device as CB509 is not water soluble.

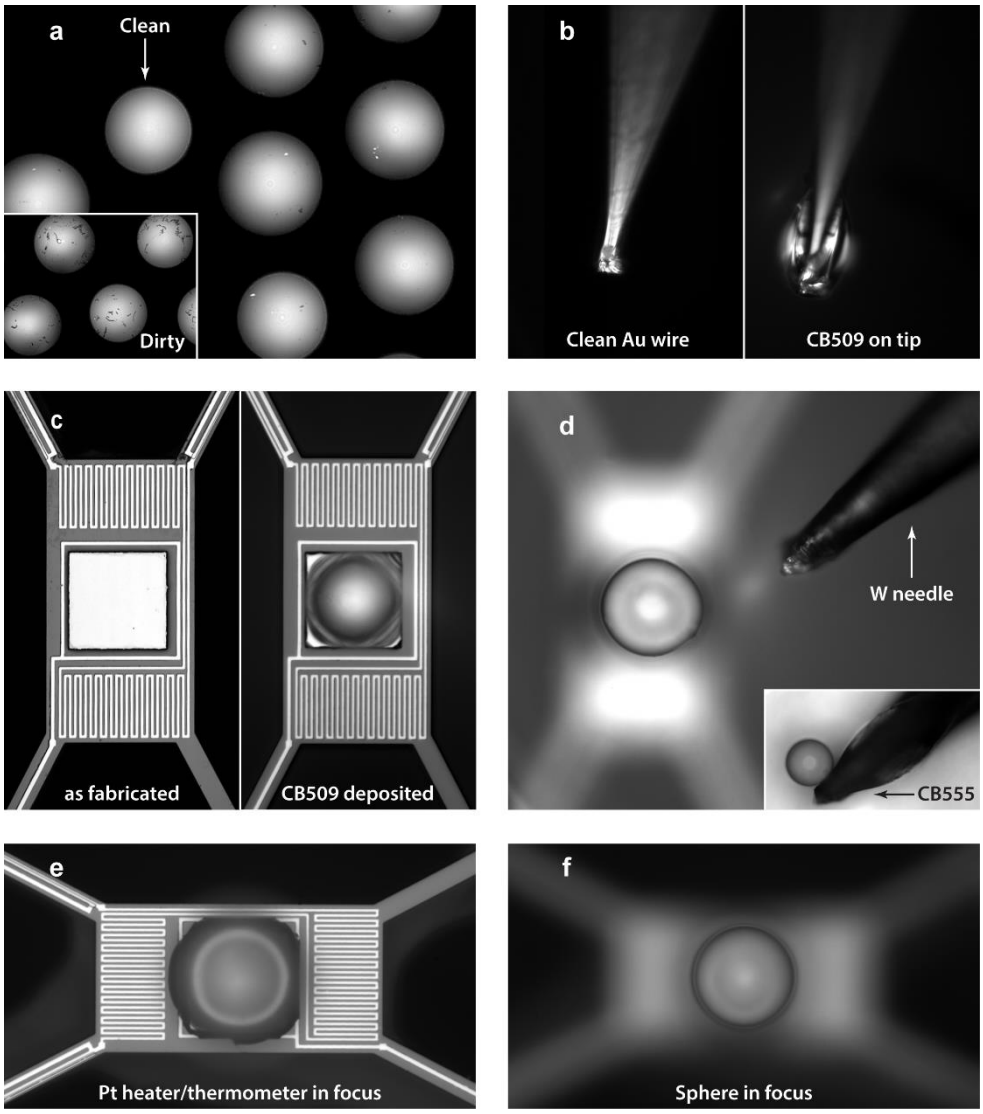


***Figure 3.3. Cleaning and attaching the microspheres onto fabricated emitter devices. a****, Confocal laser scanning microscopy images of cleaned spheres (inset shows an image of uncleaned, commercial spheres).* ***b****, Cleaned, micrometre-sized Au wire, before and after a nanolitre volume of CB509 was transferred and solidified on its tip.* ***c****, Micro-fabricated emitter device before and after CB509 is deposited. The square, gold loop surrounding the central region of the device is used for grounding.* ***d****, Microsphere attached to a CB555-coated, sharp W needle and transferred to the CB509-coated emitter device.* ***e*** *and* ***f****, An emitter device with integrated sphere after DI water rinse. Image (****e****) is focused on the Pt heater-thermometer while (****f****) shows the top of sphere in focus. Images* ***b****–****f*** *were obtained using reflected brightfield microscopy; figure adapted from [45].*

### 3.2.3 Thermal Characterization of Microdevices

The thermal characteristics of the microdevices are of crucial importance to NFRHT measurements. In order to accurately quantify these characteristics we employ both modelling and experiments. All experiments were performed in a high vacuum ($<10^{-6}$ Torr) environment as described below.

**Thermal Resistance within the Suspended Region of the Devices:** To confirm that the resistance to heat flow within the suspended regions of the emitter and the receiver devices is negligible compared to the thermal resistance within the beams we performed finite-element modelling (FEM). Specifically, we found that when heat is input in the suspended regions, the temperature field therein is essentially uniform and all the thermal gradients are primarily localized to the beams. The maximum deviation from average temperature is <1% for the emitter device and <5% for the receiver device, indicating that the thermal resistance to heat flow within the suspended region is negligible (Fig. 3.4a-b). This also implies that the thermal properties of the emitter and receiver devices can be accurately represented by lumped parameter models where the suspended region can be represented by a single temperature.

**Temperature Coefficient of Resistance:** The temperature coefficient of resistance (TCR, α) is defined as $\alpha(T) \equiv \frac{R(T+\Delta T)-R(T)}{R(T)\Delta T}$, where R(T) is the temperature-dependent electric resistance and ΔT is the change in temperature. TCRs were measured by controllably changing the temperature of the chosen device (in a vacuum cryostat) while monitoring the electrical resistance of the Pt heater-thermometer. The TCR of all individual devices was measured to account for

possible variability among devices. Figure 3.4c shows the measured Pt resistance for representative emitter and receiver devices as a function of temperature. As expected, the resistance changes linearly with temperature. Further, using the slope of the lines in Fig. 3.4c the devices' TCRs are obtained for various temperatures (Fig. 3.4d). The values are consistent with those reported by us in the past [34].

**Thermal Frequency Response:** The thermal frequency response of the devices refers to the dependence of the temperature oscillation amplitude on the heating frequency. It is measured by supplying a sinusoidal current $I_f$ with fixed amplitude and varying frequencies $f$ to the Pt heater-thermometer. This leads to sinusoidal Joule heating ($Q_{2f}$) in the device at $2f$ and corresponding temperature oscillations with an amplitude $\Delta T_{2f}$. As a result, a voltage component at $3f$, $V_{3f}$, is generated which is proportional to $\Delta T_{2f}$, and is given by the relationship $V_{3f} = \frac{\Delta T_{2f} \alpha I_0 R_{Pt}}{2}$ . The measured $\Delta T_{2f}$ (normalized to values obtained at the lowest frequencies employed in the measurement) as a function of the heating frequency is shown for representative emitter (Fig. 3.4e) and receiver (Fig. 3.4f) devices. As can be seen, the response is consistent with a first-order, linear, time-invariant system. The emitter devices show little attenuation (<5%) below 20 Hz, as-fabricated or with a sphere attached. For the receiver devices, the frequency response varies with the thickness of the $SiO_2$ films. For receiver devices with no $SiO_2$ coating, the frequency response is essentially flat up to 2 Hz. On the other hand, for devices coated with 3 μm-thick $SiO_2$ films, the response is slightly different with attenuation beginning at somewhat lower frequencies. This results in a slight attenuation in the response (~20%) at 2 Hz. The frequency response curves for devices with intermediate coating thickness fall in between the two extremes.

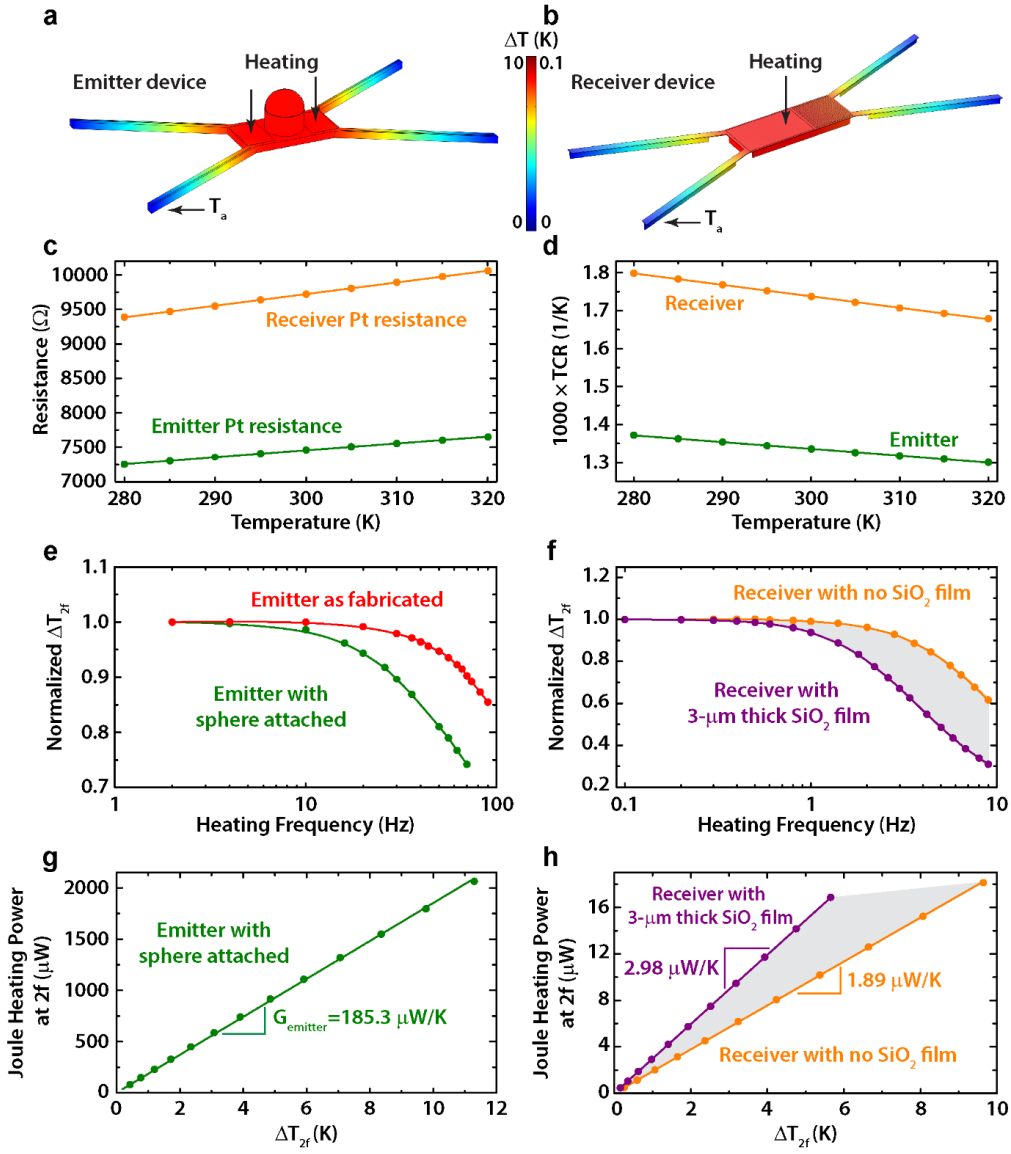


***Figure 3.4. Thermal characteristics of the microdevices.*** *a-b, FEM thermal simulation of emitter (a) and the receiver (b) devices showing the temperature distribution for heating scenarios comparable to a real experiment. It can be seen that there are negligible temperature gradients within the suspended region. c-d, Temperature dependence of the Pt resistance (c) and the corresponding TCR (d). e-f, Thermal frequency response of the devices. Measured thermal conductance of the beams isolating the suspended region of the emitter (g) and receiver (h) from the bulk substrate; figure adapted from [45].*

**Thermal Conductance of the Beams:** In order to characterize the thermal conductance of the beams of the emitter and receiver devices we supply a sinusoidal current $I_f$ with varying amplitudes

at a fixed frequency $f$ to the Pt heater-thermometer. This results in Joule heating ($Q_{2f}$) and temperature oscillations ($\Delta T_{2f}$) at $2f$ as described above. Representative measured results are shown for the emitter (Fig. 3.4g) and the receiver (Fig. 3.4h) devices. From this data the conductance of the beams was extracted by fitting the data to the following relationship, $Q_{2f} = G_{Beams} \times \Delta T_{2f}$ . In order to ensure good signal quality and a reasonable experiment duration, we used a 2 Hz (=$2f$) heating frequency in all measurements. Corrections based on the measured thermal frequency response were applied when needed. From these measurements the beam conductance of the emitter devices, $G_{emit}$, was found to be ~180 μW/K and is much larger than the conductance of receiver devices ($G_{rec}$) which were typically ~2 μW/K.

**Thermal Expansion of Emitter Device:** In order to understand if the thermal modulation of the emitter device results in significant changes of the position of the sphere, we performed finite element modelling using a coupled electrical, thermal and mechanical model that fully accounts for the bimaterial effects arising from all thin films. In these simulations we used the following boundary conditions: 1) the ends of the beams where they connect to the substrate are assumed to be fixed; this is valid because the substrate is not undergoing any temperature increases; 2) a temperature boundary condition of 295 K was used at the ends of the beams. Further, we assumed that the thermal expansion coefficients of Pt, Si3N4 and Si, are 8.8×10-6 $K^{-1}$, 2.3×10-6 $K^{-1}$, and 2.6×10-6 $K^{-1}$, respectively. The Young's moduli and all other relevant physical parameters were obtained from [55-57].

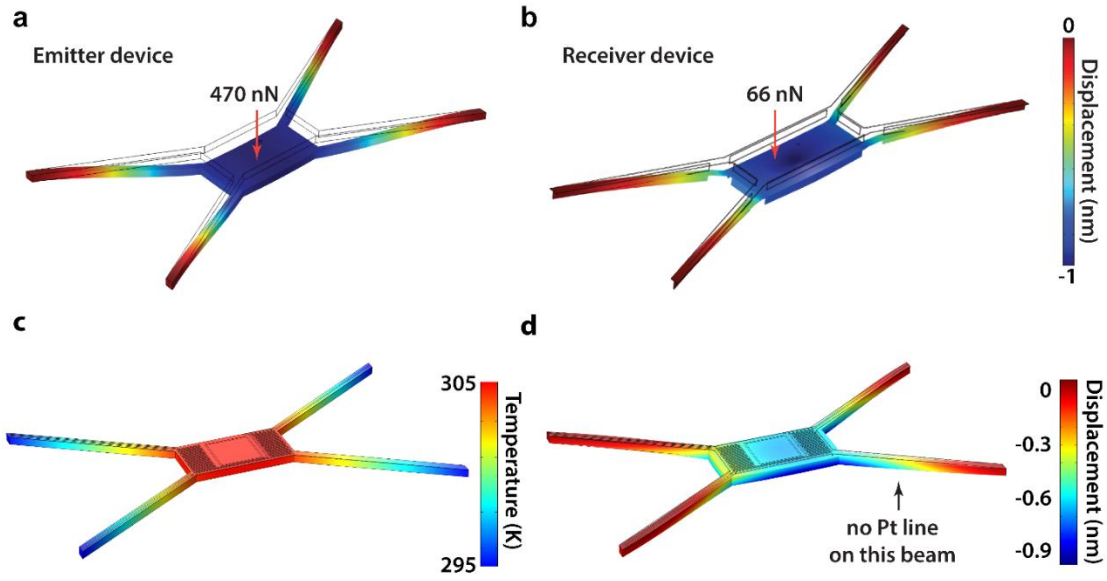


***Figure 3.5. FEM simulation for the stiffness, temperature profile and thermally-driven deflection of the microdevices. a****, Deflection of the SOI wafer-based emitter device in response to a point load applied to the suspended region.* ***b****, Same as in* ***a,*** *but for the receiver device. The displacement scale bar applies to figures a and b.* ***c****, Computed temperature profile of the emitter device. The heat dissipation in the electrical heater is set such that the temperature increases by 10 K in the suspended region whereas the temperature at the ends of the beam remains at room temperature assumed to be 295 K. d, Computed deflection of the emitter device due to a temperature rise of 10 K. The central region of the device deflects down by ~1 nm due to the bimaterial structure of three of the beams (the beam without the Pt film is labelled, also see Fig. 3.3e which depicts the exact Pt patterns on the device), which have a thin Pt film deposited on them for electrical connections. The ends of the beams are assumed to be fixed rigidly to the substrate; figure adapted from [45].*

In implementing the model we simulated Joule heating in the device by applying an electric current to the heater until the device temperature rose by 10 K in the central region (Fig. 3.5c). Using this coupled model we computed the deflection of the device due to thermally induced stresses. The obtained deflections are shown in Fig. 3.5d. The maximum deflection is in the central region of the device and is <1 nm in the downward direction. The deflection profile is slightly asymmetric as the thin Pt films are asymmetrically deposited on the beams (see Fig. 3.3e). Thus, thermally-

driven deflections of the emitter devices do not affect our measurements as such deflections are much smaller than the gap-sizes of interest in our study.

### 3.2.4. Structural and Surface Characterization

Structural and surface characteristics such as the stiffness, flatness, roughness and cleanliness of the microdevices determine the minimum achievable gap size between the emitter and the receiver. Consequently, proper measures were taken in every phase of the device fabrication and handling to ensure that devices remain uncontaminated and have all the characteristics required for performing the desired measurements.

**Stiffness and Flatness:** In order to perform NFRHT measurement across nanometre-sized gaps, both the emitter and receiver devices have to be very stiff so any force that may be present between the two, be it electrostatic, Casmir or Van der Waals force, does not cause significant mechanical instabilities, which compromise the ability to create nanometre-gaps. To optimize the devices for thermal conductance and stiffness the emitter device was made of a 10 μm-thick layer of single crystal silicon whose dimensions can be found in Fig. 1c. Its stiffness is estimated to be ~500 N/m using FEM (Fig. 3.5a). The receiver device, which is used for high-resolution radiative heat flow measurements, is made of a 1 μm-thick $SiN_x$ membrane to ensure good thermal isolation. In order to enhance the beam stiffness without causing a large increase in the thermal conductance, the beams of the emitter were fabricated to have a T-shaped cross-section (Fig. 1d) resulting in a stiffness estimated to be 66 N/m using FEM for the device without $SiO_2$ coating (Fig. 3.5b). The stiffness increases monotonically upon increasing the thickness of the $SiO_2$ layer and increases to values as high as 160 N/m for devices coated with 3 μm-thick SiO2 layers. Given the excellent stiffness of these devices, we were able to make measurements at single-digit nanometer separation

as device “snap-in” due to the aforementioned forces was avoided even for such small gaps. The snap-in distances were directly quantified by recording force-distance curves using a procedure similar to that in the field of atomic force microscopy [58]. These measurements confirmed that the snap-in distances were <5 nm for all devices, including the most compliant, which had a stiffness of 66 N/m as estimated from FEM simulations. It should be pointed out that snap-in distances in this size range have previously been described, even for much larger devices that are more prone to electrostatic snap-in, in the classic experiments of Tabor and Winterton [59, 60]. We note that the emitter device includes a grounding loop on the planar region of the devices that surrounds the sphere. Further, the gold layer in the receiver devices underneath the $SiO_2$ films is also grounded. These precautions help eliminate any electrostatic charges that may develop on the surfaces of the emitter and the receiver during their assembly. Thus, our observations of snap-in distances below 5 nm are consistent with previous work and the precautions taken by us to mitigate the effects of electrostatic interactions.

We note that the devices are also extremely flat. Both FEM and CLSM show that the emitter device is as flat as the bulk Si substrate. The thin-film receiver devices with $SiO_2$ coatings thinner than 100 nm (including Au surface with no coating) show also extremely small curvature in the suspended region of interest, roughly equivalent to a sphere with a diameter of ~20 mm. The curvatures of the devices with thicker $SiO_2$ films are slightly larger, similar to that of a sphere with a diameter of ~2 mm, However, such curvatures are still negligibly small compared to the curvature of the spherical surface (nominal diameter 53 μm) used as the emitter, validating the use of a sphere-plane model for NFRHT studies.

**Roughness:** The surface roughness of the spherical emitters and planar receivers was characterized using AFM. Multiple silica microspheres and multiple spots on each sphere incorporated in the emitter devices were examined, and the surfaces of all receiver devices were characterized using scan areas ranging from 10 μm × 10 μm to as small as 1 μm × 1 μm. Representative images are shown in Fig. 3.6. It can be seen that the roughness of the spheres (Fig. 3.6a-c) is very small, with an average root mean square (RMS) surface roughness $S_q$ (as defined in ISO 25178) of ~1 nm (Fig. 3.6b, bottom). Peaks with few-nanometre height, although present, are rare. Further, the excellent sphericity of the microsphere is demonstrated by how well different profiles overlap with each other (Fig. 3.6b, top). The roughness of the receiver films (Fig. 3.6d-j) shows a dependence on the film thickness, with thicker ones being rougher. The 100 nm-thick films (Fig. 3.6d-f) feature an average $S_q$ of ~3 nm, while the average $S_q$ of the 3 μm-thick films (Fig. 3.6g-i) is ~10 nm.

In nanoscale NFRHT measurements, knowledge of the surface topography is important in estimating the effective gap size between the emitter and the receiver. Since the exact surface characteristics at the locations where the sphere and plane are in the closest proximity are not known we need to rely on statistical descriptors (RMS surface roughness and peak roughness) to relate contact of the surfaces (as detected experimentally in our measurements, see below) to an effective gap size. Although informative, the RMS roughness $S_q$ will underestimate the minimum (effective) gap size because larger peaks on the surface tend to prevent contacts within the RMS roughness. On the other hand, the use of peak roughness likely leads to overestimates of the effective gap. Therefore, we define a threshold height beyond which on average only 3 peaks extend in a 1 μm × 1 μm region (Figs. 3.6e and h, lower). This threshold height represents our best

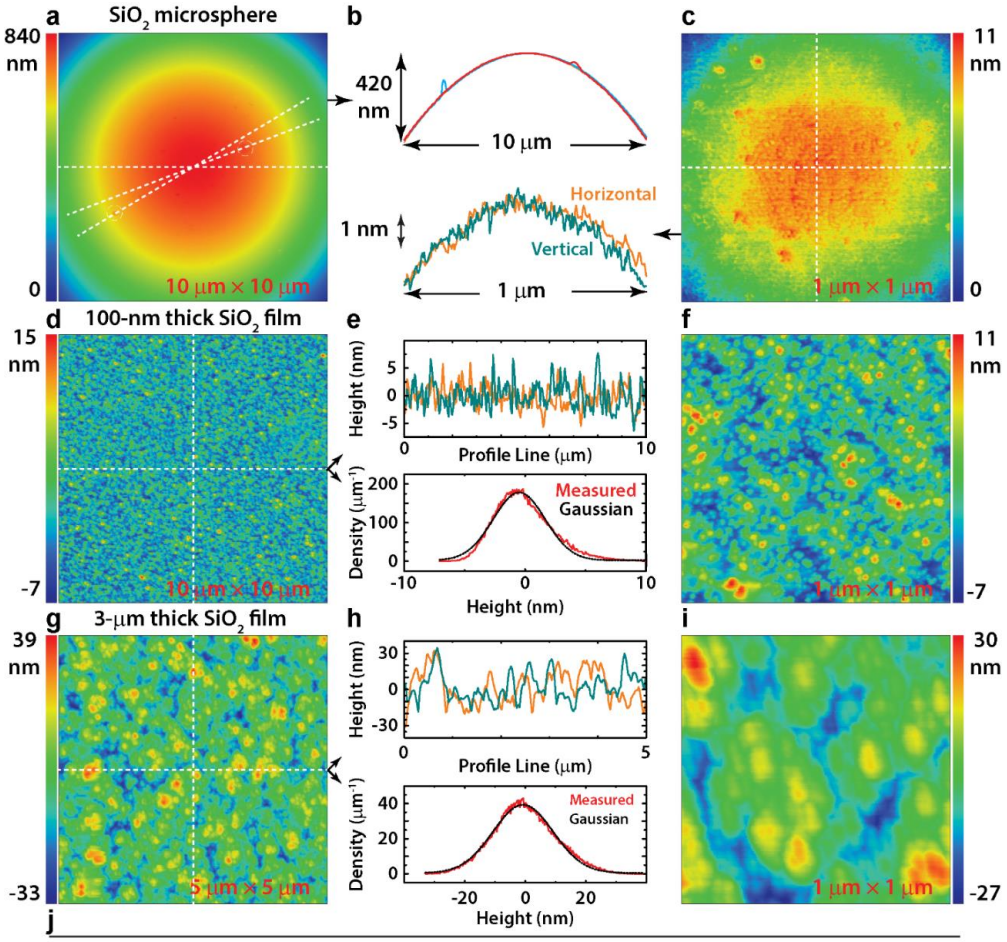


| $SiO_2$ Film Thickness | 0 nm (Au) | 50 nm | 100 nm | 1 μm | 2 μm | 3 μm |
|---|---|---|---|---|---|---|
| $S_q$ (nm) | 2 | 3 | 3 | 7 | 9 | 10 |
| Threshold Height (nm) | 6 | 10 | 11 | 18 | 19 | 21 |

***Figure 3.6. Surface characteristics of the microdevices. a-c,*** *AFM topography images and selected line profiles (indicated by the white lines in* ***a***, ***c****) of a representative silica microsphere.* ***d-f****, AFM topography images (****d****,* ***f****), line profiles (****e****, top) and height distributions (****e****, bottom) of a receiver device coated with a 100 nm-thick* $SiO_2$ *film.* ***g-i****, AFM topography images (****g****,* ***i****), line profiles (****h****, top) and height distributions (****h****, bottom) of a receiver device coated with a 3 μm-thick* $SiO_2$ *film.* ***j****, Summary of the average RMS surface roughness and the corresponding threshold height (see text) for receiver devices with coatings of various thickness; figure adapted from [45].*

estimate of the gap size at contact (minimum gap) and is found to be dependent on film thickness.

For the 100 nm-thick films the average is ~11 nm, and for the 3 μm-thick films it is ~21 nm.

**Cleanliness:** The cleanliness of the emitter and receiver surfaces is important to the nanoscale NFRHT measurement as the existence of particulate contaminations can easily limit the minimum effective gap size to be about the size of the largest particles. The cleanliness of the receiver surfaces was monitored during and after fabrication using dark-field optical microscopy (DFOM), AFM and CLSM. From this characterization we were able to identify receiver devices free of any particulate contamination larger than 10 nm in size. As to the spheres, Fig. 3.3a and Fig. 3.6b show how CLSM and AFM were used in effectively identifying spheres free of detectable particulate contaminations.

### 3.2.5. Experimental Procedure

**Alignment of the Emitter and Receiver:** In order to conduct a NFRHT measurement between the sphere emitter and the planar receiver, the two microdevices have to be first aligned properly with respect to each other (Fig. 3.1a). This is achieved using the custom-built nanopositioner in which both devices are mounted and controlled. The emitter device is mounted with the sphere facing upward, while the receiver device is suspended above the emitter with the desired $Au/SiO_2$ film facing downward towards the sphere. The xy-micropositioner enables fine lateral displacement of the emitter device relative to the receiver device. In the z direction, the gap between the emitter and the receiver is controlled by a micropositioner together with a nanometre-precise piezoelectric actuator (piezoactuator).

To ensure the creation of stable, nanometre-sized gaps, the nanopositioner is designed to be very stiff and is located on a vibration isolation table during experiments to minimize any mechanical disturbances from the laboratory environment. Further, we use only an ion pump during the experiments so as to eliminate any pump-related vibrations. Effects of acoustic noise are largely

attenuated once the nanopositioner is in a high vacuum. We note that the ambient ground vibration levels in our laboratory confirm to the VC-D criterion, whereas the acoustic noise confirms to the RC-30 criterion. Given the high stiffness of our emitter and receiver devices and the low level of ambient vibrations the root mean square displacement of the devices due to thermal and acoustic perturbations is smaller than 1 nm. Further, to attenuate thermal drift, active temperature control using thermoelectric Peltier devices was implemented, in addition to passive measures such as radiation and convection shields. Ultimately, the variation in temperature during the entire period of measurement (~10 hours, a period over which approximately 10 gap-dependent conductance curves were obtained for each film thickness, i.e. each conductance curve took about 1 hour to acquire) was attenuated to levels in the ~10 mK range. The effect on the vacuum gap due to temperature drift was characterized to be negligible (few nm/hour). The uncertainty in gap-size due to temperature drift was estimated to be <1 nm for gaps as large as 300 nm. The uncertainty due to temperature drift for larger gaps (300 nm – 10 microns) is slightly larger (~2 nm) but is also negligible.

**Measurement of Radiative Heat Transfer:** Measurement of radiative heat transfer (Fig. 1a, and Fig. 3.7, purple blocks) requires the ability to establish and quantify a temperature difference between the emitter and the receiver. This is achieved by supplying a sinusoidal electric current to the Pt resistance heater-thermometer on the emitter device, $R_{Pt,emit}$, where $f$ is the frequency in Hz and $I_0$ is the peak amplitude. The Joule heating caused by this current has a $2f$ component with an amplitude $Q_{Joule,2f}$ given by $Q_{Joule,2f} = \frac{1}{2} I_0^2 R_{Pt,emit}$. This sinusoidal heating generates a modulated temperature component in the suspended region at the same frequency, the amplitude of which is

given by $\Delta T_{emit,2f} = \frac{Q_{Joule,2f}}{G_{emit}}$ . In all our NFRHT measurements, a frequency of $f$ = 1 Hz was used and $I_0$ was chosen to generate a $\Delta T_{emit,2f}$ of ~10 K. Note that the radiation heat loss to the receiver is negligible compared to the heat conduction through the beams so the NFRHT has no noticeable effect on the desired $\Delta T_{emit,2f}$. Modulated rather than constant heating is chosen so a lock-in technique can be used to reduce the bandwidth and hence the noise.

The temperature-modulation of the emitter (at *2f*) results in a radiative heat flow $Q_{rad,2f}$ across the vacuum gap from the emitter to the receiver, which results in temperature modulations $\Delta T_{rec,2f}$ of the receiver at the same frequency. These temperature oscillations are measured by supplying a DC current across the Pt resistance thermometer of the receiver device and by monitoring the voltage component at *2f* ($V_{2f}$) in a measurement bandwidth of 5 mHz. Specifically, the temperature oscillations are related to the voltage oscillations by $\Delta T_{rec,2f} = \frac{V_{2f}}{\alpha I_{DC} R_{Pt,rec}}$ , where $R_{Pt}$ is the resistance of the Pt resistance thermometer and $I_{DC}$ is the magnitude of the applied DC current [35]. The radiative heat flow from the emitter to the receiver equals the heat flow from the suspended receiver to the ambient via the beams, i.e., $Q_{rec,2f} = \Delta T_{rec,2f} \times G_{rec}$. When the frequency response of the receiver is flat in the neighborhood of *2f* this equation can be readily used; at higher frequencies one needs to account for the attenuation in the temperature response due to the first-order response characteristics of the device; however, this can be done in a straightforward fashion due to the known frequency-response characteristics of all devices. Further, the radiative thermal conductance across the vacuum gap is given by $G_{rad} = \frac{Q_{rad,2f}}{\Delta T_{emit,2f} - \Delta T_{rec,2f}}$. Note that the total thermal conductance as measured is the sum of both far-field

and near-field contributions. A basic model involving gap-dependent view factors is needed for the far-field contribution to separate the two, and is discussed in 3.3 below.

**Control and Measurement of Gap Size:** Once the microdevices are aligned, the vacuum gap is controlled (Fig. 3.7, gray blocks) by displacing the emitter towards the receiver with the piezoactuator. The exact displacement is measured via built-in strain gauge sensors (SGS). A Wheatstone bridge configuration is used to enable sensitive resistance measurement. The excitation voltage features a relatively small amplitude (500 mV) and high frequency ($f_b$ = 5 kHz). The small amplitude minimizes Joule heating in the SGS mounted on the piezoactuator, while the high frequency ensures a low measurement noise floor. The modulated voltage across the Wheatstone bridge is pre-amplified before it is fed to a lock-in amplifier. In order to eliminate the effect of hysteresis and creep of the piezoactuator, a PID controller (Stanford Research Systems, SIM 960) is used to put the piezoactuator under feedback control. During the NFRHT experiment, the piezoactuator steps upwards in steps as small as ~2.5 nm.

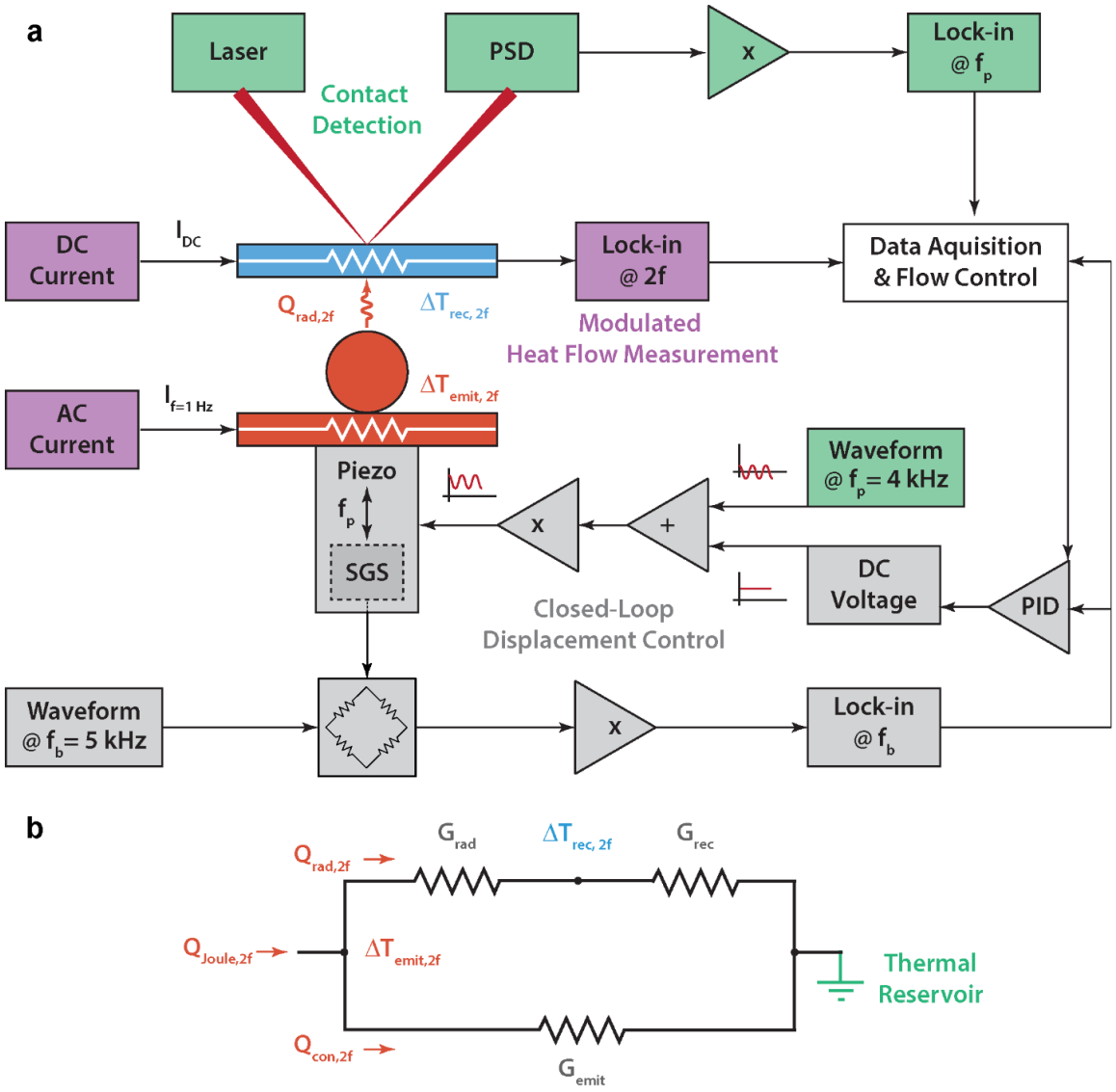


***Figure 3.7. Experimental procedure and principles.*** ***a****, Block diagram illustrating the experimental setup. The gray blocks represent the closed-loop displacement control, the green blocks show the optical detection scheme and the purple blocks denote the temperature measurement scheme. Specifically, we show how the piezoelectric displacement is measured using the strain gauge sensors and how contact is detected optically. We also show how the emitter device is heated and how temperature oscillations of the receiver device are detected. In the above block diagram X inside a triangle represents an amplifier and + inside a triangle denotes a summer.* ***b****, Thermal network showing the key quantities and relations characterizing the thermal measurements; figure adapted from [45].*

In order to quantify the size of the vacuum gap between the emitter and the receiver at various stages of the measurement, a reference position with a known gap size is needed apart from knowing the displacement of the emitter. This reference position is chosen to be the point where the emitter just makes contact with the receiver. High-resolution detection of the contact position is enabled by a laser optics system (Fig. 3.7, green blocks) similar to that used in many modern atomic force microscopes. A low power (nominally ~0.1 mW, not accounting for various losses, negligible heating effect) laser beam (635 nm) is focused onto the back side of the receiver device, and the reflected beam is collected with a position-sensitive photodiode (PSD). When the emitter and the receiver are separated, the path of the laser beam remains the same and a noisy but steady signal from the PSD is observed. However, when the emitter makes contact with and displaces the receiver, the reflected beam position on the PSD changes, leading to a sudden change of signal. In order to increase the sensitivity of contact detection, the piezoactuator is modulated by a small amplitude (~3 nm) at a relatively high frequency ($f_p$ = 4 kHz) so when the two devices make contact, the position of the emitter device and the PSD signal is modulated at the same frequency. By monitoring the amplitude of the PSD signal component at the modulation frequency, even a very small (~1-2 nm) displacement of the receiver can be identified enabling easy and accurate detection of contact formation.

This jump in lock-in output due to contact can be seen in Fig. 3.8a. Note that as the emitter approaches the receiver, there is a point where the emitter is close enough to the receiver to cause "snap-in" due to residual electrostatic charges. This is reduced to very small values due to the large stiffness of our devices and due to the incorporation of grounding loops and was experimentally quantified to be <5 nm. Finally, note that in all experiments a two-stage temperature controller

was employed that minimized temperature drift of the nanopositioner to ~1 mK over the period of the experiment and attenuated the effects of temperature drift to negligible levels.

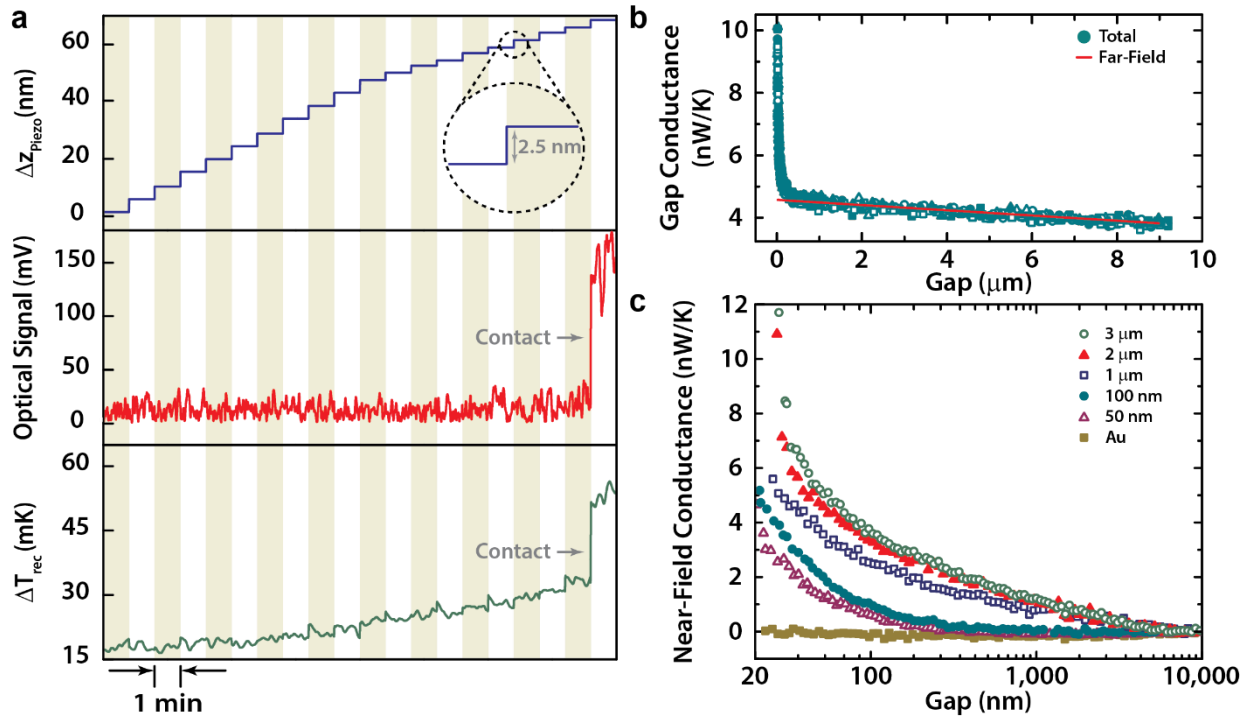


***Figure 3.8. Gap dependent near-field thermal conductance of thin films. a*** *Simultaneous recording of the displacement of the emitter towards the receiver (top), optical contact signal (middle) and temperature increase in the receiver (bottom) During the final approach piezo displacement steps of ~2.5 nm were used.* ***b*** *Contribution of far-field radiation to the radiative thermal conductance across the gap for a representative film (100 nm). The solid red line describes the predicted far field radiation which increases weakly (<1 nW/K) with decreasing gap size due to the associated change in view factor. As expected the measured data (green symbols) agree well with the prediction for gaps from 1 – 10 μm.* ***c*** *Near-field thermal conductance as a function of film thicknesses. Data for each film thickness represent an average of ~10 different data sets. Standard deviations are small and not shown for visual clarity; figure adapted from [45].*

**Comparison with previous experimental set-ups:** This experimental technique makes several significant improvements for NFRHT measurements over the previously used bimaterial cantilever-based approaches [24, 26] originally introduced by Narayanaswamy et al. [61] for NFRHT studies. Specifically, the deflection of the bimaterial cantilever is affected by both

temperature changes and mechanical forces posing challenges to the interpretation of experiments as described in a recent work [62]. In contrast, in the technique presented here, mechanical motion (detected optically) does not affect temperature measurements that are performed independently with a resistance thermometer. Moreover, in this system we are able to modulate the temperature of the emitter and thus employ lock-in based techniques that substantially enhance [34] the heat flow resolution to below 100 pW. Finally, this technique directly measures the far-field radiative heat flux, which cannot be measured using bimaterial cantilever-based techniques.

### 3.2.6 Experimental Results and their Interpretation

We began measurements with receivers coated with 3 μm-thick layers of $SiO_2$, which we expected to behave similar to bulk devices given the comparatively large thickness. After aligning a receiver and emitter at a gap size of ~10 μm in the nanopositioning platform (Fig. 3.1e) the nanopositioner was moved into a vacuum chamber and the emitter temperature ($\Delta T_{emit}$) was modulated sinusoidally at 2 Hz with a 10 K amplitude. The resulting radiative heat currents are quantified by measuring the temperature oscillations of the receiver ($\Delta T_{rec}$) using the integrated resistance thermometer, as explained is section 3.2.5. To measure the gap dependence of the heat transfer the emitter was displaced towards the receiver with the piezoelectric actuator and the gap-size was measured using the optical scheme. The top panel of Fig. 3.8a shows the displacement of the emitter towards the receiver, which starts with coarser steps (~5 nm) and continues in finer steps (~2.5 nm) close to contact. As expected, throughout the approach the optical signal (middle panel) does not change until contact is established. Finally, the bottom panel depicts the $\Delta T_{rec}$, which increases monotonically until contact is made. Contact is heralded by a sudden change in the

optical deflection signal, which occurs concurrently (i.e. within the same 2.5 nm displacement step) with a large jump in $\Delta T_{rec}$ due to conduction of heat from the silica sphere to the receiver.

These experimental data allow us to determine the gap-dependent, radiative thermal conductance as $G_{rad} = \frac{Q_{rad,2f}}{\Delta T_{emit,2f} - \Delta T_{rec,2f}}$ (see section 3.2.5). We obtain the near-field thermal conductance ($G_{NF}$) at each gap by subtracting the gap-dependent far-field contribution, which is estimated from the thermal conductance at the largest measured gap sizes (~10 μm) and the calculated gap-dependent view factor (Fig. 3.8b and section 3.3). The estimated $G_{NF}$ for the 3 μm-thick layer of $SiO_2$ as a function of the gap size is shown in Fig. 3.8c (open circles). Clearly, $G_{NF}$ increases rapidly from ~0 - 12 nW/K as the gap size is reduced to ~20 nm.

To investigate the effect of film thickness on NFRHT we employed receivers coated with a 100 nm-thick $SiO_2$ layer and measured $G_{NF}$ (Fig. 3.8c, solid circles). Intriguingly, the thermal conductance for these devices remains largely unchanged when the gap is reduced to well below 1 μm, and only begins to increase noticeably with gaps below 300 nm. When the gap size approaches the film thickness, $G_{NF}$ increases rapidly and becomes comparable to that obtained for 3 μm-thick $SiO_2$ films at gaps less than 100 nm. To better understand the dependence of $G_{NF}$ on the $SiO_2$ thickness we performed additional experiments with 50 nm, 1 μm and 2 μm-thick layers (Fig. 3.8c, all data points represent an average of ~10 independent measurements). It is clear from these experiments that $G_{NF}$ for each device depends on the thickness of the coating and begins to increase rapidly only when the gap size becomes comparable to the film thickness. We also performed a control experiment where the receiver had only a 100 nm-thick Au film and no $SiO_2$ coating. The results of this experiment (solid squares in Fig. 3.8c) show that there is no measurable increase in $G_{NF}$ as the gap size is decreased. Taken together, these observations suggest that surface

phonon polaritons on the $SiO_2$ surfaces are responsible for the observed, gap-dependent $G_{NF}$ behavior. However, before presenting a more detailed theoretical analysis of these results, we demonstrate the data analysis done and the repeatability of our experiments.

## 3.3 Data Analysis

### 3.3.1. Total Radiative Heat Transfer

To clarify the data analysis procedure and illustrate the repeatability of our experiments, we present several primary data sets. Fig. 3.9a shows for a receiver device coated with 100 nm-thick $SiO_2$ film, the measured $\Delta T_{rec,2f}$ (top, left y-axis), the corresponding radiative heat flow $Q_{rad,2f}$ (top, right y-axis) as well as the total thermal conductance $G_{rad}$ (bottom) as a function of the gap size. In these plots the symbols represent the mean values and the error bars are defined by the standard deviations. Similar results for a 3 μm-thick $SiO_2$ film measurement are shown in Fig. 3.9b. Note, while the emitter and the receiver do make physical contact during the experiment, the minimum gap, as shown in these plots, is not zero. We approximate the effective gap size at contact based on systemic measurements of the roughness of the surfaces (which varies from device to device as described in section 3.2.4), the step size of the piezoactuator (~2.5 nm), the modulation amplitude of the piezoactuator (~4 nm) and the possible snap-in distance (<5 nm). Together these uncertainties result in estimates of the effective minimum gap size with respect to NFRHT (Fig. 3.9c) that range from 18 nm to 28 nm for receiver devices with different $SiO_2$ coating thickness. The uncertainty of the measured gap size is ~6 nm which is mainly due to the piezoactuator modulation amplitude, the displacement measurement noise and the sensitivity of contact detection. Thermal drift is negligible especially for small gaps due to the use of contact position as the reference.

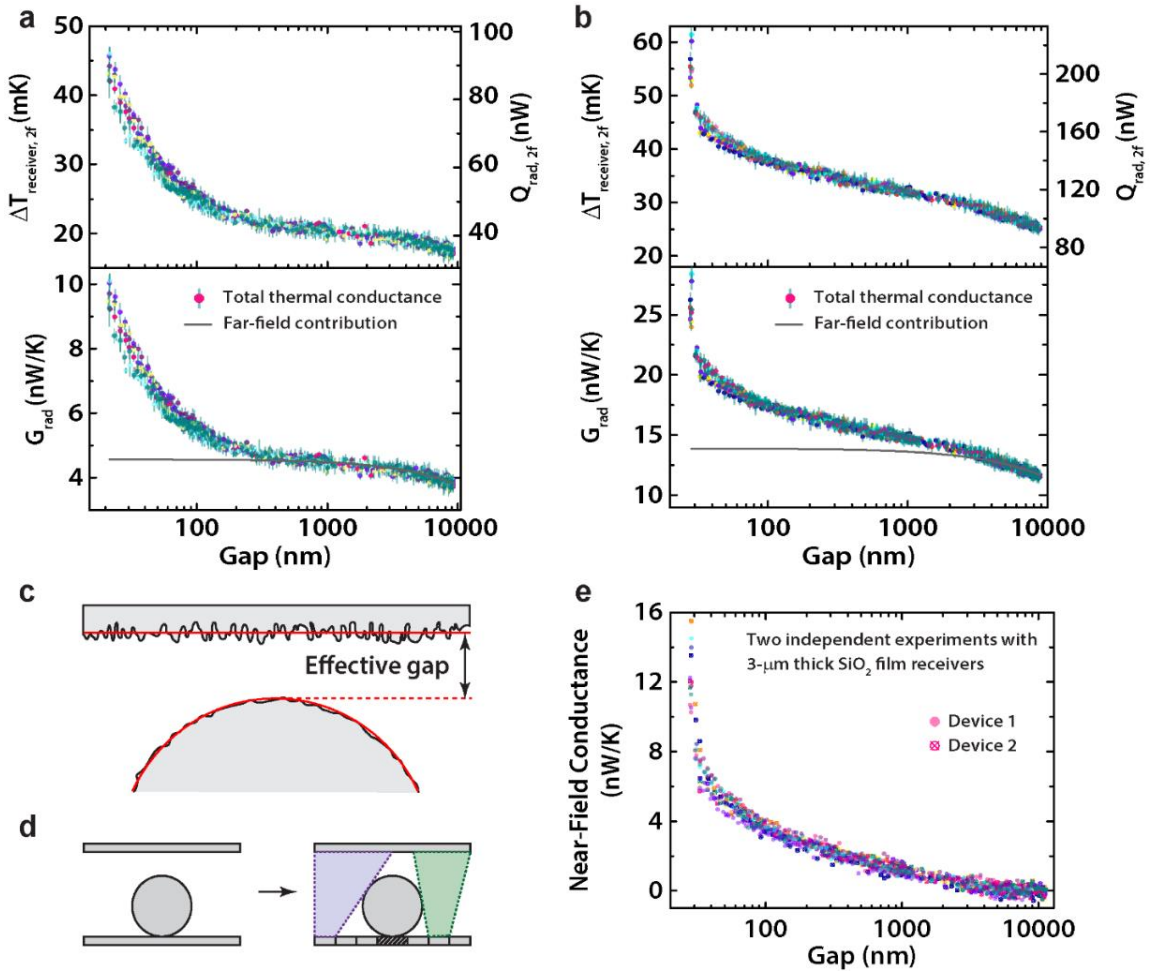


***Figure 3.9. Data analysis and representative raw data. a****, Shows the temperature rise ($\Delta T_{rec,2f}$) of the receiver and corresponding heat currents ($Q_{rad,\,2f}$) in six consecutive experiments performed using a receiver device with a 100 nm-thick $SiO_2$ coating. The lower panel of* ***a*** *shows the total thermal conductance of the vacuum gap and the estimated far-field contribution, both as a function of the gap size. The error bars denote the standard deviation.* ***b****, Same as* ***a,*** *but for a 3 μm-thick $SiO_2$ coating on the receiver (data obtained from nine consecutive measurements).* ***c****, Schematic illustrating the concept of an effective gap size.* ***d****, Schematic showing how the view factor from the emitter to the receiver device is calculated by dividing the emitter device into multiple parts for which analytical expressions of the view factors can be obtained.* ***e****. Shows the measured near-field thermal conductance, from a total of fifteen sets of data points, obtained from experiments performed using two different receiver devices each coated with a 3 μm-thick $SiO_2$ film (9 from the first device and six from the second device). Note that only the near-field thermal conductance is shown; figure adapted from [45].*

### 3.3.2. Estimation of Near-Field Thermal Conductance

To determine (calculate) the far-field contribution to the total radiative heat transfer, we perform an analysis of the view factor from the emitter device to the receiver device as a function of the gap size. As shown in Fig. 3.9d, the approach we took was to first divide the total view factor into contributions from the sphere and the underlying plate. The view factor between a sphere and a concentric rectangle as well as that between two parallel rectangles of arbitrary dimensions can be obtained analytically [63]. However, the entire emitter plate does not "see" the receiver as it is partially blocked by the sphere. To overcome this issue, the emitter plate is sliced into numerous parallel narrow bands and the view factor from each band to the rectangular area it sees on the receiver is calculated [64]. In the end, contributions from all parts are added together following the summation rule, providing accurate view factors for different gap sizes. Subsequently, the contribution from far-field radiation at various gaps is estimated from knowledge of the view factors and the thermal conductance at very large gaps (~10 μm), where near-field contributions are negligible (Fig. 3.10). As seen in Fig. 3.9a-b, the predictions (solid line) agree very well with the experiments and suggest that the thermal conductance increase for micrometre-sized gaps is mostly from small increases in the far-field contribution. With the total thermal conductance as well as the far-field contribution known for various gaps, the near-field thermal conductance is calculated simply as the difference between the two. In Fig. 3.9e, we show 15 sets of data from experiments performed using two different receiver devices coated with 3 μm-thick $SiO_2$ films. It can be seen that the data overlay so closely on each other that results from any two individual measurements cannot be visually distinguished. This highlights the repeatability both between individual measurements and across devices.

## 3.4 Theory and Modeling

Next, we evaluated if our experimental findings of NFRHT in thin films are in (quantitative) agreement with theoretical predictions.

### 3.4.1 Theoretical Description of the Radiative Heat Transfer

The theoretical analysis of radiative heat transfer in our multilayer system was carried out within the framework of Rytov's fluctuational electrodynamics (FE) [12, 37, 62]. Our calculation of the radiative heat transfer between the spherical emitter and the thin film-coated receiver proceeds in two steps: First, we determine the heat transfer between a semi-infinite $SiO_2$ surface and a $SiO_2$ thin film located on a semi-infinite Au surface, see Fig. 3.10a. We denote the distance separating either subsystems (or gap size) by *d* and the coating thickness by *t*. Moreover, we consider the silica surface to be at temperature $T_1$, while the silica coating and the Au surface are at temperature $T_3$. The solution of Maxwell's equations in the framework of the FE theory is obtained with the help of a scattering matrix approach [9], which is particularly well suited for multilayer systems. Specifically, the following expression is used for computing the heat flux (heat transfer per unit time and per unit area) [11]

$$Q(T_1, T_3, d) = \int_0^\infty \frac{d\omega}{4\pi^2} [\Theta(\omega, T_1) - \Theta(\omega, T_3)] \int_0^\infty dk k [\tau_s(\omega, k) + \tau_p(\omega, k)] \quad (1)$$

where $\Theta(\omega, T_i) \equiv \hbar\omega / [\exp(\hbar\omega / k_B T_i) - 1]$ , $T_i$ is the absolute temperature of the layer *i*, $\omega$ is the radiation frequency, *k* is the magnitude of the wave vector component parallel to the layer planes, and $\tau_s$ and $\tau_p$ are the transmission probabilities for the transverse electric (TE) and transverse

magnetic (TM) modes, respectively. These probabilities can be expressed in terms of the Fresnel coefficients of the different layer interfaces as follows:

$$\tau_{\alpha=s,p}^{13}(\omega,k)=\begin{cases}\frac{(1-|R_\alpha^1|^2)(1-|R_\alpha^3|^2)}{|D_\alpha|^2}, & if\ k<\frac{\omega}{c}, propogating\ waves\\ \frac{4Im(R_\alpha^1)Im(R_\alpha^3)e^{-2Im(\zeta_3)d}}{|D_\alpha|^2}, & if\ k>\frac{\omega}{c}, evanescent\ waves\end{cases}, (2)$$

Where $R_\alpha=\frac{r_\alpha^{23}+r_\alpha^{34}e^{2iq_3t}}{1-r_\alpha^{34}r_\alpha^{32}e^{2iq_3t}}$ and $D_\alpha=1-r_\alpha^{21}R_\alpha e^{2iq_2t}$. Here, the different Fresnel coefficients are given by $r_p^{ij}=\frac{\varepsilon_j q_i-\varepsilon_i q_j}{\varepsilon_j q_i+\varepsilon_i q_j}$ and $r_s^{ij}=\frac{q_i-q_j}{q_i+q_j}$ where $q_i=\sqrt{\varepsilon_i\omega^2/c^2-k^2}$ is the transverse component of the wave vector in layer *i* and $\varepsilon_i$ is the corresponding dielectric constant. The indices *i* and *j* run from 1 to 4 following the labelling defined in Fig. 3.10a. The dielectric constant of $SiO_2$ was taken from Palik [65], and that for Au was obtained from Ordal et al. [66]. These dielectric functions are shown in Fig. 3.10c-d in the energy range of interest for the heat transfer at room temperature. Since the temperature difference between the silica sphere and the thin film was only 10 K, we restrict our analysis to the linear response regime. We explicitly checked the validity of this approximation and found that it deviates from the exact result by less than 1% for the whole range of parameters. Thus, we focus on the radiative linear heat conductance per unit area (*h*), the heat transfer coefficient, which is given by

$$h(T,d)=\lim_{(T_1-T_3)\to 0}\left|\frac{Q(T_1,T_3,d)}{T_1-T_3}\right|=\int_0^\infty\frac{d\omega}{4\pi^2}\frac{\partial}{\partial T}\left[\frac{\hbar\omega}{e^{\hbar\omega/k_BT}-1}\right]\int_0^\infty dkk\left[\tau_s(\omega,k)+\tau_p(\omega,k)\right], (3)$$

For all calculations shown here we assumed an absolute temperature of $T$ = 300 K. The computed gap dependence of *h* for this structure is shown in Fig. 3.10e for different coating thicknesses.

In a second step, in order to establish a direct comparison with our experimental measurements, we use the results obtained for the semi-infinite multilayer system to compute the thermal conductance *G(T, d)*, between a 53 μm diameter silica sphere and a thin film-coated surface by making use of the so-called Derjaguin approximation [67]. As illustrated in Fig. 3.10b, in this approximation the sphere is thought to be sliced into a series of infinitesimal annuli of different radii and the conductance between every annulus and the thin film (or thin film-coated receiver) is computed using equations (1-3). Thus, the thermal conductance is computed as

$$G(T,d) = \int_0^R 2\pi r h(T, \bar{d}(r)) dr, \quad (4)$$

where *R* is the radius of the sphere, *h* is the linear conductance of the multilayer system defined in equation (3), and $\bar{d}(r) = d + R - \sqrt{R^2 - r^2}$ is the local distance between the silica film and the annuli, see Fig. 3.10b. The validity of this approximation has been thoroughly investigated in the literature and it has been shown to provide accurate results for the NFRHT in the regime where the gap size is much smaller than the radius of the silica sphere [40]. The results obtained within this approximation for the thermal conductance between the sphere and coated film as a function of the gap size and for different coating thicknesses are shown in Fig. 3.10f. We emphasize that in this figure we only show the near-field contributions, which are obtained by subtracting the far-field contributions (gap size = 70 μm) from the total heat conductance of equation (4).

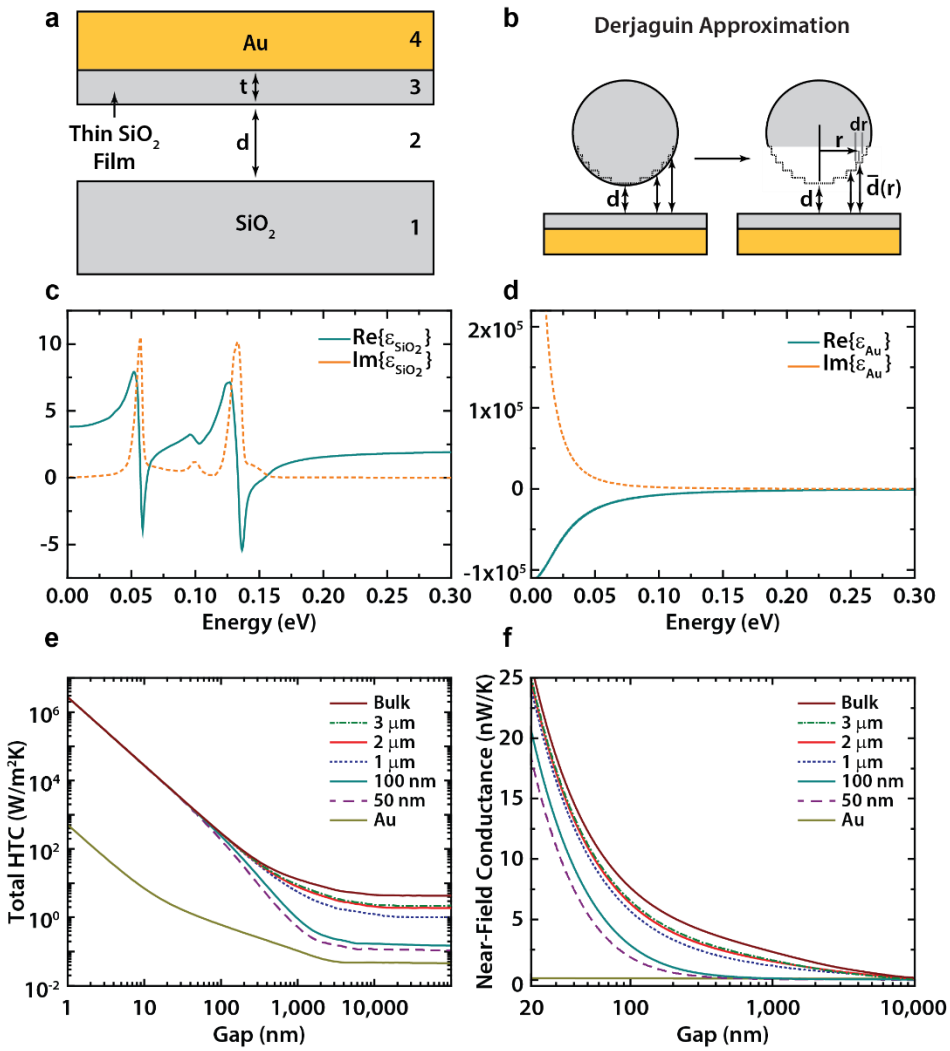


***Figure 3.10. Multilayer system, Derjaguin approximation and dielectric constants. a****, Multilayer system used to (theoretically) predict the radiative heat transfer in our experimental system. Here, a semi-infinite silica surface (medium 1) is separated by a vacuum gap (medium 2) of size d from a silica film of thickness t (medium 3) coating a semi-infinite Au surface (medium 4).* ***b****, Illustrates how we used the Derjaguin approximation [67] as described in equation (4), in conjunction with data shown in* ***a,*** *to estimate NFRHT between a silica sphere and a silica-coated Au surface.* ***c****, Real and imaginary parts of complex dielectric constant of silica as a function of energy. Notice that the real part becomes negative in two narrow regions due to the existence of phonon polaritons in this dielectric material. This is the origin of the appearance of surface phonon polaritons in our multilayer structure, which dominate the near-field radiative heat transfer.* ***d****, The same as in panel* ***c*** *for gold.* ***e,*** *Computed linear thermal conductance per unit of area as a function of the gap size for the multilayer system shown in the inset. This structure comprises a semi-infinite silica layer separated by a vacuum gap of size d from a silica thin film coating a semi-infinite Au surface. The different curves correspond to different thicknesses of the silica coating.* ***f,*** *Calculated heat transfer coefficient as a function of the gap size for the sphere-coated layer*

*system shown in the inset. The different curves correspond to different values of the coating thickness. The far-field contribution is subtracted to make a direct comparison with our experiments. In both panels a temperature of 300 K was assumed; figure adapted from [45].*

In our experimental system, the receiver consists of a silica thin film deposited on a 100 nm-thick gold film, which in turn lies on top of a silicon nitride ($SiN_x$) membrane. However, in the multilayer system used to compute *h* (Fig. 3.10a) we assumed that the Au layer is semi-infinite. This assumption is well justified since a 100 nm-thick Au layer is optically thick at the relevant frequencies and the $SiN_x$ membrane underneath plays no role in the heat transfer in our experiments. To demonstrate this fact, we extended the above theory to consider a geometry with a finite thickness Au layer (100 nm) resting on a semi-infinite layer of $SiN_x$. This extension only requires generalizing the expression of the coefficients $R_\alpha$ in equation (2) to take into account the additional $SiN_x$ layer, which is a straightforward calculation within the scattering matrix formalism [68]. Using the dielectric constant of $SiN_x$ reported elsewhere [69], we computed *h* in the multilayer system with the $SiN_x$ membrane and compared it to the results without this membrane. We found that, irrespective of the gap size or the coating thickness, the $SiN_x$ layer plays no role in the heat transfer in our system and therefore we assume throughout this work that the Au layer behaves like a semi-infinite layer.

### 3.4.2. Validity of the Derjaguin Approximation and Role of the Film Roughness

The validity of the Derjaguin approximation has been investigated in the past. For instance, Sasihithlu and Narayanaswamy studied this issue [70] in the context of the heat transfer between two silica microspheres. These authors concluded that the Derjaguin approximation does provide excellent results when the far-field contribution is systematically accounted for using classical radiative heat transfer theories as done in this work (see Section 3.3). Further analysis on the

validity of the Derjaguin approximation was performed by Otey and Fan for the case of a silica sphere and a silica infinite plate [40], which is a closer approximation to our system than the work by Sasihitulu et al. These authors showed that the Derjaguin approximation provides a very accurate description of the NFRHT when the sphere radius is much larger than the gap size (with relative errors within 1%). This is precisely the scenario in our work as the diameter of our sphere is 53 μm and the gap-size of interest for near-field effects is in the 20 nm – few μm range. Therefore, the use of Derjaguin approximation in our work is well justified.

**Direct demonstration of the validity of the Derjaguin approximation:** In order to further bolster these conclusions and directly test the validity of the Derjaguin approximation, we have performed our own numerical calculations of heat transfer between a silica sphere and a silica plate. For this purpose, we have employed the fluctuating-surface-current (FSC) formulation of the heat transfer problem that has been recently put forward by Rodriguez and coworkers [71]. As shown by these authors, this formulation can be combined with the boundary element method (BEM), a well-established numerical method in classical electromagnetism, to describe the heat transfer between bodies of arbitrary shape. It is worth stressing that this approach provides numerically exact results for the heat transfer within the framework of fluctuational electrodynamics. In practice, this formulation of the heat transfer problem has been implemented in the SCUFF-EM29 solver. This code makes use of the BEM to discretize the surfaces of the bodies into polygonal elements or panels and the surface currents in each element are described by piecewise low-degree polynomials. In particular, SCUFF-EM employs a so-called RWG30 basis of vector-valued polynomial functions defined on a mesh of triangular panels. This basis is

suitable to deal with arbitrary geometries and yields results that converge with increasing resolution (smaller triangles). Further technical details can be found in [71, 72].

In our calculation we analyzed a scenario with a silica sphere (diameter 20 μm) and a silica disk (diameter 18.8 μm) as shown in Fig. 3.11a. The choice of the slightly small size of the sphere and disk keeps the problem computationally tractable (computational resources scale polynomially with size of the system) and enables validation of the Derjaguin approximation for systems with sphere and gap-sizes comparable to those employed in our experiments. We have chosen a disk instead of a rectangle to avoid the singularities in the electromagnetic fields associated with the sharp corners of a rectangle. This choice facilitates computational convergence and is reasonable because the near-field heat flow is dominated by a small region at the center of the disk. In Fig. 3.11c we present a comparison of the exact results (red filled circles) of total thermal conductance (which exactly capture the near-field and far-field contributions) to that obtained using the Derjaguin approximation (see section 3.4.1) which includes only the near-field contribution (black solid line). As one can see, the Derjaguin approximation is able to reproduce the exact results for a wide range of gap sizes, which nicely demonstrates the validity of this approximation in the context of our work. Notice that the only deviations between these two results occur at large gaps (of the order of 5-10 μm), which are simply due to the fact that the exact result contains a small far-field contribution that has not been subtracted here to avoid any post-processing of the exact data. In any case, notice that at large gaps the heat conductance is quite low and therefore, these small deviations are completely irrelevant for the conclusions of our work. Thus the analysis provided above in conjunction with past work unambiguously supports the use of the Derjaguin approximation for analyzing the experimental results of our work.

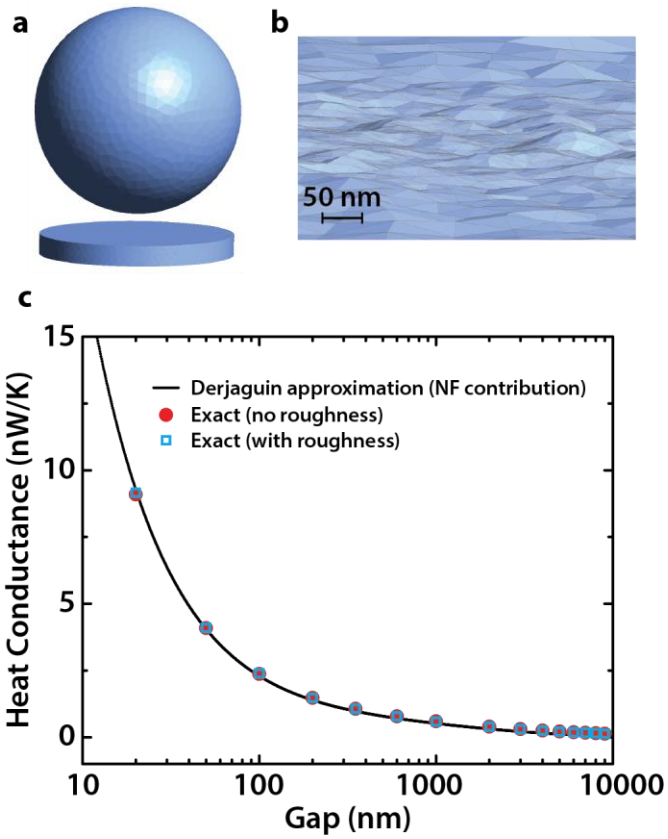


***Figure 3.11. Testing the Derjaguin approximation. a,*** *The sphere-finite plate used to study the validity of the Derjaguin approximation and the role of the film thickness. The silica sphere has a diameter of 20 μm, while the silica disk has a diameter of 18.8 μm and a thickness of 2 μm.* ***b,*** *Blow up of the receiver rough surface used to investigate the role of the film roughness.* ***c,*** *Calculated room temperature radiative heat conductance as a function of the distance between the sphere and the disk. The black solid curve corresponds to the Derjaguin approximation where only the near-field contribution has been taken into account. The red filled circles correspond to the exact numerical results for the total heat conductance for the system shown in* ***a*** *as obtained with the FSC method, while the blue open squares correspond to the exact numerical results for the case where the disk has a rough surface, as shown in panel b; figure adapted from [45].*

**Validity of Derjaguin approximation in the presence of surface roughness:** The use of the FSC formulation in combination the SCUFF-EM package also allows us to address another important issue. As explained in section 3.2.4, our $SiO_2$ films exhibit a surface roughness of ~10 nm. We performed analysis to evaluate if this roughness affects NFRHT and if the Derjaguin

approximation is still applicable to devices with rough films. Specifically, we investigated heat transfer in the sphere-disk system discussed above, where the disk is assumed to have a rough surface. To faithfully describe the experimental situation, we introduced random Gaussian noise in the profile of the disk surface with a maximum protrusion height of 18 nm and a correlation length between protrusions of 30 nm.

We show in Fig. 3.11b, a blow up of the surface of the disk for this example. In this case, the distance between the sphere and the rough surface is defined as shown in Fig. 3.8c, i.e. very much like in our experiments. The results for the total heat conductance as a function of the gap size are shown in Fig. 3.11c as blue open squares. The obtained conductances are identical to those obtained for those with a smooth disk, which clearly shows that the presence of the roughness in our coating films does not play any significant role for the range of gaps explored in our experiments (> 20 nm). The reason for this insensitivity to surface roughness is that the sphere radius is much larger than the scale of the roughness and thus, the sphere averages over a large portion of the rough surface. The net result is that the total heat transfer is only very slightly (<1 %) higher than in the ideal smooth case. In summary, our results unambiguously validate the use of the Derjaguin approximation to analyze NFRHT in our experiments.

## 3.5 Origin of the Thickness Dependence of the NFRHT: Surface Phonon Polaritons

Here we explain how the fundamental properties of the surface phonon polaritons (SPhPs) directly determine the observed dependence of the NFRHT on the thickness of the coating film. For this purpose we focus on the analysis of the heat transfer in the multilayer system shown in Fig. 3.10a.

The conclusions from this analysis can be readily extended to the sphere and thin film system in the spirit of the Derjaguin approximation.

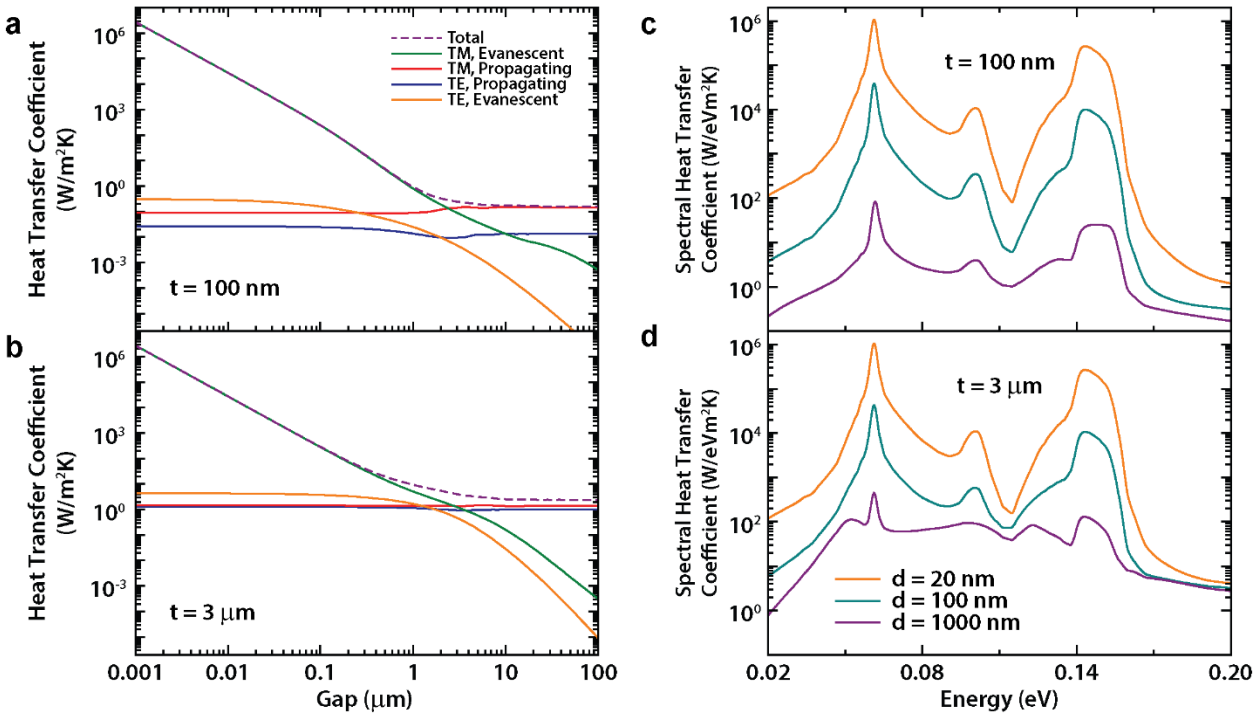


***Figure 3.12. Computed radiative heat conductance in the multilayer system. a-b****, Heat transfer coefficient for the multilayer system in Fig. 3.10a as a function of the gap size and for two different thicknesses of the silica coating, t. The solid lines correspond to the different contributions coming from the TE and TM modes, both evanescent and propagating, while the dashed line shows the total heat transfer coefficient. Notice that below 1 μm the contribution to the radiative heat transfer is dominated by evanescent TM modes that correspond to surface phonon polaritons.* ***c-d****, The corresponding spectral heat transfer coefficient as function of the radiation energy for several gap sizes and two different coating thicknesses. Notice that the main contribution to the conductance comes from the regions where the real part of the dielectric constant of silica becomes negative, see Fig. 3.10c, which is precisely where surface phonon polaritons exist; figure adapted from [45].*

An analysis of the contributions from different modes to NFRHT, for two different coating thicknesses (100 and 3000 nm), is presented in Fig. 3.12a and b. It is found that the heat transfer coefficient increases dramatically below 1 μm. Moreover, an examination of the individual contributions of the TM and TE modes for both propagating ($k \leq \omega/c$) and evanescent waves

($k > \omega/c$) reveals that in the near-field regime the heat transfer is completely dominated by evanescent TM-waves. This is a first indication that the NFHRT in our system is governed by the excitation of SPhPs [73].

Further evidence in support of this conclusion can be obtained from an analysis of the spectral heat transfer coefficient, $h_{\mathrm{spc}}(\omega)$, defined as

$$h \equiv \int_0^\infty h_{spc}(\omega) d\omega, \quad (5)$$

which gives the contribution of each frequency to the total heat transfer coefficient. In Fig. 3.12c and d we show the spectral heat transfer coefficient for several gaps in the near-field regime and two different coating thicknesses. Notice that heat transfer is dominated by contributions from two narrow frequency ranges that correspond to regions where the dielectric constant of $SiO_2$ has a negative real part, see Fig. 3.10c, which are precisely the regions where the SPhPs exist.

Having established that the evanescent TM-modes dominate the NFRHT, it is interesting to analyze their transmission. In Fig. 3.13a and b we show the dependence of transmission on *k* for $\hbar\omega = 61.2$ meV, which corresponds to the maximum of the spectral heat transfer coefficient (see Fig. 3.12c and d). To be precise, we show the transmission for two different coating thicknesses (100 and 3 μm) and multiple gap sizes. As can be seen, the transmission attains a maximum, equal to one, for values of *k* that increase as the gap size decreases, reaching very large values of *k* ($k > 100\omega/c$) for the smallest gaps. From equation (1) it is apparent that this dramatic increase in the value of *k* at which the transmission becomes unity is the reason for the large increase of the NFRHT at small gap sizes. Conversely, when the separation becomes comparable to the film thickness the transmission becomes <1 and decreases monotonically as the gap size is increased.

This behavior is apparent in the 100 nm-thick film data shown in Fig. 3.12a and c. To identify the waves that contribute most to heat transfer at various gap sizes we present in Fig. 3.13c and d transmission as a function of *kd*. This data illustrates that the transmission peaks at larger *k* values as the gap size is decreased. In fact, it can be seen that the *k* with largest transmission is inversely proportional to *d*. Hence, heat transfer is dominated by waves with larger *k* values as the gap size is decreased.

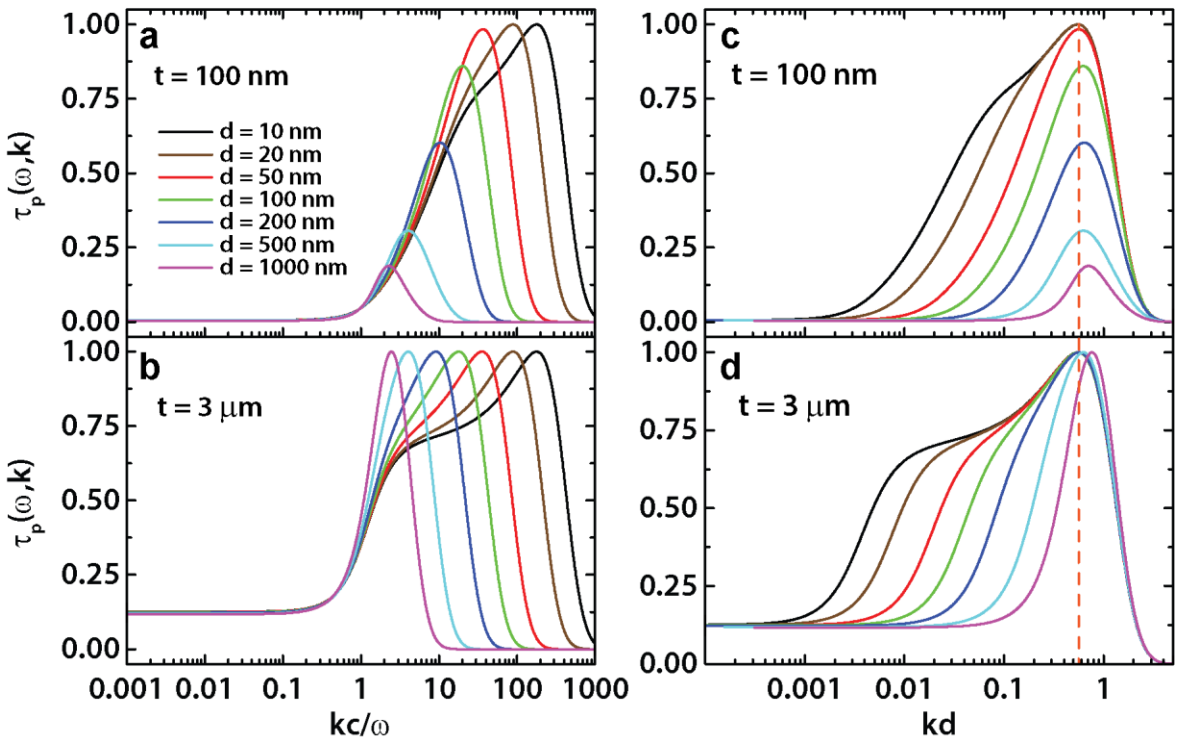


***Figure 3.13. Transmission probability of the TM modes. a-b**, Transmission probability of the TM waves as a function of the magnitude of the parallel component of the wave vector normalized by ω/c for different values of the gap and two different coating thicknesses. The radiation energy has been fixed here to $\hbar\omega = 61.2$ meV, which is the energy at which the spectral heat transfer coefficient reaches its maximum, see Fig. 3.12c and d. Notice, for small gaps the transmission reaches a maximum of 1 for values ($k \gg \omega/c$). **c-d**, The same as in panels **a-b** but shown as a function of the parallel wave vector multiplied by the gap, d. Notice that all the curves show a maximum roughly at the same value, a value that approximately corresponds to the wave vector of the CSPhP at this frequency as given by equation (7) and indicated by vertical dashed lines; figure adapted from [45].*

To establish unambiguously the connection between the NFRHT and the SPhPs in our system, we computed the dispersion relation for the cavity surface phonon polariton modes (CSPhPs) supported by the vacuum cavity between the silica layers. One can show that this dispersion relation is given by the solution of the following secular equation

$$D_p(\omega, k) = 1 - r_p^{21}(\omega, k) R_p(\omega, k) e^{2iq_2 d} = 0, \quad (6)$$

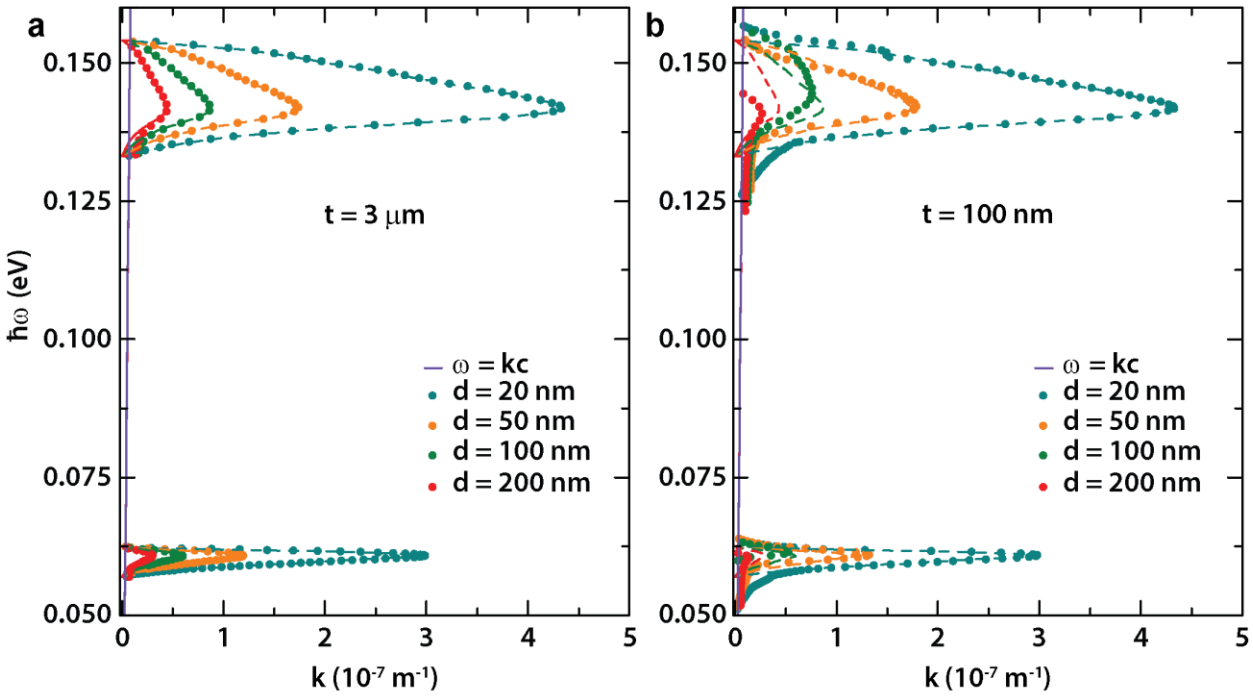


***Figure 3.14. Dispersion relation of the cavity surface phonon polaritons. a****, Dispersion relation of the surface phonon polaritons for t = 3000 nm and different gaps. The open symbols correspond to the results the exact numerical solution of equation (6), while the dashed lines correspond to the analytical result of equation (7). The light blue solid line corresponds to the light line. Notice that the analytical results match accurately the numerically computed ones.* ***b****, The same as in panel* ***a*** *but for a thickness t = 100 nm. Notice that the analytical result ceases to reproduce the exact results when the gap becomes comparable to the coating thickness; figure adapted from [45].*

Notice that $D_p$ is the denominator in the expression of $\tau_p$ in equation (2). In Fig. 3.14 we show the dispersion relations of the CSPhPs obtained from the numerical solution of equation (6) for two different coating thickness (3000 and 100 nm) and different gap sizes ranging from 20 nm to 200 nm. As one can see, the magnitude of the parallel wave vector of the CSPhPs increases as the gap size decreases and therefore, they progressively become more localized to the silica interfaces. In the limit of small gaps (smaller than the coating thickness), the dispersion relation can be obtained analytically. In this limit $R_p \approx r_p^{23}$, which allows us write the solution of equation (6) in the electrostatic limit ($|k| \gg \omega/c$) as

$$k_c = \frac{1}{d}\ln[\pm\frac{\varepsilon(\omega)-1}{\varepsilon(\omega)+1}], \quad (7)$$

where $k_C$ is the complex amplitude of the parallel wave vector of the surface mode ($k = \mathrm{Re}\{k_C\}$) and $\varepsilon(\omega)$ is the dielectric constant of $SiO_2$. Notice that there are two branches corresponding to an anti-symmetric (+) and a symmetric mode (–), but they are degenerate in the sense that both of them have the same real part of the wave vector. In Fig. 3.14 we show that this analytical result agrees very well the numerical solution of equation (6) in its range of validity ($d < t$). Additionally, as we show in Fig. 3.13c and d (see vertical dashed line), equation (7) reproduces the position of the transmission maxima.

This is further illustrated in Fig. 3.15 where we show that this dispersion relation describes very accurately the transmission maxima for the whole range of frequencies. Thus, there is overwhelming support for the conclusion that the CSPhPs are responsible for the NFRHT in our system.

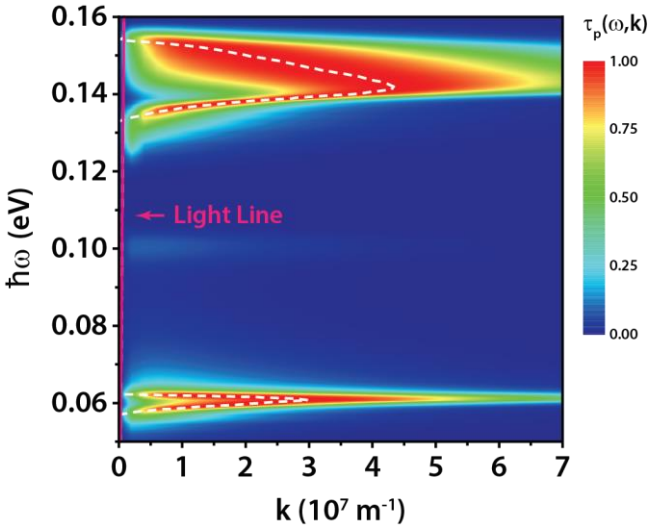


***Figure 3.15. The transmission probability for TM modes,*** $\tau_p(\omega,k)$ *, as a function of the radiation energy and the magnitude of the parallel wave vector for t = 100 nm and d = 20 nm. The white dashed line corresponds to the analytical dispersion relation of the cavity surface phonon polaritons, while the pink solid line next to the y-axis corresponds to the light line, i.e.* $\omega = kc$*. The maxima of the transmission appear largely to the right of the light line and therefore correspond to evanescent waves; figure adapted from [45].*

In light of the above discussion the thickness dependence of the NFRHT can be understood in terms of the penetration depth of the CSPhPs. Assuming that $|k| \gg \omega/c$ , this penetration depth at a given frequency, *l(ω)* , is approximately given by $l(\omega) \approx 1/[Re\{k_c(\omega)\}]$ , which in the limit of small gaps reduces to

$$l(\omega) \approx \frac{d}{2Re\{\ln\left[\frac{\varepsilon(\omega)-1}{\varepsilon(\omega)+1}\right]\}}, \quad (8)$$

The denominator in this expression is on the order of 1 for frequencies close to that of the maximum of the spectral heat transfer coefficient. Thus, for small gaps *l(ω)* is on the order of the gap size and is independent of the thickness of the dielectric coating. This result implies that for small gaps, only a shallow region of thickness *l* from the interface contributes to the NFRHT.

Therefore, the heat transfer is independent of the coating thickness (Fig. 3.10e) for all films with a thickness greater than the gap size.

This fact is illustrated in Fig. 3.16, where we compare the normalized electric field intensity of representative CSPhP modes, corresponding to an energy of ~61.2 meV, for two coating thicknesses (100 nm and 3 μm) and a gap of 20 nm. Notice that the mode shapes are almost identical due to the small penetration depths showing that NFRHT in small gaps occurs through identical modes for both thin and thick films and is hence unaffected by film thickness [74] or the presence of a gold layer. On the contrary, when the gap becomes comparable to or larger than the film thickness, the intensity of these modes decays slowly in $SiO_2$, but drops sharply at the $SiO_2$-Au interface (lower panel Fig. 3.15b), reducing their ability to contribute to heat transport and leading to a diminished transmission probability. Thus, the NFRHT enhancement for thin films, at gaps larger than the film thickness, is significantly smaller than that of thicker films at the same gap size. Finally, we observe that the large reduction in the NFRHT in the absence of a dielectric coating is mainly due to the mismatch between the spectral coefficients of $SiO_2$ and Au and is consistent with past work [24].

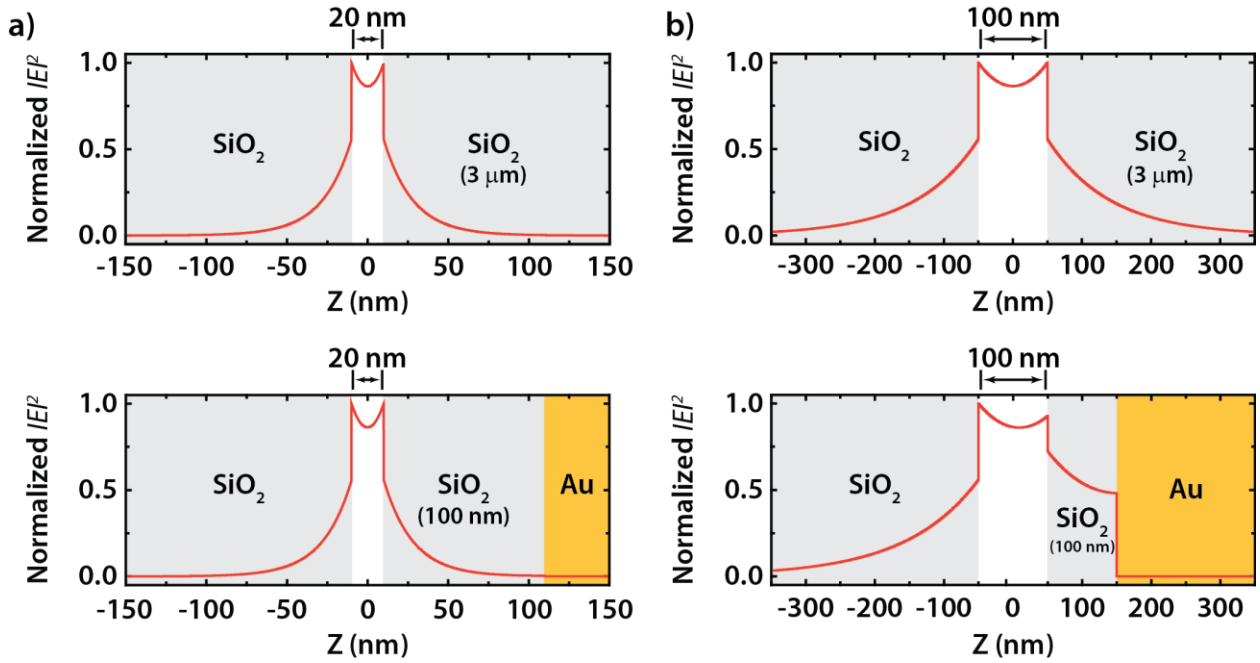


***Figure 3.16 Mode shape of CSPhPs. a****, Normalized electric field intensity of a representative CSPhP mode ($\hbar\omega = 61.2$ meV) for a gap of 20 nm and thicknesses of t = 3 μm (upper panel) and t = 100 nm (lower panel), normalized to peak intensity. The grey regions correspond to $SiO_2$ and the yellow region represents Au.* ***b,*** *Same as in a but for a gap of 100 nm; figure adapted from [45].*

The normalized electric field intensity shown in Fig. 3.16 was computed using a standard scattering matrix approach [68]. Briefly, the modeling begins by fixing the electric field amplitude for a mode (a pair of frequency and parallel wave vector related by the dispersion relation) of interest, at a location in the multilayer structure well inside the silica surface. Subsequently, the field amplitudes in other locations are calculated via the scattering matrix of the system considering multiple reflections at the interfaces.

## 3.6 Concluding Remarks

The experimental results and analysis presented here show for the first time that NFRHT can be dramatically affected by nanometer-thick dielectric films if the gap size is comparable to the film thickness. The instrumentation advances made in this work towards high resolution measurement of heat flows and precise control of gap size will enable experimental studies of a variety of nanoscale radiative heat transport phenomena that remain unexplored [75, 76]. Finally, the results reported here are of great importance to future nanotechnologies [2, 51, 77] that seek to take advantage of near-field effects for thermal management, lithography and thermo-photovoltaic applications.

**Contributions:** The devices were designed by B. Song and me and fabricated by S. Sadat and D.R. Thompson. The experiments were run by B. Song, A.R. Fiorino and me. The numerical simulations were done by V. Frnández-Hurtado, J. Feist, F. J. Garcia-Vidal, and J. C. Cuevas. For the plane-plane measurements, the devices were designed by B. Song and D.R. Thompson and fabricated by D.R. Thompson. I contributed to FEM simulations of devices. The experiments were run by B. Song. All of the above work was conceived by E. Meyhofer and P. Reddy.

# CHAPTER 4

# Summary and Outlook

## 4.1 Summary

In this dissertation, I have presented a new experimental platform for measurements of NFRHT enhancement between parallel plates and also from nanoscale-thin dielectric coatings. The two components of the platform were shown in chapter 2. The first component was a room-temperature picowatt resolution calorimeter [33] that was able to measure heat flows as low as ~4 pW. This calorimeter was designed and fabricated by my colleague S. Sadat and I collaborated with my colleagues Y-J. Chua and W. Lee in testing its performance. Despite the fact that this calorimeter achieved an order-of-magnitude improvement in heat-flow resolution over other room-temperature calorimeters (at the time), I explained how it was unsuitable for NFRHT measurements due to the thermos-mechanical coupling between its bimaterial temperature sensor and the active area of device, negatively influencing accurate control and measurement of spatial

separations. Consequently, Sadat [34] was able to fabricate a new version of resistive calorimeters that did not use a moving cantilever sensor and these new calorimeters were used for our NFRHT experiments. The 2nd component of this platform was a 6 degree-of-freedom nanopositioner that was designed, manufactured and tested by me in collaboration with my colleagues [36]. We showed that this platform is capable of parallelizing two microplates that are ~ 60 × 60 $\mu m^2$ in area with an angular resolution < 6 μrad and control their spatial separation with nanometer resolution. Hence, given perfectly smooth, flat and clean microplates, this instrument can successfully parallelize them with gap-sizes less than a micrometer, paving the way for measurements NFRHT between parallel plates with submicrometer gaps.

The microfabricated calorimeters and the nanopositioner provided us with the necessary tools to perform NFRHT experiments. Most importantly, I was able to make the first experimental measurements of NFRHT enhancements from thin dielectric coatings and study effect of film thickness on NFRHT with my colleagues [45]. These studies showed for the first time orders-of-magnitude increase in radiative HTC from nanoscale-thin dielectric coatings that were comparable to those observed from bulk materials. Our colleagues used the framework of fluctuational electrodynamics in conjunction with a scattering matrix approach to verify these measurements and their theoretical results were in agreement with our experimental results.

## 4.2 Future Directions

There is a range of interesting phenomena that can be explored using the platform presented in this thesis. The first future goal for this setup is to make the first experimental measurement of NFRHT

from parallel plates with submicrometer gaps and observe 3 orders-of-magnitude enhancement in heat transfer. Subsequently, the platform can be used for a range of interesting NFRHT studies such as high-precision lithography [51], heat-assisted magnetic recording (HAMR) [47], near-field thermo-photovoltaics (NTPV) [1], thermal diodes (rectification) [14, 48], and nanoporous surfaces [78].

### 4.2.1 Measurement of NFRHT between Parallel Plates with Submicrometer Gaps

While there have been a few experimental efforts in measuring NFRHT between parallel plates with submicrometer gaps [21, 23], they have been limited by the design of the devices. As mentioned in chapter 1, in [21], NFRHT is measured between parallel beams but do to the fact that the thickness of the beams is less than propagation length of surface waves, this experiment cannot fully capture the plane-plane geometry as the beams are confined in one direction. A more recent work was also presented [23]; however, this work was limited only to three gap-sizes and there were many experimental limitations: a) the devices were not flat as-fabricated and flatness was achieved by applying pressure on the devices; the pressure was prescribed based on a simplified FEM model, b) a white-light interferometry approach was used to measure the gap uniformity but it assumed there was no particulate contamination, c) there were large uncertainties both in gap-size and HTC and fitting parameters were used to reach agreement between experimental and theoretical results.

The platform we designed removes the experimental limitations of previous works. In particular, it enables parallelization and spatial-separation control between any two planar surfaces. Consequently, it is possible to make measurements of NFRHT enhancement between a range of devices. In fact, our initial experiments have been able to go to gap-sizes as low as ~100 nm and

measure ~150 times increase in HTC. We are currently in process of making further measurements to achieve a gap-size < 100 nm and 3 orders-of-magnitude increase in radiative heat transfer.

### 4.2.2 Near-Field Thermo-Photovoltaic Devices

One of the most interesting applications of NFRHT will be in design of novel near-field thermo-photovoltaic (NTPV) devices. For example, a NTPV device proposed by Park et al. [1], can increase the power output of the TPV device and reach conversion efficiencies as high as 24.5%. However, to date, no NTPV device has been demonstrated experimentally. The platform presented in this thesis can be used in conjunction with microfabricated devices for the first experimental demonstration of a NTPV device. This will require addressing additional experimental considerations since such a TPV device will need to work at much higher temperature differences. Once these experimental difficulties are addresses, the platform can be used to design and test the first NTPV device, greatly increasing the power output comparing to existing TPV devices.

# References


1. Park, K., et al., *Performance analysis of near-field thermophotovoltaic devices considering absorption distribution.* Journal of Quantitative Spectroscopy & Radiative Transfer, 2008. **109**(2): p. 305-316.

2. Guha, B., et al., *Near-Field Radiative Cooling of Nanostructures.* Nano Letters, 2012. **12**(9): p. 4546-4550.

3. Jones, A.C., et al., *The thermal near-field: Coherence, spectroscopy, heat-transfer, and optical forces.* Progress in Surface Science, 2013. **88**(4): p. 349-392.

4. Basu, S., Z.M. Zhang, and C.J. Fu, *Review of near-field thermal radiation and its application to energy conversion.* International Journal of Energy Research, 2009. **33**(13): p. 1203-1232.

5. Polder, D. and M.A.V. Hove, *Theory of Radiative Heat Transfer between Closely Spaced Bodies.* Physical Review B, 1971. **4**(10): p. 3303-3314.

6. Incropera, F.P., *Introduction to heat transfer*. 5th ed. 2007, Hobokenm NJ: Wiley. xxv, 901 p.

7. Basu, S., Z. Zhang, and C. Fu, *Review of Near-field thermal radiation and its application to energy conversion.* International Journal of Energy Research, 2009. **33**(13): p. 1203-1232.

8. Joulain, K., et al., *Surface electromagnetic waves thermally excited: Radiative heat transfer, coherence properties and Casimir forces revisited in the near field.* Surface Science Reports, 2005. **57**(3-4): p. 59-112.

9. Rytov, S.M., I.A. Kravtsov, and V.I. Tatarskii, *Principles of statistical radiophysics*. 2. rev. and enl. ed. 1987, Berlin ; New York: Springer-Verlag.

10. Song, B., Fiorino, A., Meyhofer, E., Reddy, P., *Near-field radiative thermal transport: From theory to experiment.* AIP Advances, 2015. **5**.

11. Biehs, S.A., *Thermal heat radiation, near-field energy density and near-field radiative heat transfer of coated materials.* European Physical Journal B, 2007. **58**(4): p. 423-431.

12. Joulain, K., et al., *Surface electromagnetic waves thermally excited: Radiative heat transfer, coherence properties and Casimir forces revisited in the near field.* Surface Science Reports, 2005. **57**(3-4): p. 59-112.

13. Basu, S., B.J. Lee, and Z.M. Zhang, *Near-Field Radiation Calculated With an Improved Dielectric Function Model for Doped Silicon.* Journal of Heat Transfer-Transactions of the Asme, 2010. **132**(2).

14. Basu, S. and M. Francoeur, *Near-field radiative transfer based thermal rectification using doped silicon.* Applied Physics Letters, 2011. **98**(11).

15. Domoto, G.A., R.F. Boehm, and C.L. Tien, *Experimental Investigation of Radiative Transfer between Metallic Surfaces at Cryogenic Temperatures.* Journal of Heat Transfer, 1970. **92**(3): p. 412-&.

16. Hargreav.Cm, *Anomalous Radiative Transfer between Closely-Spaced Bodies.* Physics Letters A, 1969. **A 30**(9): p. 491-&.

17. Hu, L., et al., *Near-field thermal radiation between two closely spaced glass plates exceeding Planck's blackbody radiation law.* Applied Physics Letters, 2008. **92**(13).

18. Ottens, R.S., et al., *Near-Field Radiative Heat Transfer between Macroscopic Planar Surfaces.* Physical Review Letters, 2011. **107**(1).

19. Kralik, T., et al., *Cryogenic apparatus for study of near-field heat transfer.* Review of Scientific Instruments, 2011. **82**(5).

20. Kralik, T., et al., *Strong Near-Field Enhancement of Radiative Heat Transfer between Metallic Surfaces.* Physical Review Letters, 2012. **109**(22).

21. St-Gelais, R., Guha, B., Zhu, L., Fan, S., and Lipson, M., *Demonstration of Strong Near-Field Radiative Heat Transfer between Integrated Nanostructures.* Nano Letters, 2014.

22. Carminati, R. and J.J. Greffet, *Near-field effects in spatial coherence of thermal sources.* Physical Review Letters, 1999. **82**(8): p. 1660-1663.

23. Ito, K., et al., *Parallel-plate submicron gap formed by micromachined low-density pillars for near-field radiative heat transfer.* Applied Physics Letters, 2015. **106**(8).

24. Shen, S., A. Narayanaswamy, and G. Chen, *Surface Phonon Polaritons Mediated Energy Transfer between Nanoscale Gaps.* Nano Letters, 2009. **9**(8): p. 2909-2913.

25. Shen, S., et al., *Nanoscale thermal radiation between two gold surfaces.* Applied Physics Letters, 2012. **100**(23).

26. Rousseau, E., et al., *Radiative heat transfer at the nanoscale.* Nature Photonics, 2009. **3**(9): p. 514-517.

27. Lai, J., et al., *Optimization and performance of high-resolution micro-optomechanical thermal sensors.* Sensors and Actuators a-Physical, 1997. **58**(2): p. 113-119.

28. Shen, S., et al., *Thermal conductance of bimaterial microcantilevers.* Applied Physics Letters, 2008. **92**(6): p. 3.

29. Francoeur, M., M.P. Menguc, and R. Vaillon, *Near-field radiative heat transfer enhancement via surface phonon polaritons coupling in thin films.* Applied Physics Letters, 2008. **93**(4): p. 043109-11.

30. Basu, S. and Z.M. Zhang, *Ultrasmall penetration depth in nanoscale thermal radiation.* Applied Physics Letters, 2009. **95**(13): p. 3.

31. Narayanaswamy, A. and Y. Zheng, *A Green's function formalism of energy and momentum transfer in fluctuational electrodynamics.* Journal of Quantitative Spectroscopy & Radiative Transfer, 2014. **132**: p. 12-21.

32. Ben-Abdallah, P., K. Joulain, and A. Pryamikov, *Surface Bloch waves mediated heat transfer between two photonic crystals.* Applied Physics Letters, 2010. **96**(14).

33. Sadat, S., et al., *Room temperature picowatt-resolution calorimetry.* Applied Physics Letters, 2011. **99**(4): p. 3.

34. Sadat, S., E. Meyhofer, and P. Reddy, *Resistance thermometry-based picowatt-resolution heat-flow calorimeter.* Applied Physics Letters, 2013. **102**(16): p. 163110-3.

35. Sadat, S., E. Meyhofer, and P. Reddy, *High resolution resistive thermometry for micro/nanoscale measurements.* Review of Scientific Instruments, 2012. **83**(8).

36. Ganjeh, Y., et al., *A platform to parallelize planar surfaces and control their spatial separation with nanometer resolution.* Review of Scientific Instruments, 2012. **83**(10): p. 105101-9.

37. Volokitin, A.I. and B.N.J. Persson, *Near-field radiative heat transfer and noncontact friction.* Reviews of Modern Physics, 2007. **79**(4): p. 1291-1329.

38. Otey, C., W.T. Lau, and S. Fan, *Thermal Rectification through Vacuum.* Physical Review Letters, 2010. **104**(15).

39. Hu, L., et al., *Near-field thermal radiation between two closely spaced glass plates exceeding Planck's blackbody radiation law.* Applied Physics Letters, 2008. **92**(13).

40. Otey, C. and S. Fan, *Numerically exact calculation of electromagnetic heat transfer between a dielectric sphere and plate.* Physical Review B, 2011. **84**(24).

41. Biehs, S.-A., et al., *Nanoscale heat flux between nanoporous materials.* Optics Express, 2011. **19**(19): p. A1088-A1103.

42. Zwol, P.J.v., et al., *Fast nanoscale heat-flux modulation with phase-change materials.* Physical Review B, 2011. **83**(20).

43. Madou, M.J., *Fundamentals of microfabrication and nanotechnology*. 3rd ed. Vol. II. 2012, Boca Raton, FL: CRC Press.

44. Hariharan, P., *Optical interferometry*. 2nd ed. 2003, Amsterdam ; Boston: Academic Press. xvi, 351 p.

45. Song, B., Ganjeh, Y., Sadat, S., Thompson, D.R., Fiorino, A.R., Fernández-Hurtado, V., Feist, J., Garcia Vidal, F.J., Cuevas, J.C., Reddy, P., Myhofer, E., *Enhancement of near-field radiative heat transfer using polar dielectric thin films.* Nature Nanotechnology, 2015. **10**(3).

46. Challener, W.A., et al., *Heat-assisted magnetic recording by a near-field transducer with efficient optical energy transfer.* Nature Photonics, 2009. **3**(4): p. 220-224.

47. Stipe, B.C., et al., *Magnetic recording at 1.5 Pb m(-2) using an integrated plasmonic antenna.* Nature Photonics, 2010. **4**(7): p. 484-488.

48. Otey, C., W.T. Lau, and S. Fan, *Thermal Rectification through Vacuum.* Physical Review Letters, 2010. **104**(15): p. 154301-4.

49. Rodriguez, A.W., et al., *Frequency-Selective Near-Field Radiative Heat Transfer between Photonic Crystal Slabs: A Computational Approach for Arbitrary Geometries and Materials.* Physical Review Letters, 2011. **107**(11): p. 114302-5.

50. van Zwol, P.J., L. Ranno, and J. Chevrier, *Tuning Near Field Radiative Heat Flux through Surface Excitations with a Metal Insulator Transition.* Physical Review Letters, 2012. **108**(23): p. 234301-4.

51. Pendry, J.B., *Radiative exchange of heat between nanostructures.* Journal of Physics-Condensed Matter, 1999. **11**(35): p. 6621-6633.

52. Kittel, A., et al., *Near-field heat transfer in a scanning thermal microscope.* Physical Review Letters, 2005. **95**(22).

53. Francoeur, M., M.P. Menguc, and R. Vaillon, *Coexistence of multiple regimes for near-field thermal radiation between two layers supporting surface phonon polaritons in the infrared.* Physical Review B, 2011. **84**(7).

54. Worbes, L., D. Hellmann, and A. Kittel, *Enhanced Near-Field Heat Flow of a Monolayer Dielectric Island.* Physical Review Letters, 2013. **110**(13).

55. Liu, C., *Foundations of MEMS*. 2nd ed. 2012, Upper Saddle River, N.J.: Prentice Hall. xiv, 562 p.

56. Senturia, S.D., *Microsystem design*. 2001, Boston: Kluwer Academic Publishers. xxvi, 689 p.

57. Zhang, X., et al., *Thermal and electrical conductivity of a suspended platinum nanofilm.* Applied Physics Letters, 2005. **86**(17).

58. Cappella, B. and G. Dietler, *Force-distance curves by atomic force microscopy.* Surface Science Reports, 1999. **34**(1-3): p. 1-+.

59. Tabor, D. and Winterto.Rh, *Direct Measurement of Normal and Retarded Van Der Waals Forces.* Proceedings of the Royal Society of London Series a-Mathematical and Physical Sciences, 1969. **312**(1511): p. 435-&.

60. Tabor, D. and Winterto.Rh, *Surface Forces - Direct Measurement of Normal and Retarded Van Der Waals Forces.* Nature, 1968. **219**(5159): p. 1120-&.

61. Narayanaswamy, A., S. Shen, and G. Chen, *Near-field radiative heat transfer between a sphere and a substrate.* Physical Review B, 2008. **78**(11).

62. Cahill, D.G., et al., *Nanoscale thermal transport. II. 2003-2012.* Applied Physics Reviews, 2014. **1**(1).

63. Feingold, A.G., K. G., *New analytical approach to the evaluation of configuration factors in radiation from spheres and infinitely long cylinders.* J. Heat Transfer, 1970. **92**: p. 69-76.

64. Ehlert, J.R. and T.F. Smith, *View Factors for Perpendicular and Parallel Rectangular-Plates.* Journal of Thermophysics and Heat Transfer, 1993. **7**(1): p. 173-175.

65. Palik, E.D., *Handbook of optical constants of solids*. Academic Press handbook series. 1985, Orlando: Academic Press. xviii, 804 p.

66. Ordal, M.A., et al., *Optical-Properties of the Metals Al, Co, Cu, Au, Fe, Pb, Ni, Pd, Pt, Ag, Ti, and W in the Infrared and Far Infrared.* Applied Optics, 1983. **22**(7): p. 1099-1119.

67. Derjaguin, B.V., *Direct Measurement of Molecular Attraction between Solids Separated by a Narrow Gap.* Quarterly Reviews, 1956. **10**(3): p. 295-&.

68. Whittaker, D.M. and I.S. Culshaw, *Scattering-matrix treatment of patterned multilayer photonic structures.* Physical Review B, 1999. **60**(4): p. 2610-2618.

69. Cataldo, G., et al., *Infrared dielectric properties of low-stress silicon nitride.* Optics Letters, 2012. **37**(20): p. 4200-4202.

70. Sasihithlu, K. and A. Narayanaswamy, *Proximity effects in radiative heat transfer.* Physical Review B, 2011. **83**(16).

71. Rodriguez, A.W., M.T.H. Reid, and S.G. Johnson, *Fluctuating-surface-current formulation of radiative heat transfer: Theory and applications.* Physical Review B, 2013. **88**(5).

72. Reid, M.T.H.J., S. G., *Efficient computation of power, force and torque in BEM scattering calculations.* arXiv:1307.2966, 2013.

73. Mulet, J.P., et al., *Enhanced radiative heat transfer at nanometric distances.* Microscale Thermophysical Engineering, 2002. **6**(3): p. 209-222.

74. Biehs, S.A., E. Rousseau, and J.J. Greffet, *Mesoscopic Description of Radiative Heat Transfer at the Nanoscale.* Physical Review Letters, 2010. **105**(23): p. 234301-4.

75. Ben-Abdallah, P. and S.A. Biehs, *Near-Field Thermal Transistor.* Physical Review Letters, 2014. **112**(4): p. 044301-4.

76. Rodriguez, A.W., et al., *Anomalous Near-Field Heat Transfer between a Cylinder and a Perforated Surface.* Physical Review Letters, 2013. **110**(1): p. 014301-4.

77. Lenert, A., et al., *A nanophotonic solar thermophotovoltaic device.* Nature Nanotechnology, 2014. **9**(2): p. 126-130.

78. Biehs, S.A., et al., *Nanoscale heat flux between nanoporous materials.* Optics Express, 2011. **19**(19): p. A1088-A1103.